NOTE TO USERS

UNIVERSITÉ DE MONTRÉAL

COMMANDE NONLINÉAIRE DE MICROMIRROIRS ÉLECTROSTATIQUES

CARLOS GUSTAVO AGUDELO
DÉPARTEMENT DE GÉNIE ÉLECTRIQUE
ÉCOLE POLYTECHNIQUE DE MONTRÉAL

MÉMOIRE PRÉSENTÉ EN VUE DE L'OBTENTION
DU DIPLÔME DE MAÎTRISE ÈS SCIENCES APPLIQUÉES
(GÉNIE ÉLECTRIQUE)
APRIL 2008

Your file Votre référence
ISBN: 978-0-494-46027-6
Our file Notre référence
ISBN: 978-0-494-46027-6

UNIVERSITÉ DE MONTRÉAL

ÉCOLE POLYTECHNIQUE DE MONTRÉAL

Ce mémoire intitulé:

COMMANDE NONLINÉAIRE DE MICROMIRROIRS ÉLECTROSTATIQUES

présenté par: AGUDELO Carlos Gustavo

en vue de l'obtention du diplôme de: Maîtrise ès sciences appliquées

a été dûment accepté par le jury d'examen constitué de:

M. DE SANTIS Romano, Ph.D., président

M. SAYDY Lahcen, Ph.D., membre et directeur de recherche

M. ZHU Guchuan, Ph.D., membre et codirecteur de recherche

Mme. AKHRIF Ouassima, Ph.D., membre

RÉSUMÉ

Le micromiroir à torsion est actuellement l'un des systèmes Micro-Opto-Eletro-Mécaniques (MOEMS) les plus populaires. Grâce à sa polyvalence, sa taille réduite, sa haute vitesse et sa faible consommation de puissance, le micromiroir est de plus en plus utilisé dans diverses applications scientifiques, commerciales ou de défense [Bauer (2003), Ramani (2006), Lyshevski and Lyshevski (2003)], telles que l'optique adaptative [Tyson (2000)], les réseaux optiques [Chu *et al.* (2002), Chu *et al.* (2005)], les systèmes de projection [Kessel (1998)], et les communications inter-satellites [Suhonen *et al.* (2001)].

La force électrostatique est le moyen le plus utilisé pour déplacer le micromiroir [Kovacs (1998), Thielicke and Obermeier (2000)]. Cependant, cet actionnement est hautement nonlinéaire, ceci rendant le contrôle en boucle ouverte très difficile. De plus, la nonlinéarité produit une bifurcation de type selle, appelée Pull-in, qui fait que plus de la moitié de la gamme du micromiroir est instable. Pour cette raison, un contrôle en boucle fermée, qui offre de la stabilité et une bonne performance est proposé.

Dans ce travail, un model nonlinéaire pour le micromiroir électrostatique est obtenu. Des micromiroirs à torsion électrostatiques avec un et deux électrodes sont considérés. Ensuite, deux contrôleurs nonlinéaires basés sur la théorie de platitude et la linéarisation exacte entré-sortie sont conçus pour les deux types de micromiroirs. L'objective du contrôle en boucle fermée est d'obtenir des opérations sur toute la gamme du micromiroir. Suite à cela, un montage expérimental est mis en œuvre pour implémenter les lois de contrôle pour les deux sortes de micromiroirs, et pour tester la performance dynamique et la gamme d'opération. Les différents aspects d'implémentation en temps réel sont discutés. Les résultats démontrent que les contrôleurs développés peuvent atteindre une bonne performance avant et après le Pull-in.

ABSTRACT

The torsional micromirror is currently one of the most popular Micro-Opto-Electro-Mechanical Systems (MOEMS). Due to its versatility, reduced size, high velocity, and low power consumption, the micromirror is rapidly finding its way into a variety of scientific, commercial, and defense applications [Bauer (2003), Ramani (2006), Lyshevski and Lyshevski (2003)]. Fields such as adaptive optics [Tyson (2000)], optical network switching [Chu *et al.* (2002), Chu *et al.* (2005)], projection systems [Kessel (1998)], and inter-satellite laser communications [Suhonen *et al.* (2001)] are readily making use of this device.

The most popular driving scheme for the micromirror is electrostatic actuation [Kovacs (1998), Thielicke and Obermeier (2000)], however, it is highly nonlinear, making open-loop control over a large operating range difficult. Furthermore, the nonlinearity gives rise to a saddle-node bifurcation, called "Pull-In", that makes more than half of the mirror range inherently unstable. For this reason, a stabilizing closed-loop scheme that accounts for such nonlinearities and additionally offers good dynamic performance is proposed.

A novel nonlinear model for the electrostatic micromirror is obtained using the voltage across the device as a state variable, which facilitates the control system implementation. Single- and dual-electrode torsional micromirrors are considered. Then, two nonlinear closed-loop tracking controllers based on exact linearization techniques are designed for each kind of micromirror, having as objective to achieve whole range operation. Next, an experimental test-bed is put together to characterize real micromirrors, to implement the control laws for both single- and dual-electrode micromirrors, and to test dynamic performance and operating range. Real-time issues are also discussed. Results demonstrate that the developed control schemes can achieve good performance below and beyond pull-in.

CONDENSÉ EN FRANÇAIS

Introduction

Le micromiroir à torsion est actuellement l'un des systèmes Micro-Opto-Eletro-Mécaniques (MOEMS) les plus populaires. Grâce à sa polyvalence, sa taille réduite, sa haute vitesse et sa faible consommation de puissance, le micromiroir est de plus en plus utilisé dans diverses applications scientifiques, commerciales ou de défense [Bauer (2003), Ramani (2006), Lyshevski and Lyshevski (2003)], telles que l'optique adaptative [Tyson (2000)], les réseaux optiques [Chu *et al.* (2002), Chu *et al.* (2005)], les systèmes de projection [Kessel (1998)], et les communications inter-satellites [Suhonen *et al.* (2001)].

La force électrostatique est le moyen le plus utilisé pour déplacer le micromiroir [Kovacs (1998), Thielicke and Obermeier (2000)]. Cependant, cet actionnement est hautement nonlinéaire, ceci rendant le contrôle en boucle ouverte très difficile. Afin d'intégrer le miroir électrostatique dans des applications de haute performances la gamme d'opération doit être élargie et le comportement dynamique doit être approprié. Ceci est très difficile à réaliser dû à la dynamique hautement nonlinéaire du micromiroir. De plus, la nonlinéarité produit une bifurcation de type selle, appelée Pull-in, qui fait que plus de la moitié de la gamme du micromiroir est instable.

Le Pull-in se produit lorsque le couple électrostatique entrainé par les électrodes vainc le couple mécanique restaurateur. Au-delà de ce point le micromiroir devient instable et s'écrase subitement contre l'électrode inférieure. Pour cette raison, un contrôle en boucle fermée, qui offre de la stabilité et une bonne performance est proposé dans ce mémoire.

Objectives

- Obtenir un model nonlinéaire pour le micromiroir électrostatique. Des micromiroirs à torsion électrostatiques avec un et deux électrodes sont considérés.
- Concevoir deux contrôleurs nonlinéaires basés sur la théorie de linéarisation exacte pour les deux types de micromiroirs.
- Implémenter les lois de contrôle pour les deux sortes de micromiroirs par moyen d'un montage expérimental afin de tester la performance dynamique et la gamme d'opération.
- Identifier les différents aspects d'implémentation en temps réel.

Modelisation du Micromiroir Électrostatique

Dans la littérature une manière commune de modeliser la dynamique du miroir électrostatique est d'utiliser la charge électrique à travers les électrodes comme variable d'état [Senturia (2002)Zhu *et al.* (2006)b]. Cependant, l'implémentation de capteurs de charge électrique on-chip souvent devient complexe [Anderson *et al.* (2005)] en plus du bruit et basse résolution associés. Une option viable est de choisir le voltage à la place de la charge comme variable d'état pour la conception du system de contrôle. La captation de voltage est direct du point de vue pratique, en plus puisque le voltage d'actuation est normalement de quelque dizaine de volts donc on peut attendre une meilleure résolution et meilleures rapports signal-bruit.

Le schema d'un micromiroir est montré à la Fig. 1. La capacitance dû à chaque électrode peut être exprimé comme

$$C_a = C_0\gamma(\theta),$$

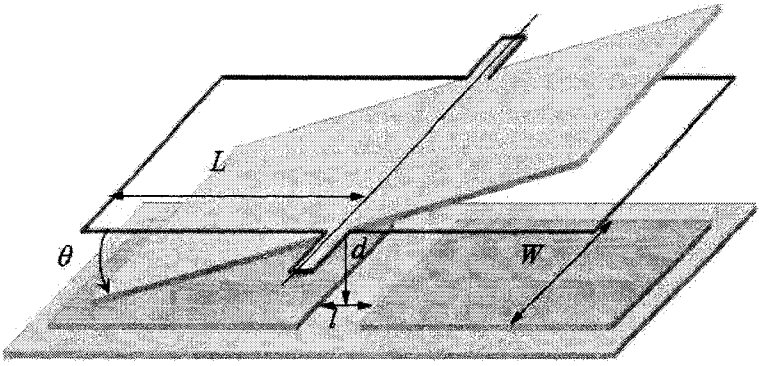

FIGURE 1 SCHEMA D'UN MICROMIROIR.

où C_0 est une constante qui représente la capacitance lorsque il n'y a pas de voltage appliqué et une fonction adimensionnelle $\gamma(\theta)$ est introduite pour représenter la variation de la capacitance lorsque l'angle varie. L'équation de mouvement est donnée par

$$J\ddot{\theta} + b\dot{\theta} + k\theta = T_e,$$

où θ est l'angle, J est le moment d'inertie de l'électrode mobile, b est le coefficient visqueux, k est le coefficient du ressort, et T_e est le couple électrostatique. T_e est donné par [Senturia (2002)]:

$$T_e = \frac{1}{2} V_a^2 C_0 \gamma'_\theta$$

où V_a est le voltage à travers le dispositif.

Afin de générer une force électrique, un voltage élevé doit être fourni au micromiroir. En général un amplificateur de haut voltage est utilisé pour ceci.

La dynamique du circuit électrique peut être déduit à partir du circuit équivalent montré à la Fig. 2. En laissant $\omega = \dot{\theta}$ être la vitesse angulaire, V_s le signal de contrôle, et en faisant $\rho = C_p/C_0$, le micromiroir sous l'influence d'un seul électrode

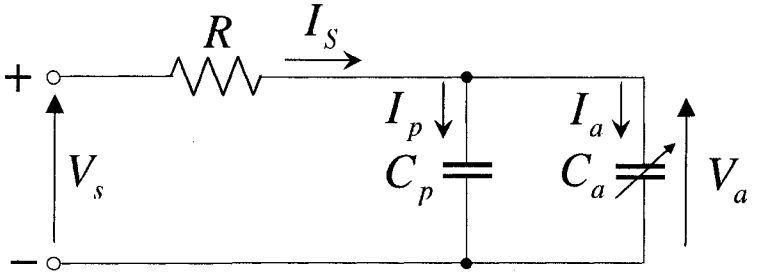

FIGURE 2 CIRCUIT ÉLECTRIQUE ÉQUIVALENT.

peut être décrit en forme d'état comme:

$$\begin{aligned}
\dot{\theta} =& \omega \\
\dot{\omega} =& \frac{1}{J}\left(-b\omega - k\theta + \frac{C_0}{2}\gamma'_\theta V_a^2\right) \\
\dot{V}_a =& \frac{1}{\rho + \gamma_\theta}\left(\frac{V_s - V_a}{RC_0} - \omega\gamma'_\theta V_a\right)
\end{aligned}$$

valide dans l'espace restreint $\mathcal{X} = \{(\theta, \omega, V_a) \subset \mathbb{R}^3 | \theta \in [0, \theta_{\max})\}$.

Par la suite, on se réfère à l'électrode positive (négative respectivement) comme celui-là qui produit une rotation dans le sens horaire (anti-horaire respectivement) lorsque un voltage lui est appliqué. En nommant C_{ep} et C_{en} comme les capacitances dûes aux électrodes positive et négative,

$$\begin{aligned}
C_{ep}(\theta) =& C_0\gamma(\theta), \\
C_{en}(\theta) =& C_{ep}(-\theta) = C_0\gamma(-\theta).
\end{aligned}$$

La dynamique du micromiroir avec deux électrodes et donné donc par

$$\begin{aligned}
\dot{\theta} =& \omega \\
\dot{\omega} =& \frac{1}{J}\left(-b\omega - k\theta + \frac{C_0}{2}\left(\gamma'_\theta V_{ap}^2 + \gamma'_{-\theta} V_{an}^2\right)\right) \\
\dot{V}_{ap} =& \frac{1}{\rho + \gamma_\theta}\left(\frac{V_{sp} - V_{ap}}{RC_0} - \omega\gamma'_\theta V_{ap}\right) \\
\dot{V}_{an} =& \frac{1}{\rho + \gamma_{-\theta}}\left(\frac{V_{sn} - V_{an}}{RC_0} - \omega\gamma'_{-\theta} V_{an}\right)
\end{aligned}$$

où V_{sp} et V_{sn} sont les signaux de contrôle pour l'électrode positive et négative respectivement. Valide dans l'espace restreint $\mathcal{X} = \{(\theta, \omega, V_{ap}, V_{an}) \subset \mathbb{R}^4 | \theta \in (-\theta_{\max}, \theta_{\max})\}$.

Synthèse du Contrôleur

La conception des contrôleurs en boucle fermée est basée sur la technique de linéarisation exacte et planification de trajectoire. En utilisant trajectoires de référence différentes types d'opérations, comme scanning control and set-point, son accordés. En plus, la performance dynamique peut être spécifiée par un choix approprié de la trajectoire de référence, ce qui permet au system de contrôle se dérouler d'une façon systématique.

Avant de développer les contrôleurs la contrôlabilité locale est explorée. Il est assez direct de conclure que le micromirroir électrostatique est contrôlable tout au long de sa gamme sauf au point où V_a est zéro. Ce point-ci est appelé flat position. D'ailleurs, le system est observable localement dans toute la gamme du micromirroir.

Après quelque calcules il est montré que la loi de contrôle de linéarisation exact est

donné par

$$V_s = \frac{R}{\gamma'_\theta V_a}(\rho + \gamma_\theta)\left(Jv + b\ddot{\theta} + k\dot{\theta}\right) + V_a\left(1 + RC_0\gamma'_\theta\dot{\theta} - \frac{RC_0\gamma''_\theta\dot{\theta}(\rho + \gamma_\theta)}{2\gamma'_\theta}\right).$$

Il est direct à voir que la loi de contrôle est singulier lorsque $V_a = 0$. Afin de réaliser le contrôle de poursuite nous définissons $e = y - y_r$ comme l'erreur de poursuite et $y_r(t)$ la trajectoire désirée. Alors, il suffit de choisir v comme

$$v = \dddot{y}_r - k_2\left(\ddot{\theta} - \ddot{y}_r\right) - k_1\left(\dot{\theta} - \dot{y}_r\right) - k_0\left(\theta - y_r\right),$$

pour obtenir une poursuite stable asymptotiquement à condition que $s^3+k_2s^2+k_1s+k_0$ soit un polynôme Hurwitz.

Dans le but d'échapper à la noncontrôlabilité à la flat position, une actuation différentielle est proposée pour le micromiroir avec deux électrodes. Un schéma de la configuration différentielle est montré à la Fig. 5.5. Selon la Fig. 5.5, les voltages

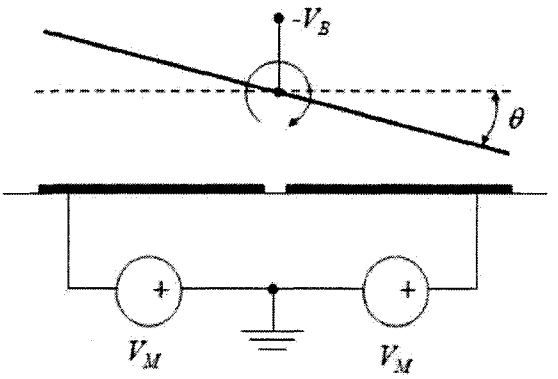

FIGURE 3 SCHEMA DE LA CONFIGURATION DIFFÉRENTIELLE.

d'entrée deviennent donc

$$V_{sp} = V_B + V_M,$$
$$V_{sn} = V_B - V_M.$$

Donc, la loi de contrôle devient

$$V_M = \left[R\left(Jv + b\ddot{\theta} + k\dot{\theta}\right) - V_B\left(\frac{\gamma'_\theta}{C_1}V_{ap} + \frac{\gamma'_{-\theta}}{C_2}V_{an}\right) + \left(\frac{\gamma'_\theta}{C_1}V_{ap}^2 + \frac{\gamma'_{-\theta}}{C_2}V_{an}^2\right) + R\dot{\theta}C_0\left(\frac{{\gamma'_\theta}^2}{C_1}V_{ap}^2 + \frac{{\gamma'_{-\theta}}^2}{C_2}V_{an}^2\right) - \frac{R\dot{\theta}C_0}{2}\left(\gamma''_\theta V_{ap}^2 + \gamma''_{-\theta}V_{an}^2\right)\right]\left(\frac{\gamma'_\theta}{C_1}V_{ap} - \frac{\gamma'_{-\theta}}{C_2}V_{an}\right)^{-1}.$$

Montage Expérimental

A schéma du montage est montré à la Fig. 6.1, qui comprend une unité de contrôle xPCtarget-based, une carte DAQ National Instruments de 12bits (6025E), un amplificateur de haut voltage (Apex PA97), deux boosters de voltage (EMCO G05) qui fournit l'alimentation de voltage à l'amplificateur, une source laser infrarouge (longueur d'onde 900nm), et un capteur de position Hamamatsu (PSD S1880).

Les interfaces électroniques entre les capteurs, les actuateurs, et la carte DAQ ont été développés dans le cadre de ce mémoire. L'image de l'application embarquée en temps réel est développée en Matlab/Simulink dans le host PC, ensuite elle est téléchargée au noyau xPC-Target installé dans le target PC. Pendant l'expérimentation, le host peut commander l'exécution du système de contrôle et récupérer les données. Le laser est utilisé pour mesurer l'angle du micromiroir de manière indirecte.

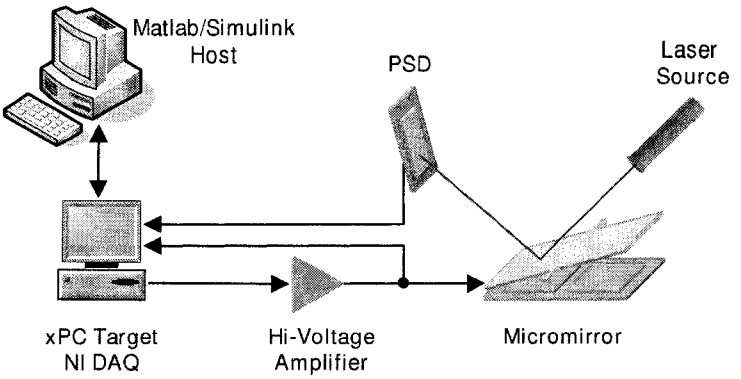

FIGURE 4 SCHÉMA DU MONTAGE EXPÉRIMENTAL.

Soucis Expérimentaux

À travers la réalisation de ce travail quelques obstacles ont été identifiés.

L'exécution en boucle fermée requiert beaucoup d'effort puisque les micromiroirs sont relativement rapides pour la technologie disponible. Le meilleur temps d'échantillonnage atteint a été de $25\mu s$, ce qui est juste à la fréquence de Nyquist.

Les tests au-delà de pull-in ont été extrêmement difficiles parce que les micromiroirs sont pas conçus d'un point de vue de contrôle. Il n'y a même pas de protection physique contre l'écrasement du micromiroir.

Au moment de l'expérimentation en temps réel plusieurs problèmes numériques ont été subis en plus de l'exigence de la bonne performance du matériel.

Il est remarqué qu'une bonne modélisation est nécessaire afin de réaliser un bon contrôle puisque le contrôleur est basé sur celle-ci. Si le model n'est pas assez proche du vrai comportement la performance est sévèrement détérioré.

Résultats Expérimentaux en Boucle-fermée

La Fig 6.18 montre les résultats expérimentaux pour le micromiroir simple (un électrode) pour différents set-points avec transitions de $10ms$ avant pull-in. Il peut être observé que le contrôleur fait le micromiroir poursuivre la trajectoire de référence de près, livrant la réponse dynamique désirée.

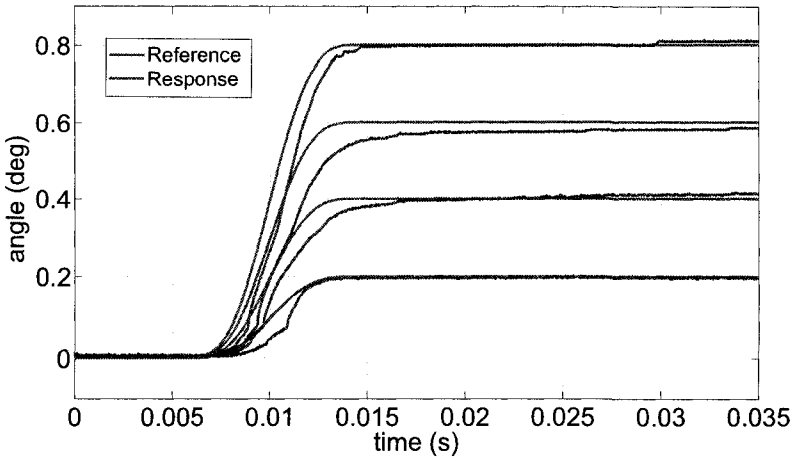

(a)

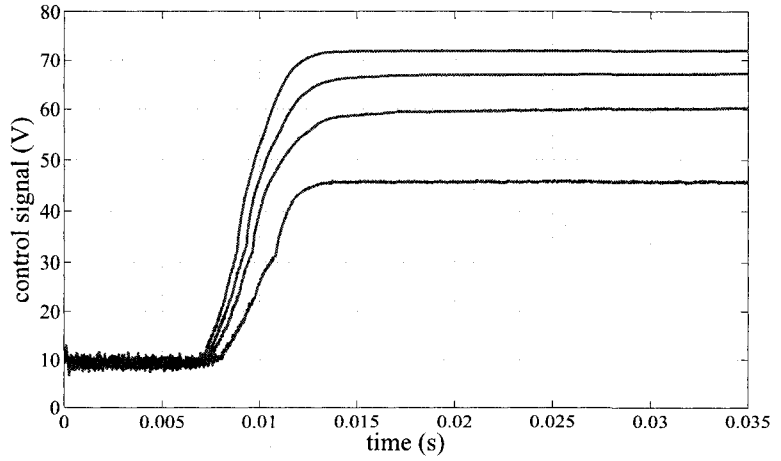

(b)

FIGURE 5 CONTRÔLE EN BOUCLE FERMÉE AVANT PULL-IN: (A) RÉPONSE DU SYSTÈME, (B) SIGNAUX DE CONTRÔLE.

La Fig 6.21 montre une référence de 1.45° pour le micromiroir simple. Il est démontré donc que l'opération au-delà de pull-in est atteint avec succès.

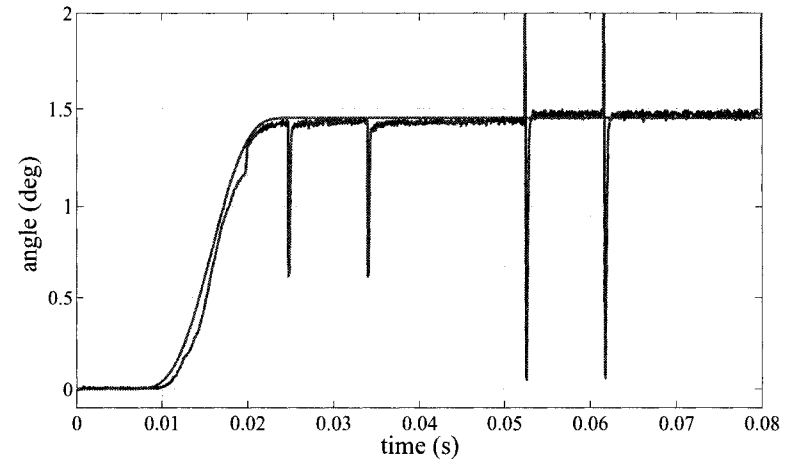

(a)

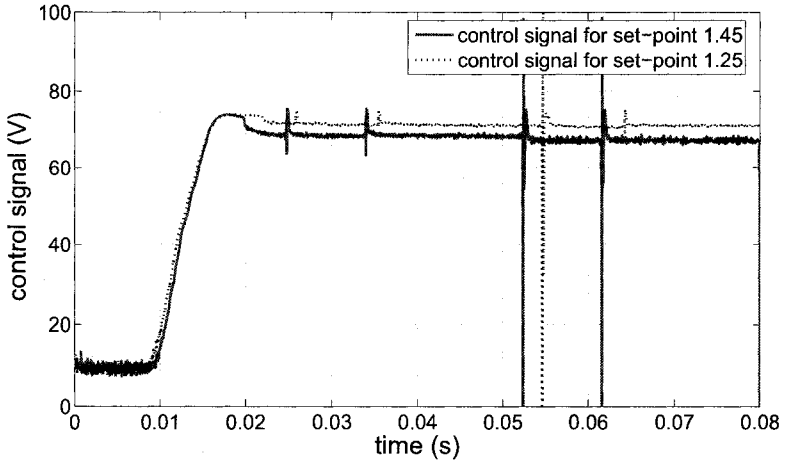

(b)

FIGURE 6 CONTRÔLE EN BOUCLE FERMÉE AU-DELÀ DE PULL-IN: (A) RÉPONSE DU SYSTÈME, (B) SIGNAUX DE CONTRÔLE.

La Fig 6.25(a) montre le résultat expérimental pour le micromiroir double pour une trajectoire scanning d'amplitude 0.5° et une période de 50ms. Un voltage constant V_B de $200V$ a été utilisé. Il peut être vérifié que le micromiroir suit la référence sans distorsion. La Fig 6.25(b) montre le signal de contrôle V_M.

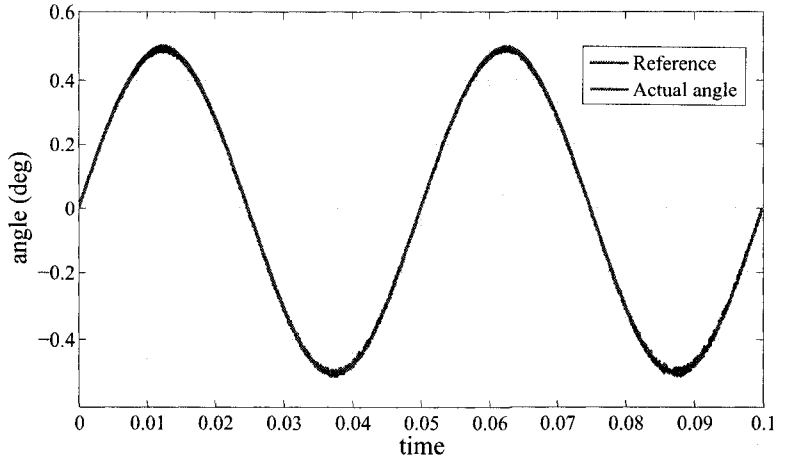

(a)

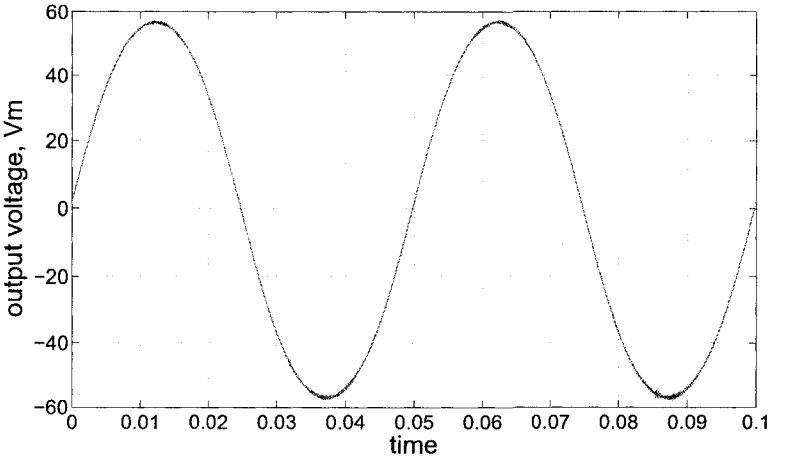

(b)

FIGURE 7 CONTRÔLE EN BOUCLE FERMÉE: (A) RÉPONSE DU SYSTÈME, (B) SIGNAUX DE CONTRÔLE V_M.

La figure précédente montre que la configuration différentielle enlève efficacement la noncontrolabilité de la position flat, tout en permettant le micromiroir de se balancer à travers ce point-ci sans problème.

Conclusions

Un model fiable du micromiroir électrostatique a été développé.

Des lois de contrôle performantes et stabilisantes basées sur la théorie nonlinéaire ont été conçues avec succès.

La noncontrolabilité à la position flat a été enlevé efficacement.

Des nombreux aspects pratiques qui influencent la performance du système de contrôle en temps réel ont été identifiés.

Un montage expérimental a été mis en œuvre pour implémenter le contrôle en boucle fermée du micromiroir électrostatique.

CONTENTS

LIST OF TABLES

LIST OF FIGURES

LIST OF ABBREVIATIONS AND SYMBOLS

AO Adaptive Optics

BIOMEMS Biological MEMS

DAQ Data Acquisition

DLP Digital Light Processing

DM Deformable Mirror

EKF Extended Kalman Filter

HV High Voltage

MEMS Micro-Electro-Mechanical Systems

MOEMS Micro-Opto-Electro-Mechanical Systems

PSD Position Sensitive Detector

SEM Scanning Electron Microscope

SISO Single-Input Single-Output

TET Task Execution Time

b viscous damping coefficient of the moving electrode

C_a capacitance due to a single electrode

C_0 constant representing the capacitance at the flat position

C_p the parasitic capacitance

d thickness of the air gap

ζ damping ratio of the micromirror

$\gamma(\theta)$ dimensionless function of the tilt angle that represents the variation of the capacitance

J mass moment of inertia of the moving electrode

k stiffness coefficient of the micromirror's hinges

L length of the electrode

R Amplifier output resistance

θ the micromirror's tilt angle

T_e the electrostatic torque exerted on the micromirror

T_M the mechanical torque exerted on the micromirror

$\theta_{\max}$ maximum angle allowed by the geometry of the mirror

θ_{PIN} Pull-in angle

θ_{TOUCH} angle at which there is a physical obstruction that prevents the mirror from attaining the maximum angle

V_a voltage across the micromirror

V_{PIN} Pull-in Voltage

V_s input control voltage

ω angular velocity of the micromirror

ω_n undamped natural frequency of the micromirror

W width of the electrode

CHAPTER 1

INTRODUCTION

1.1 Motivation

The micromirror is one of the most popular Micro-Optical-Electro-Mechanical System (MOEMS). Due to its versatility, reduced size, high velocity, and low power consumption, the micromirror is rapidly finding its way into a variety of scientific, commercial, and defense applications [Bauer (2003), Ramani (2006), Lyshevski and Lyshevski (2003)], such as adaptive optics [Tyson (2000)], optical network switching [Chu *et al.* (2002), Chu *et al.* (2005)], projection systems [Kessel (1998)], and inter satellite laser communications [Suhonen *et al.* (2001)]. For illustration purposes the schematic of a dual electrostatic torsional micromirror is shown in Fig. 1.1.

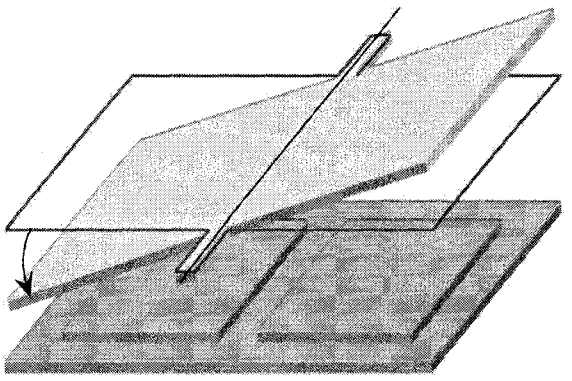

FIGURE 1.1 SCHEMATIC REPRESENTATION OF 1D MICROMIRROR.

Electrostatic actuation is popular because it is simple in structure, flexible in operation, and may be fabricated from standard, well-understood, materials [Kovacs

(1998), Thielicke and Obermeier (2000)]. However, electrostatic actuation is highly nonlinear, making open-loop control over a large operating range difficult.

In order to integrate the electrostatic torsional micromirror into high performance applications, range operation and transient behaviour have to be highly adequate. This is very difficult to achieve due to the highly nonlinear dynamics involved. Furthermore, the nonlinearity gives rise to a saddle-node bifurcation, called "Pull-In", that makes more than half of the angle range inherently unstable. Pull-in occurs when the electrostatic torque produced by the bottom electrodes overcomes the mechanical restoring torque. Beyond this point the movable electrode will abruptly crash down to the fixed electrode. This phenomenon is not new and has been amply studied by several authors [Degani *et al.* (1998), Toshiyoshi *et al.* (2001), Xiao *et al.* (2003)]. Since the micromirror is normally intended to have a controlled motion through all its geometry, the pull-in phenomenon is a limitation because a large portion of the available angle range would be lost. A stabilizing closed-loop scheme that accounts for the nonlinearities becomes then necessary.

In this work, single and dual electrostatic torsional micromirror are addressed. The model is revised taking into account implementation issues. Then, two nonlinear closed-loop tracking controllers based on flatness theory and input-output linearization are designed for single and dual electrostatic micromirrors respectively. The main objective is to achieve whole range operation. Next, an experimental setup is put together and the control law is implemented for both single and dual micromirror to test practical dynamic performance and operating range.

1.2 Previous Work in MEMS Control

Due to the high nonlinearity of the electrostatic micromirror, the control of its motion becomes a difficult task. The pull-in phenomenon, for instance, introduces a complex

behaviour that splits the operational range of the micromirror into an initial stable range and a later unstable range. Bi-stable devices have already been designed to exploit such bifurcation [Bloom (1997), Kessel (1998)]. However, overcoming the pull-in would allow for enhanced functionality in applications requiring fine position capability. Besides, the pull-in causes a shortening in the device lifetime due to the incremental surface damage done after each contact [McCarthy *et al.* (2002)]. Eliminating pull-in via feedback control increases the operational range of the movable electrode, reduces the need for anti-stiction measures, and prevents disturbances from causing the movable electrode to depart from its stable operating region [Maithripala *et al.* (2005)b].

In general, linear control techniques are not enough to deal with such a system since global stability is difficult to guarantee, thus making nonlinear techniques completely justifiable. Nevertheless, Lu and Fedder have reported a classical linear, time-invariant controller design that approximately doubles the stable range of a parallel plate capacitor [Lu and Fedder (2004)]. Transient behaviour is addressed through an input-shaping pre-filter. Guaranteed stability properties are only local.

Seeger [Seeger and Crary (1997)] and Chan [Chan and Dutton (2000)] have removed the pull-in instability by the simple addition of a series capacitance. This scheme guarantees global stability but does not address transient behavior. Besides, it requires a considerable higher voltage than the pull-in voltage to achieve full operational range. A variation using charge control by means of current driving, proposed by Nadal [Nadal-Guardia *et al.* (2002)], shows that full operational range can be achieved without voltage penalty. More recently, Seeger [Seeger and Boser (2003)] implemented a charge control scheme for a parallel-plate actuator that travels up to 83% of the gap, but its transient performance is still poor.

The works found in the literature confirm that nonlinear control techniques can provide a better performance to MOEMS. Maithripala has proposed nonlinear con-

trol strategies applying a port-controlled Hamiltonian structure [Maithripala *et al.* (2003)], using static and dynamic feedback [Maithripala *et al.* (2005)a], and a passivity-based design [Maithripala *et al.* (2005)b]. These approaches offer global stability but a good transient performance is not always guaranteed. Other nonlinear control strategies reported are robust backstepping [Zhu *et al.* (2007)], and controlled Lyapunov function (CLF) synthesis [Zhu *et al.* (2005)a], which offer enhanced transient performance. Nonetheless, the performance of these control algorithms is rarely assessed by experimental validation. Robust control appears to be an interesting approach for devices with a complex structure since the use of models for control purposes utilizes considerably simplified assumptions. Indeed, most works to date neglect physical behaviors such as interelectrode coupling, stiction, electrical shorting, fringing field, squeezing film effect, parameter variations, parasitic elements, and sensing noise.

Some other nonlinear techniques have been reported, such as integral sliding mode control [Zhao *et al.* (2006), Harshad *et al.* (2003)], attaining as high as double the stable range. This technique offers theoretical global stabilization and good robustness, but the transient response is not directly considered. Although its implementation is computationally demanding, this method is readily feasible. Another technique reported is the use of a torque inversion approach [Chu *et al.* (2005), Chen *et al.* (2004)]. These works do not address stability nor transient response directly, but have successfully implemented the control algorithm attaining as high as almost twice the stable region, which corresponds approximately to two-thirds of the total operational range of the device.

A recent approach involving flatness-based control was proposed by Zhu and coauthors [Zhu *et al.* (2006)b, Zhu *et al.* (2006)a, Zhu *et al.* (2005)b]. This strategy offers global stability, transient performance, and implementation feasibility. This thesis is based on those works. Nonetheless, the control and implementation of the

electrostatic micromirror remains a continuing research topic.

Practical results, in the end, justify the supporting theory and the viability of future applications. Experimentation not only provides a deep implementation insight, but also stimulates the subsequent research required to achieve a reliable control system. This is particularly crucial for nonlinear control, which is just making its way into industrial and commercial applications. Even so, implementation matters of nonlinear controllers for the electrostatic micromirror are rarely addressed in the literature.

The aim of this study is to be a thrust in the knowledge of a cutting-edge technology by addressing the nonlinear control of electrostatic micromirrors from theory and practice stand-point and to mark the path for subsequent work.

1.3 Thesis Overview

This thesis searches to assert stabilization and operation of the electrostatic micromirror beyond pull-in by a well designed control system despite the stringent implementation requirements imposed by such a fast and highly nonlinear device.

1.3.1 Objectives

The main objectives of this thesis are:

- Propose a reliable nonlinear model of the electrostatic micromirror for control purposes.
- Develop performing and stabilizing nonlinear control laws for single and dual electrostatic micromirrors.

- Implement the nonlinear control laws for the single and dual electrostatic micromirrors with an experimental setup.
- Identify main issues related to the implementation of real-time control systems.

1.3.2 Contributions

Readily, several concrete contributions of this work can be put forth:

Nonlinear model enhancement

Electrostatic micromirrors are typically modeled in terms of the tilt angle, the angular velocity, and the electrical charge on the device. Although from a theoretical point of view this is a convenient choice, it is not practical due to the ensuing low resolution and the complexity of implementation related to the necessity of the charge measurement. This thesis demonstrates that the voltage across the device is a more convenient state variable for the control of electrostatic micromirrors. The capacitance-based model developed in this work makes the control synthesis clear and well-defined, especially in terms of dynamics performance. Furthermore, using the voltage as a state variable spares a sensor in the MEMS design, impacting positively the manufacturing complexity and reliability, and facilitating the implementation.

Identification of implementation parameters

This thesis deals with the experimental issues involved in the implementation of the nonlinear control of electrostatic micromirrors with low cost components. It characterizes real micromirrors and studies in depth the impact of control considerations to MEMS design.

Proposal of a differential scheme

It is shown that the electrostatic micromirror is uncontrollable at the flat position. To circumvent this situation a differential actuation is proposed. Differential actuation for electrostatic torsional mirror control has the advantage of torque amplification and linearization of the actuation voltage curve. However, this is achieved at the expense of a reduced stability range [Pareek *et al.* (2005)]. This work presents a differential nonlinear closed-loop control in order to obtain stable operations and linearized input-output responses in the whole range of deflection, circumventing the noncontrollability at the origin and hence allowing the micro-mirror to swing through the flat position with continuous bounded control. Furthermore, a reduction of the active control effort is achieved using this control, improving the overall performance.

1.3.3 Document's Organization

The rest of this thesis is organized as follows. Chapter 2 introduces MEMS and their general characteristics. Then, it focuses on the MEMS of interest, namely the micromirror. Chapter 3 describes the dynamic modeling of torsional electrostatic micromirrors and their properties. Two sorts are categorized, torsional electrical micromirror with single and dual bottom electrodes. Chapter 4 covers the general background for the nonlinear control techniques used in the control synthesis of the considered devices. Chapter 5 presents the controller design for both types of micromirrors together with the corresponding simulations. Chapter 6 describes the experimental setup that has been put together with the purpose to implement the proposed controllers. Implementation issues such as noise and calibration are treated and experimental closed-loop control results are presented. Chapter 7 states final conclusions and outlines future work.

CHAPTER 2

MEMS AND THEIR APPLICATIONS

2.1 MEMS Generalities

Micro-Electro-Mechanical Systems (MEMS) is a novel technology that deals with systems whose size is in the order of micrometers. They are usually composed by mechanical and electrical subsystems such as sensors, actuators, electronics, central processing units, among others. Since they all share a common substrate, the level of integration these devices offer is unique, permitting the realization of whole systems on a chip.

The advent of MEMS was possible thanks to semiconductor fabrication technologies, which are the main manufacturing process used for their construction. By sharing the same batch fabrication techniques, electronics and micromachining can be combined to obtain higher levels of miniaturization, integration, reliability, and performance at a relatively low cost. Fig. 2.1 shows a mite on a micromirror assembly at Sandia National Laboratories[1] for illustration purposes.

For the last two decades, intense research has been done in the MEMS area. This active interest has already led to some commercial products that readily make use of the advantages offered by MEMS technologies. Modern vehicles, network equipment, adaptive optics (AO), and entertainment electronics are just some of the fields that are benefiting from MEMS technology. However, despite the vast possibilities that MEMS technology introduces, the transition between laboratory prototypes and commercial products has been slow. There are still several aspects about MEMS that are not well

[1]Courtesy of Sandia National Laboratories, SUMMiTTM Technologies, www.mems.sandia.gov

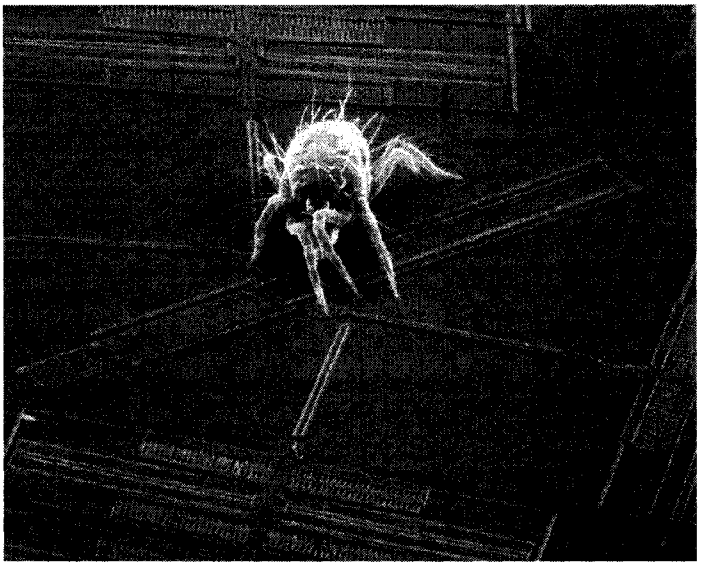

FIGURE 2.1 MITE ON MIRROR ASSEMBLY.

understood and have to be addressed. For instance, classical physics is not always valid at microscopic levels and some phenomenons are still being investigated.

Another important challenge for MEMS is attaining manufacturing reliability. Problems such as stiction (tendency of small devices to stick to each other) and packaging have to be consistently coped with in order to achieve a broader commercial success. There has already been efforts in overcoming stiction issues [Mastrangelo (1999)], but the stiction problem has to be addressed at both engineering and physics level. With proper design and process, it is possible to move beyond prototyping and to achieve the levels of manufacturability required for real applications[2]. This is particularly true for MEMS that require control considerations, which is the case of this work, since MEMS devices might have to include different accessories in order to assure a consistent performance regardless of the operation point. This will be further discussed in chapter 6.

[2]For more detailed information the reader is referred to www.memsnet.org

The packaging issue is also being addressed [Darveaux and Munukutla (2005)] although it continues to be an active research area. Even if the MEMS device works properly, the interface between the device and the environment is crucial for real applications. This is not an easy task as most of the useful applications require a direct contact with the surroundings, increasing the probability of malfunction. One kind of MEMS device that is well suited for packaging are Micro-Opto-Electro-Mechanical Systems (MOEMS). Because of its nature, they can be packaged in a typical way with a glass lid hermetically attached, providing a reliable interface between the optical component and the environment.

2.1.1 MEMS Technologies

The fabrication of a MEMS device is carried out by a repeatable photolithography process, which consists of the transfer of a two-dimensional pattern from a mask into the structural material. The mask is created from CAD tools, and the structure is built up by a series of steps that involve the addition of thin films of material to the structure (Deposition) and the removal of patterned layers of material from the structure (etching) [Banks (2006), Gadelhak (2006)b]. Devices are then built by combining these operations. Typically, two main processes can be outlined:

Bulk Micromachining

Bulk micromachining is a fabrication process that starts with a silicon wafer, then material is selectively removed from the silicon bulk, leaving functional mechanical parts. Typically, the wafer is photo patterned, protecting the material that is to be kept. Next, the wafer is etched away. This process is well suited for simple structures at a relatively low cost. For instance, almost all current pressure sensors are built with Bulk Micromachining.

Surface Micromachining

The Surface Micromachining process builds MEMS devices by the successive deposition and patterning of sacrificial (typically silicon dioxide) and structural (typically silicon) layers on the surface of the silicon wafer. The sacrificial layers are used to create moving parts once they are etched away. Surface Micromachining is more elaborate than Bulk Micromachining, hence more expensive, but it is able to create more complex devices with extended functionality.

2.1.2 Fields of Application

Numerous disciplines are already benefiting from MEMS thanks to the versatility, richness, and novel perspectives these devices propose. MEMS offer a great variety of sensors and actuators with the option of including specialized microstructures to interact with the environment. Besides, the full potential of microelectronics can be incorporated in order to obtain full systems on a chip. Novel applications will certainly emerge since the design possibilities are endless, nonetheless some applications of current interest are [Gadelhak (2006)a, Gaura (2006)]:

2.1.2.1 Biotechnology

MEMS is enabling the rapid evolution of biological-micro-electro-mechanical systems (BIOMEMS). In addition to basic components, such as microchannels, microvalves, micropumps, micromixers and microreactors for flow management at microscopic volumes, several lab-on-a-chip systems have been reported, such as cell and molecule analyzers, pharmaceutical screeners, rapid detectors of environmental mycobacteria, biochips for detection of hazardous chemical and biological agents, among others [Wang and Soper (2007)].

2.1.2.2 Automotive

The automotive industry was the first high volume commercial application of MEMS. The small size, high reliability, and low cost associated with MEMS allowed the smooth insertion of these devices into the automobile in the form of tyre pressure sensors, collision accelerometers, airbag accelerometers, among others. Accelerometers and pressure sensors continue to be today the most used MEMS sensors in the market.

2.1.2.3 Communications

RF-MEMS technology is another branch rapidly emerging. High frequency components such as inductors, tunable capacitors, RF switches, and resonators can be significantly enhanced by designing unique physical structures that outperform their integrated counterparts. Furthermore, the total circuit area, power consumption and cost is considerably reduced.

2.1.2.4 Optics

MOEMS is a rising branch that deals with the direct manipulation of optical signals. This kind of MEMS has the benefit of having simple packaging and high efficiency. One of the most promising MOEMS devices is the micromirror. A detailed description of this device and its fields of application is given in the next section.

Potentially, many other fields such as space, medicine, chemical engineering, electronics or even video games can certainly profit from the advances in MEMS technology.

2.2 The Micromirror: State-of-the-Art and Applications

A micromirror is a MOEMS device whose geometrical extent is in the order of micrometers. Its function is, simply, to reflect light in a way suited for a specific application. The following is a description of the main properties of micromirrors [Motamedi (2005), Leondes (2006)].

2.2.1 Properties

2.2.1.1 Materials

The reflective material used to coat the mirror may differ depending on the light wavelength that is to be reflected. For the visible spectrum, Aluminum (Al) is the most employed material due to its reflective properties and relatively low cost. However, for the infrared range gold (Au) is preferred, although at a greater cost. The supporting structures are generally made out of SiO_2, SOI (Silicon on Insulator), BSOI (Bonded Silicon on Insulator) and Polysilicon Si(100) wafers.

2.2.1.2 Piston vs Torsional Motion

Torsional micromirrors have an angular motion. They rotate around an axis whereas piston motion is done in a longitudinal way. Even though the actuation mechanism might be of the same nature, the final results in reflection are quite different and depend mainly on the type of application. Typically, torsional micromirrors can be made single-axed or dual-axed. Clearly, adding a second degree of movement to the mirror increases its versatility at the cost of rendering the system more complex, since the actuation mechanism has to be properly augmented. Fig. 2.2 shows a dual axis torsional micromirror used in the design of an optical switch by Chu and co-authors

[Chu *et al.* (2005)].

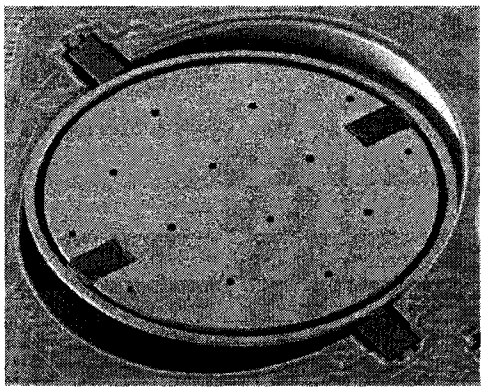

FIGURE 2.2 TWO-AXIS TORSIONAL MICROMIRROR.

2.2.1.3 Range of Operation

Intrinsic to the micromirror motion is the range of displacement it can achieve. Such displacement can be either angular or piston-like. For piston-like mirrors the range of operation is described by the stroke, which refers to the longitudinal distance that the micromirror can attain at its maximum physical displacement. For torsional devices the range of operation is given by the maximum angle permitted by the geometry of the mirror.

2.2.1.4 Actuation Mechanism

There are currently three main mechanisms to actuate micromirrors: electrostatic, mechanical, and electro-thermal. Electrostatic actuation is done by means of electrical electrodes placed underneath the micromirror which exert an electrical force on the movable surface. This type of actuation will be treated in detail in chapter 3. Fig. 2.2 shows a dual-axis electrostatically actuated torsional micromirror with four electrodes

underneath. Mechanical actuation is based on mechanical gears, generally connected to a micro-motor, that make the micromirror shift its position. Fig. 2.3(a) shows such a micromirror built at Sandia National Laboratories[3].

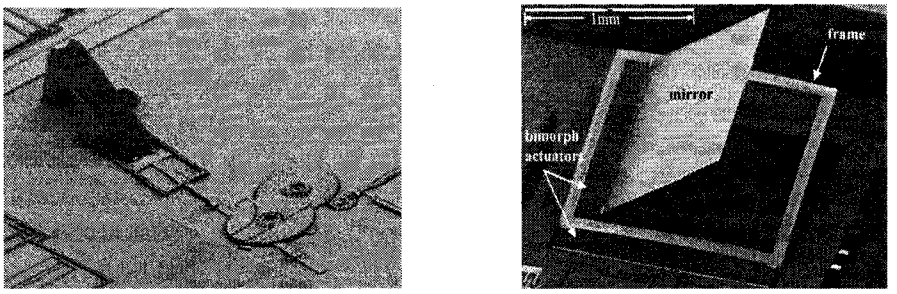

(a) (b)

FIGURE 2.3 ACTUATION MECHANISM: (A) MECHANICAL MIRROR, (B) ELECTRO-THERMAL MIRROR.

Electro-thermal actuation is based on a set of bimorph aluminum/silicon dioxide thin-film beams. When a current is applied through the bimorph actuator, the temperature increases. This makes the beams bend since the thermal coefficient of expansion of aluminum is greater than that of silicon dioxide, resulting in an angular displacement of the attached mirror. Fig. 2.3(b) shows a two-axis electro-thermal micromirror used for an endoscopic tomography [Jain *et al.* (2004)].

2.2.1.5 Surface Shape

Current MEMS technology has two major surface shapes for micromirrors: flat and deformable. Flat mirrors are characterized by having a leveled surface. Any curvature or bump is minimized as much as possible. Applying coatings that simultaneously achieve high reflectivity and optical flatness is a key issue. Flat micromirrors are usually designed as squares for simplicity, but other shapes (e.g. circular) might be

[3]Courtesy of Sandia National Laboratories, SUMMiTTM Technologies, www.mems.sandia.gov

used to obtain different stress patterns. Fig. 2.4 shows a typical flat micromirror fabricated at Mirrorcle Technologies[4].

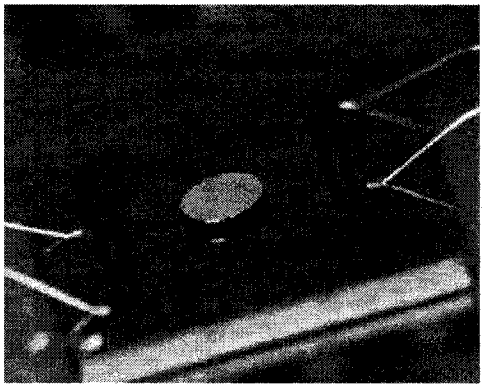

FIGURE 2.4 FLAT MIRROR FROM MIRRORCLE TECHNOLOGIES.

Deformable mirrors (DM) can change their surface shape dynamically. The deformation can be achieved by placing a set of actuating elements under a continuous membrane or by using a segmented array of mirrors. Continuous membrane mirrors have optimal fill factor and no diffraction effects, but have limited deformation range and are slower than segmented mirrors. Deformable mirrors are the main element in the emerging field of Adaptive Optics (AO). Fig. 2.5(a) shows the cross section schematic of a continuous deformable mirror and Fig. 2.5(b) shows the SEM (Scanning Electron Microscope) of a 37-segment deformable mirror developed at Iris AO[5].

2.2.1.6 Digital and Analog Micromirrors

Although the micromirror is inherently an analog system, it can be used in such a way that it is either actuated or not-actuated. This digital operation can be useful in

[4]Kind courtesy of Mirrorcle Technologies, www.mirrorcletech.com
[5]Kind courtesy of Iris AO, www.irisao.com

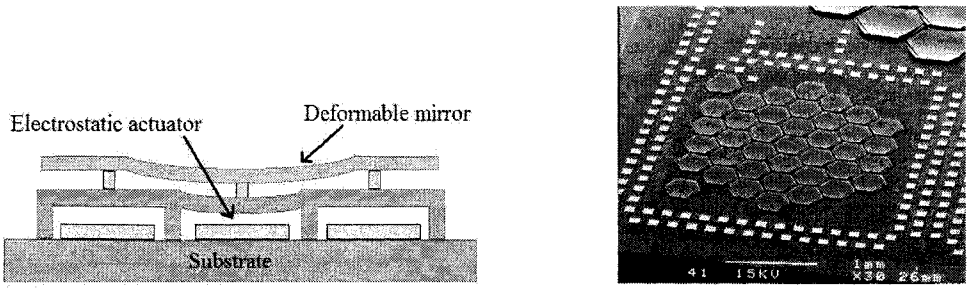

(a) (b)

FIGURE 2.5 DEFORMABLE MIRRORS: (A) CONTINUOUS MEMBRANE, (B) ARRAY.

some applications due to its repeatability and easiness of implementation, as is the case of the DLP® technology from Texas Instruments, explained in the next section.

2.2.2 Some of the Micromirror Applications

In this section some specific applications where the micromirror plays a fundamental role are described. In general, the micromirror is mostly used as a fine-pointing optical mechanism.

2.2.2.1 DLP® Projection System

The Digital Light Processing (DLP®) projection system is a novel technology designed and fabricated by Texas Instruments. It is based on an optical semiconductor chip that works as a fast light switch. This chip contains a rectangular array of up to 2 million hinge-mounted micromirrors digitally actuated. The DLP® chip is then coordinated with a digital video signal, a light source, and a projection lens to make its mirrors reflect a digital image onto a screen. Many televisions, home theater systems and business projectors currently in the market are already using DLP® technology.

2.2.2.2 Optical Switching

The optical switch is the next generation device in network connectivity. This kind of switch is based on a 2D micromirror array which permits to build large optical cross-connects that are highly reliable, fast, low loss, low power, and protocol independent. Some of these products are already in the market, for instance, the Glimmerglass Intelligent Optical Switch is shown in Fig. 2.6[6]. Basically, the optical beam is first reflected by a micromirror to a supporting mirror, then the beam is directed to another optical port by a second micromirror.

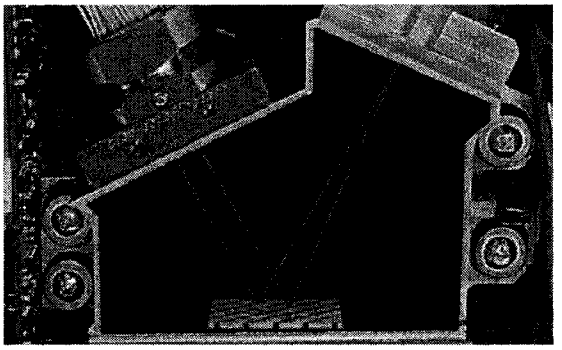

FIGURE 2.6 BASIC OPTICAL SWITCH SYSTEM.

2.2.2.3 Adaptive Optics

Adaptive optics (AO) is a novel technology whose purpose is to sense and correct the phase profile of an optical wave. The objective is to reduce the effects of varying optical aberrations. It is commonly used in astronomical telescopes to remove the effects of atmospheric distortion, but it is finding its way into new applications such as in microscopy, laser shaping and space optical communication, among others. Fig. 2.7

[6]Kind courtesy of Glimmerglass, www.glimmerglass.com

shows the AO principle and an example of its use[7]. AO works by measuring the distortion in the wavefront with the *wavefront sensor*, then the *wavefront analyzer* determines the pattern needed in the *deformable mirror* to compensate for the optical distortion. The controller closes the loop by sending the necessary information to the *actuator control* in order to drive the deformable mirror accordingly.

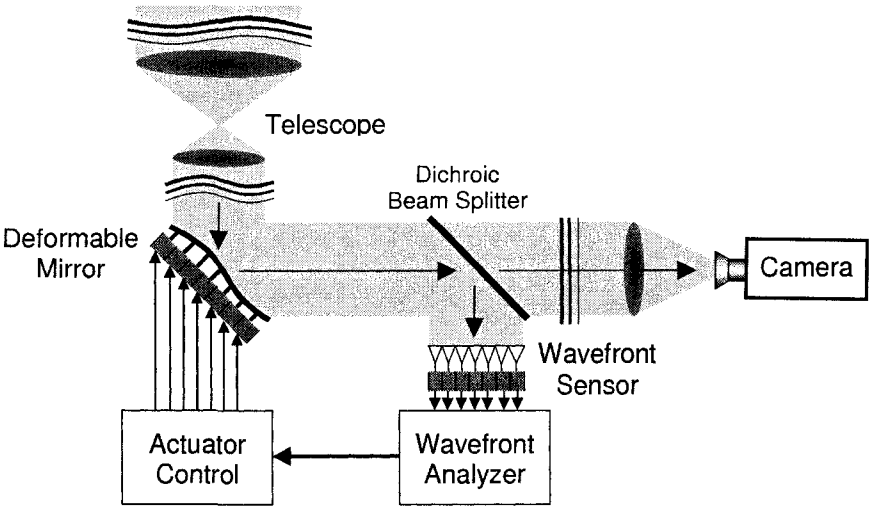

(a)

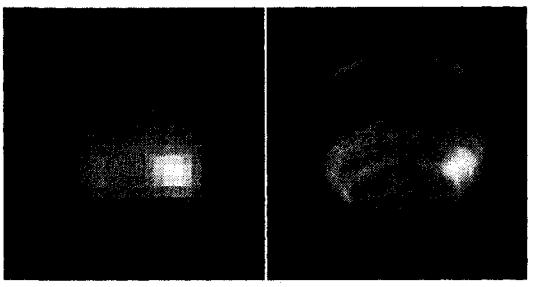

(b)

FIGURE 2.7 ADAPTIVE OPTICS: (A) PRINCIPLE, (B) IMAGE OF NEPTUNE WITHOUT AND WITH AO.

The application of micromirrors is revolutionizing several disciplines to the point where it might become of daily human use. For example, Holographic data storage of up to 4TB of disc space is now possible thanks to the properties of the micromirrors.

[7]From the *Center for adaptive Optics*

Head-mounted stereoscopic display systems are currently in development. Novel 3D display holografic systems are emerging based on micromirror arrays. Medicine procedures such as Optical tomography, Retinal scan and Laser surgery are being improved with the incorporation of this new technology. In a near future, the micromirror will even be a natural component of optical computers.

CHAPTER 3

MODELING OF TORSIONAL ELECTROSTATIC MICROMIRRORS

In the literature, a commonly used model for describing the dynamics of electrostatic micromirrors uses the charge in the mirror electrodes as a state variable (see e.g. [Senturia (2002)] and [Zhu *et al.* (2006)b], and the references therein). However, the implementation of on-chip charge measurement apparatus often results in a complex structure (see, e.g., [Anderson *et al.* (2005)]. In addition, the charge measurement is based essentially on the accumulation of the current across the actuator which is very weak for capacitive devices, usually in the order of nA. Therefore, charge measurement is prone to noise and low resolution, besides the off-set due to signal integration. Moreover, since electrostatic MEMS are actuated by high voltages, the interference between on-chip sensing and actuation might be quite strong.

A viable alternative is to choose the voltage across the device as the state variable in the control system design. As voltage measurement is straightforward for data acquisition, the implementation of the corresponding control system will be much easier. Besides, the actuation voltage ranges typically from several tens to several hundreds of volts. Hence, one can expect a much higher resolution and a higher signal-to-noise ratios. This approach has never been used previously in the literature.

The voltage-driven model proposed in this work would significantly change the structural design of micromirrors since it basically spares a sensor in the MEMS design. By doing this, the manufacturing complexity is considerably reduced and the reliability enhanced. Since the sensing electronic circuits must be closely integrated with the MEMS chip, the implementation of a control system is greatly facilitated.

This chapter addresses the modeling of torsional electrostatic micromirrors. First,

a model for the single-electrode micromirror is derived, then the dual-electrode micromirror is treated. Finally, the pull-in phenomenon is analyzed in depth.

3.1 Single-electrode Micromirror Modeling

3.1.1 Electro-Mechanical Dynamics

The device studied is the one-dimensional scanning micromirror. For simplicity, we consider a rectangular micromirror whose schematic representation is depicted in Fig. 3.1. The movable plate of the mirror is supported by two hinges, but in general, several kind of spring arrangements can be used to provide a desired angular stiffness coefficient. The device is actuated by two underneath electrodes making it possible to tilt in both clockwise and counterclockwise directions. We start investigating the modeling of this type of devices by considering the actuation with only one electrode.

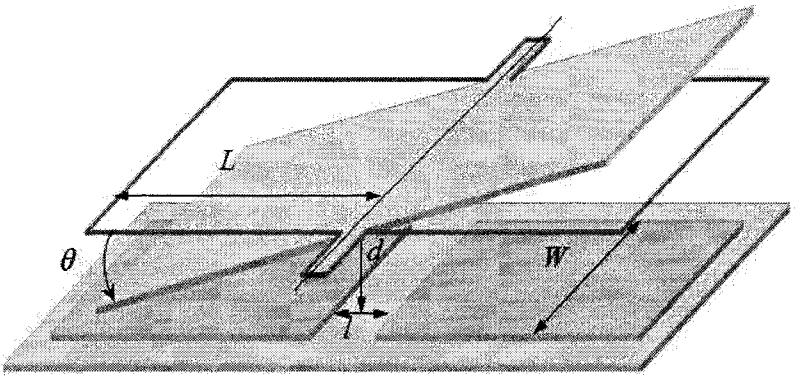

FIGURE 3.1 SCHEMATIC REPRESENTATION OF 1D MICROMIRROR.

The capacitance due to a single electrode can be expressed as

$$C_a = C_0\gamma(\theta),$$

where C_0 is a constant representing the capacitance at the flat position, that is, when no voltage is being applied. C_0 depends basically on the geometric shape of the mirror and the bottom electrode. A dimensionless function of the tilt angle $\gamma(\theta)$ is introduced to represent the variation of the capacitance. This varying capacitance approach is more convenient for modeling purposes than the usual force vector approach because the voltage is used as a state variable.

For a rectangular micromirror the air gap of this device is much smaller than its extent, therefor the fringing field effect can be ignored. The capacitance due to a single electrode can be computed as

$$\begin{aligned} C_a &= \varepsilon W \int_{L_0}^{L} \frac{dx}{d - x\sin\theta} \\ &= \frac{\varepsilon W}{\sin\theta} \ln\left(\frac{d - l\tan\theta/2}{d - L\sin\theta}\right), \end{aligned} \tag{3.1}$$

where ε is the permittivity in the air gap, W and L are, respectively, the width and the length of the electrodes, l is the distance separating the two electrodes, d is the thickness of the air gap, and the lower bound of integration is $L_0 = l/2\cos\theta$. Note that the main electrical field beyond the moving plate will be null when $L_0 > L$. The capacitance at the flat position is given by

$$C_0 = \frac{\varepsilon W L}{d}, \tag{3.2}$$

therefore the scaling function can be expressed as

$$\gamma_\theta = \frac{d}{L\sin\theta} \ln\left(\frac{d - l\tan\theta/2}{d - L\sin\theta}\right). \tag{3.3}$$

Note that $\gamma(\theta)$ has an essential discontinuity at the maximum angle $\theta_{\max} = \arcsin(d/L)$, which corresponds to the maximum angle allowed by the geometry of the mirror. Eventually, there might exist a touch angle θ_{TOUCH} that indicates the

angle at which there is a physical obstruction that prevents the mirror from attaining the maximum angle. For the single-electrode micromirror, it is typical to have $l = 0$. In this case, to find the value of γ at $\theta = 0$ (flat position), the natural logarithm can be expressed as a Taylor series. Taking into account that for small angles the approximation $\theta \approx \sin\theta$ holds, then it follows:

$$\begin{aligned}\gamma(\theta) &= \frac{d}{L} \cdot \frac{1}{\theta} \cdot \left(\frac{L}{d}\theta + \frac{L^2}{2d^2}\theta^2 + \frac{L^3}{3d^3}\theta^3 + \cdots \right) \\ &= 1 + \frac{L}{2d}\theta + \frac{L^2}{3d^2}\theta^2 + \frac{L^3}{4d^3}\theta^3 + \cdots\end{aligned}$$

It can be easily seen that $\gamma(0) = 1$, as expected, since at the flat position the capacitance is C_0. As θ increases, C_a increases from C_0 until, ideally, infinity at the maximum angle, $\theta_{\max}$. A sketch of the capacitance against the angular deflection is shown in Fig. 3.2.

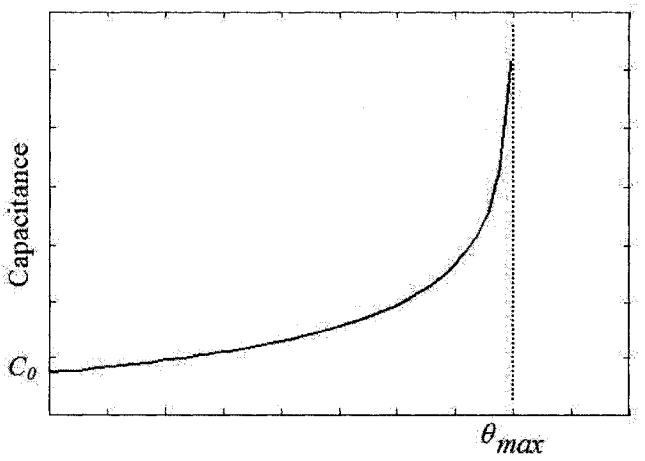

FIGURE 3.2 CAPACITANCE VS ANGLE SKETCH FOR A TORSIONAL MICROMIRROR.

The Equation of motion of a one-dimensional electrostatic torsional micromirror is

given by:

$$J\ddot{\theta} + b\dot{\theta} + k\theta = T_e, \tag{3.4}$$

where θ is the tilt angle, J is the mass moment of inertia of the moving electrode, b is the viscous damping coefficient, k is the stiffness coefficient, and T_e is the electrostatic torque. T_e is produced in this case only by one electrode and can be obtained by differentiating the stored electrical energy with respect to the angular deflection [Senturia (2002)]:

$$T_e = \frac{\partial}{\partial\theta}\left[\frac{1}{2}V_a^2 C_a\right] = \frac{1}{2}V_a^2 C_0 \frac{\partial\gamma(\theta)}{\partial\theta} = \frac{1}{2}V_a^2 C_0 \gamma'_\theta \tag{3.5}$$

where V_a is the voltage across the device.

3.1.2 Electrical Subsystems

In order to generate an electrical force, a high voltage must be supplied to the micromirror. Generally, a high voltage amplifier is used for this purpose. Since electrical parameters such as the output impedance of the amplifier have to be taken into account, the modeling of the electrical subsystems must be carried out. More details about the practical issues involved will be discussed in Chapter 6, but as far as the modeling is concerned, its treatment is developed below.

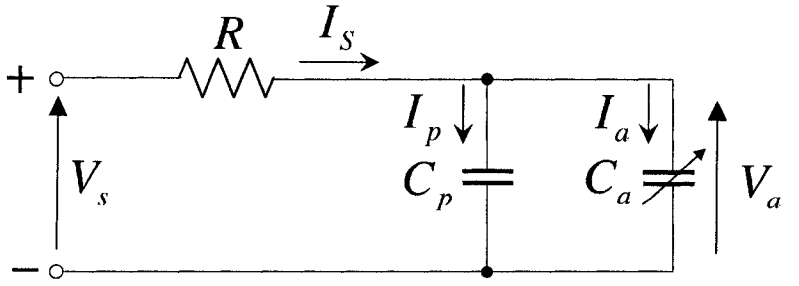

FIGURE 3.3 EQUIVALENT ELECTRICAL CIRCUIT.

The dynamics of the electrical subsystem can be deduced from the equivalent circuit

of the system shown in Fig. 3.3. When the charge on the device, Q_a, is taken as a state variable, the dynamical model of the electrical subsystem is given by:

$$\dot{Q}_a(t) = \frac{C_a}{R(C_a + C_p)} \left(V_s - \frac{Q_a}{C_a^2} \left(C_a - RC_p \dot{C}_a \right) \right), \tag{3.6}$$

where V_s is the control voltage and C_p is the parasitic capacitance, which includes the output capacitance of the voltage amplifier and the parallel parasitics due to current leak. Then, by the relationship

$$V_a = \frac{Q_a}{C_a},$$

the voltage across the device V_a is used as a state variable. This voltage is called *applied voltage* indistinctly throughout this thesis. This might add some complexity to the dynamic model as a trade for the experimental simplicity, however, its dynamical properties, such as the pull-in phenomenon, remain. Moreover, a nonlinear controller is readily justified since it takes care of any intricacies in the model. Then, it yields

$$\dot{Q}_a = C_a \dot{V}_a + \dot{C}_a V_a = C_a \dot{V}_a + C_0 \gamma'_\theta \dot{\theta} V_a$$

From (3.6) it can be deduced that

$$\dot{V}_a = \frac{V_s - V_a}{RC_0 \left(C_p/C_0 + \gamma(\theta) \right)} - \frac{\dot{\theta}\gamma'(\theta) V_a}{C_p/C_0 + \gamma(\theta)}. \tag{3.7}$$

Note that it is important to take into account the influence of the dynamics of the voltage amplifier. In particular, the output capacitance of the amplifier has the effect of slowing down the actuation transient, affecting the response time of the system. However, introducing the parallel parasitics will not affect the static behavior of the system, in particular the pull-in position remains unchanged [Chan and Dutton (2000), Degani *et al.* (1998)].

Letting $\omega = \dot{\theta}$, the angular velocity of the micromirror, and defining $\rho = C_p/C_0$, then

using (3.4) and (3.7) the system model can be expressed in state-space form as :

$$\dot{\theta} = \omega \tag{3.8a}$$

$$\dot{\omega} = \frac{1}{J}\left(-b\omega - k\theta + \frac{C_0}{2}\gamma'_\theta V_a^2\right) \tag{3.8b}$$

$$\dot{V}_a = \frac{1}{\rho + \gamma_\theta}\left(\frac{V_s - V_a}{RC_0} - \omega\gamma'_\theta V_a\right) \tag{3.8c}$$

valid in the restricted state space $\mathcal{X} = \{(\theta, \omega, V_a) \subset \mathbb{R}^3 | \theta \in [0, \theta_{\max})\}$.

3.2 Dual-electrode Micromirror Modeling

3.2.1 Electro-Mechanical Dynamics

In the modeling of dual-electrode micromirrors, it is assumed that the geometry of the two actuation electrodes and the corresponding driving circuits are identical.

In the sequel, we refer to the positive (respectively negative) electrode as the one that will produce a counterclockwise (respectively clockwise) tilt when a voltage is applied to it. Letting C_{ep} and C_{en} be the capacitances due to the positive and negative electrodes, respectively, it follows

$$\begin{aligned} C_{ep}(\theta) &= C_0\gamma(\theta), \\ C_{en}(\theta) &= C_{ep}(-\theta) = C_0\gamma(-\theta). \end{aligned}$$

Denoting $\gamma_\theta = \gamma(\theta)$ and $\gamma_{-\theta} = \gamma(-\theta)$ for notation simplicity, the total electrical

torque for the dual-electrode configuration is then given by:

$$\begin{aligned} T_e =& T_{positive} + T_{negative} \\ =& \frac{1}{2}\left(C'_{ep}(\theta)V_{ap}^2 + C'_{en}(\theta)V_{an}^2\right) \\ =& \frac{C_0}{2}\left(\gamma'_\theta V_{ap}^2 + \gamma'_{-\theta}V_{an}^2\right) \end{aligned} \tag{3.9}$$

where V_{ap} and V_{an} are the voltages across the positive and the negative electrodes. Typical curves of the function γ and its derivative are illustrated in Fig. 3.4.

The Equation of motion of the dual-electrode torsional micromirror is given, then, by:

$$J\ddot{\theta} + b\dot{\theta} + k\theta = T_e = \frac{C_0}{2}\left(\gamma'_\theta V_{ap}^2 + \gamma'_{-\theta}V_{an}^2\right), \tag{3.10}$$

where J is the mass moment of inertia of the movable electrode, b is the viscous damping coefficient, and k is the stiffness coefficient, as assigned before for the single-electrode electrostatic micromirror.

3.2.2 Electrical Subsystems

The dynamics of the electrical subsystem for dual electrodes can be expressed by a generalized form of (3.7). Hence, it is straightforward to obtain from (3.7) and (3.10) that

$$\dot{\theta} = \omega \tag{3.11a}$$

$$\dot{\omega} = \frac{1}{J}\left(-b\omega - k\theta + \frac{C_0}{2}\left(\gamma'_\theta V_{ap}^2 + \gamma'_{-\theta}V_{an}^2\right)\right) \tag{3.11b}$$

$$\dot{V}_{ap} = \frac{1}{\rho + \gamma_\theta}\left(\frac{V_{sp} - V_{ap}}{RC_0} - \omega\gamma'_\theta V_{ap}\right) \tag{3.11c}$$

$$\dot{V}_{an} = \frac{1}{\rho + \gamma_{-\theta}}\left(\frac{V_{sn} - V_{an}}{RC_0} - \omega\gamma'_{-\theta}V_{an}\right) \tag{3.11d}$$

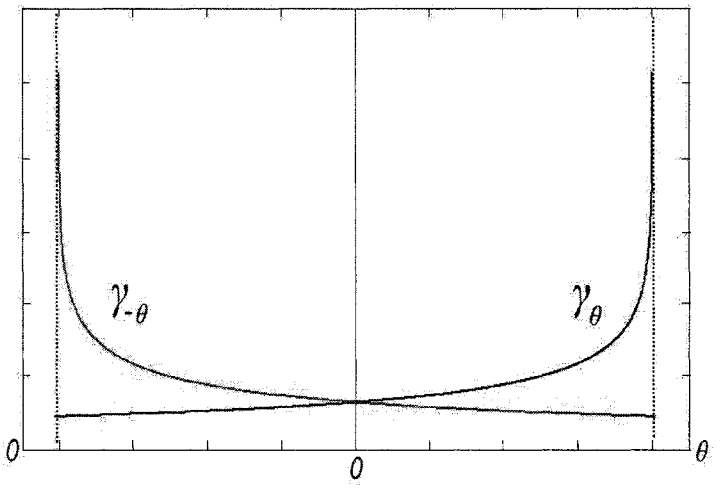

(a)

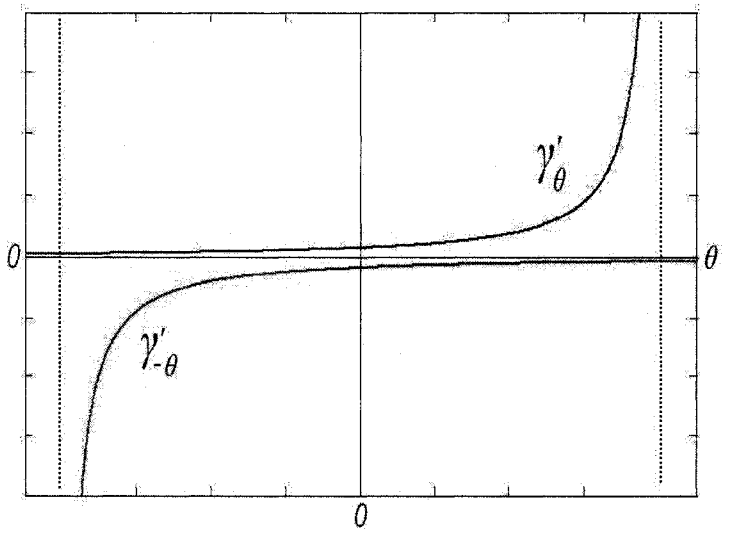

(b)

FIGURE 3.4 CAPACITANCE SKETCH FOR BOTH ELECTRODES: (A) γ FUNCTION, (B) γ FUNCTION'S DERIVATIVE.

where V_{sp} and V_{sn} are the control signals for the positive and the negative electrode, respectively. System (3.11) is valid in the restricted state space $\mathcal{X} = \{(\theta, \omega, V_{ap}, V_{an}) \subset \mathbb{R}^4 | \theta \in (-\theta_{\max}, \theta_{\max})\}$.

It is noted that the models derived for the single and dual micromirror are generic and can be used for any mirror shape. The only difference is the expression of the capacitance as a function of the tilt angle. This generic property is an advantage of the capacitance-based modeling approach.

3.3 Pull-in Phenomenon in Electrostatic Micromirrors

Due to the high nonlinearity of the dynamic model of electrostatic micromirrors, some complex and interesting phenomena arise. In this section, the single-electrode electrostatic micromirror model given by (3.8) is analyzed. Same results hold for the dual-electrode system.

The equilibrium points of the system are obtained by making the derivatives equal to zero. In Equation (3.8)

$$\begin{aligned} \omega &= 0 \\ -k\theta + \frac{C_0}{2}\gamma'_\theta V_a^2 &= 0 \\ V_a &= V_s \end{aligned} \tag{3.12}$$

From Equation (3.12) it is straightforward to note that the equilibrium point is given by the balance between the mechanical torque T_M and the electrical torque exerted on the micromirror, namely,

$$T_M = k\theta = \frac{C_0}{2}\gamma'_\theta V_s^2 = T_E \tag{3.13}$$

Since Equation (3.13) has to be solved numerically, a graphical approach can better illustrate the behaviour of the micromirror.

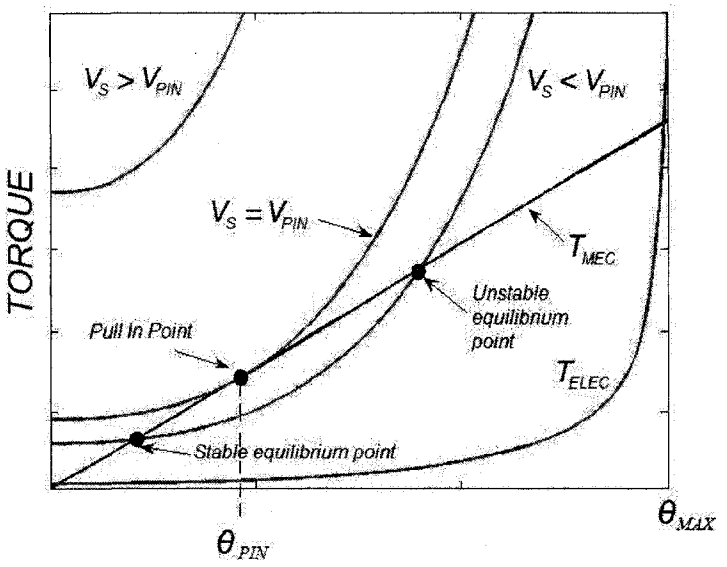

FIGURE 3.5 ELECTROSTATIC AND MECHANICAL TORQUES.

Fig. 3.5 shows the electrostatic and mechanical torques applied on the micromirror. The points where they cross are a solution to (3.13). These points are, hence, equilibrium points of the system. Mechanical and electrical torques are both functions of the tilt angle θ but the electrical one depends also on the applied voltage, which is why several curves are drawn with V_s as a parameter. In contrast to the electrical torque, which is considerably nonlinear, the mechanical torque is modeled as a linear function of θ determined by its stiffness coefficient k. The mechanical torque could be more accurately modeled as a cubic function of θ, but the dynamical properties of the micromirror would still hold.

When $V_s = 0$, $T_E = 0$, therefore there is only one cross point at $\theta = 0$. This point

corresponds to the flat position, where no voltage is applied and, hence, no torque is exerted. For $V_s > 0$, the electrical curve crosses the mechanical curve twice. Due to the torque curves' shape, the first cross point (at lower angles) occurs with the mechanical curve's slope greater than that of the electrical curve. This makes this first equilibrium point stable. As for the second cross point, the electrical curve's slope is greater, making this equilibrium point unstable. This can be analytically demonstrated by finding the eigenvalues of the Jacobian matrix of the system at the cross points.

The stability of the first equilibrium point can be seen intuitively in Fig. 3.5. If a perturbation makes the mirror increase its tilt angle slightly, then the mechanical torque becomes greater than the electrical one, which makes the mirror decrease its tilt angle and restore its stable position. If the perturbation makes the mirror decrease its tilt angle, the electrical torque becomes greater and then pulls the mirror down to restore its stable position.

When V_s reaches a certain value, namely V_{PIN}, an interesting thing happens. The electrical curve lies entirely above the mechanical curve and touches it only at one point. The previous stable equilibrium point and unstable equilibrium point fuse into just one unstable equilibrium point. This point is called the Pull-In angle θ_{PIN}. Beyond the Pull-in point, that is, with $V_s > V_{PIN}$, there are no equilibrium points at all. That means that the electrical torque dominates the mirror dynamics and only diverging trajectories occur. Physically, the micromirror at this point becomes unstable and suddenly snaps down, rushing into the bottom electrode. This is generally known as the Pull-In phenomenon.

The nonlinear behaviour described above is due to the shape of the electrical torque and does not depend on linear spring structures. Furthermore, the shape of the electrical torque does not depend on V_s. V_s modifies only its magnitude.

Then, the pull-in phenomena occurs when both torques are equal and their first derivatives are also equal as shown in Fig. 3.5. Hence, the pull-in angle satisfies not only (3.13) but also

$$k = \frac{C_0}{2}\gamma''_\theta V_a^2 \tag{3.14}$$

By combining (3.13) and (3.14), the following Equation can be used to find the pull-in angle (see [Toshiyoshi and Wu (2002)]):

$$\left.\frac{\partial\gamma(\theta)}{\partial\theta}\right|_{\theta=\theta_{PIN}} - \theta_{PIN}\left.\frac{\partial^2\gamma(\theta)}{\partial\theta^2}\right|_{\theta=\theta_{PIN}} = 0 \tag{3.15}$$

The pull-in voltage is then given by

$$V_{PIN} = \sqrt{\frac{2k\theta_{PIN}}{C_0\frac{\partial\gamma(\theta)}{\partial\theta}|_{\theta_{PIN}}}} = \sqrt{\frac{2k\theta_{PIN}}{C_0\gamma'_{\theta_{PIN}}}} \tag{3.16}$$

Later in chapter 6 equations (3.15) and (3.16) will be used to identify the real pull-in parameters of the tested micromirror.

From the point of view of bifurcation theory, V_s would be the bifurcation parameter and the bifurcation map would be the one depicted in Fig. 3.6. The dashed line and the shallow circle represent the unstable modes.

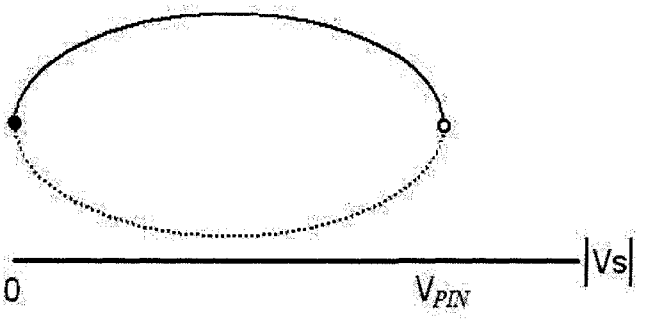

FIGURE 3.6 BIFURCATION MAP OF THE ELECTROSTATIC MICROMIRROR.

CHAPTER 4

TOOLS FOR NONLINEAR CONTROL SYSTEMS DESIGN

Although in the real world nearly every dynamical system is nonlinear in essence, linear theory is the most popular tool for tackling control system design problems. However, as dynamic behavior becomes more complex, linear theory fails to properly help in the analysis and design of nonlinear control systems. This is particularly true for the system studied in the present work, i.e., the electrostatic micromirror. Hence, nonlinear control system analysis and design tools are required in order to gain insight into the rich dynamics at hand. A rather concise overview on the tools for nonlinear system analysis and design used in this work is presented below. It must be clearly stated that the tools presented in this chapter are limited to autonomous Single-Input Single-Output (SISO) nonlinear systems unless otherwise stated. For a formal and complete presentation of nonlinear systems theory, flat systems, and the control techniques described in this chapter, the reader is referred to [Khalil (2002), Isidori (1995), Slotine and Li (1991), Fliess *et al.* (1995), Fliess *et al.* (1999), Lévine (2004)].

4.1 Nonlinear Systems

It is assumed that the dynamics of the nonlinear system has been modeled accurately enough by a finite number of coupled first-order ordinary differential equations:

$$\begin{aligned}
\dot{x_1} &= f_1\left(t, x_1, \ldots, x_n, u_1, \ldots, u_p\right) \\
\dot{x_2} &= f_2\left(t, x_1, \ldots, x_n, u_1, \ldots, u_p\right) \\
&\vdots \qquad\qquad \vdots \\
\dot{x_n} &= f_n\left(t, x_1, \ldots, x_n, u_1, \ldots, u_p\right),
\end{aligned}$$

where $\dot{x}_i$ denotes the derivative of x_i with respect to the time variable t and $u_1, \ldots, u_p$ are the p specified input variables. The variables $x_1, \ldots, x_n$ are called the state variables and they hold the actual state information of the dynamical system based on its past states and inputs.

Usually, a vector notation is used to write the n first-order differential equations in a compact form as one n-dimensional first-order vector differential equation

$$\dot{x} = f(t, x, u). \tag{4.1}$$

Sometimes, another equation

$$y = h(t, x, u)$$

is associated with (4.1), defining a q-dimensional output vector y that contains variables of particular interest in the analysis of the dynamical system. A special case of (4.1) occurs when the function f does not depend explicitly on t, then it is said to be an autonomous system. Such systems are represented by the following system of

equations:

$$\dot{x} = f(x, u), \tag{4.2}$$

$$y = h(x). \tag{4.3}$$

Where u is a single input and y is a single output. Also, The function f is frequently referred to as a *vector field* since it assigns to each point x in $\mathbb{R}^n$ a vector of $\mathbb{R}^n$.

For the system (4.2), the equilibrium points are the real roots of the equation

$$f(x, u) = 0.$$

Which is equivalent to say that the system's derivatives $\dot{x}$ are equal to zero. An equilibrium point has the property that whenever the state of the system starts at $f(x^*, u^*)$, it will remain there for all future time. An equilibrium point can be an isolated point or a continuum of points.

4.1.1 Controllability

Following, the particular case described by the state equation

$$\begin{aligned} \dot{x} &= f(x) + g(x)u \\ y &= h(x), \end{aligned} \tag{4.4}$$

with f and g being smooth vector fields on $\mathbb{R}^n$, is addressed. By smoothness of a vector field, it is meant that the function has continuous partial derivatives of any required order. The system output is y and the associated system order is n. Systems in the form (4.4) are said to be *linear in control* or *affine*. First, some basic definitions are necessary.

Definition 4.1 (Sastry (1999)) *The nonlinear system (4.4) is said to be controllable if for any two points x_0, x_1 there exists a time T and an admissible control defined on $[0, T]$ such that for $x(0) = x_0$ it follows $x(T) = x_1$.*

Definition 4.2 (Sastry (1999)) *The nonlinear system (4.4) is said to be locally controllable at x_0 if given an open subset $V \subset \mathbb{R}^n$ and $x_0, x_1 \in V$, for all $T > 0$, there exists an admissible control u on $[0, T]$ such that the system can be steered from x_0 to x_1 with $x(t) \in V$ for all $t \in [0, T]$.*

Definition 4.3 (Sastry (1999)) *Let $R_T(x_0) \subset \mathbb{R}^n$ be the subset of all the states accessible from state x_0 in time T with the trajectories confined to a neighborhood V of x_0 with u piecewise continuous on $[0, T]$. This is called the reachable set from x_0.*

Definition 4.4 (Lévine (2004)) *The system (4.4) is said to be locally accessible if for every neighborhood V of x_0, $R_T(x_0) \bigcap V$ has a nonempty interior.*

Controllability of nonlinear systems is still an active research area since guaranteing global conditions is difficult for a broad kind of nonlinear systems. Nevertheless, local accessibility can be asserted by introducing Lie Brackets even though it is a weaker property than local controllability.

Definition 4.5 (Slotine and Li (1991)) *Let $f(x)$ and $g(x)$ be two vector fields on $\mathbb{R}^n$. The Lie Bracket operation generates a new vector field defined by*

$$[f, g] = \frac{\partial g}{\partial x} f - \frac{\partial f}{\partial x} g$$

Also, higher order Lie Brackets can be defined by

$$\begin{aligned} ad_f^{\,0} g &= g, \\ ad_f^{\,1} g &= [f, g], \\ ad_f^{\,i} g &= [f, ad_f^{\,i-1} g]. \end{aligned}$$

Where the "ad" is read "adjoint". Then, the local accessibility can be asserted using the following theorem.

Theorem 4.1 (Lévine (2004)) *The n-dimensional affine nonlinear system defined by*

$$\dot{x} = f(x) + \sum_{i=1}^{m} g_i(x) u_i$$

is locally accessible at x_0 if the accessibility distribution C spans an n-dimensional space at x_0, where C is defined by:

$$C = \left[g_1, \ldots, g_m, [g_i, g_j], \ldots, ad_{g_i}^{\,k} g, \ldots, [f, g_i], \ldots, ad_f^{\,k} g_i, \ldots \right],$$

where $1 \leqslant i, j \leqslant m$, and $1 \leqslant k \leqslant n-1$. If $f(x) = 0$ and C has rank n, then the system is controllable.

The accessibility distribution C is a Lie algebra that contains all possible finite linear combinations of (i) $g_1, \ldots, g_m$; (ii) all possible iterated Lie Brackets of the $g_1, \ldots, g_m$ among themselves; and (iii) all possible iterated Lie Brackets of all the members of the sets in (i) and (ii) with $f(x)$.

Note that if a nonlinear system is linearized about x_0 and the linearization is controllable, i.e., if the system is linearly controllable, then the nonlinear system is accessible at x_0. However, the contrary is not true, if the linearization is uncontrollable the nonlinear system may still be locally accessible.

4.1.2 Observability

Definition 4.6 *The nonlinear system (4.4) is said to be observable if the knowledge of $y(t)$ on a finite time interval is sufficient to determine the initial state x_0 uniquely.*

In general, recovering the state of a nonlinear system from its output is a difficult task. Also, the choice of inputs plays a nontrivial role in reconstructing the state.

Definition 4.7 *The system is locally observable, that is distinguishable at a point x_0, if there exists a neighborhood of x_0 such that in this neighborhood,*

$$x_0 \neq x_1 \Rightarrow y(x_0) \neq y(x_1).$$

Similarly, global observability is difficult to obtain, so a local approach is pursued. To this end, the Lie derivative is introduced.

Definition 4.8 (Slotine and Li (1991)) *Let $h : \mathbb{R}^n \to \mathbb{R}$ be a smooth scalar function, and $f : \mathbb{R}^n \to \mathbb{R}^n$ be a smooth vector field on $\mathbb{R}^n$, then the Lie derivative of h with respect to f is a scalar function defined by*

$$L_f h = \langle \nabla h, f \rangle = \sum_{i=1}^{n} \frac{\partial h}{\partial x_i} \cdot f_i$$

Also, higher order Lie derivatives can be defined by

$$\begin{aligned} L_f^0 h &= h, \\ L_f^i h &= \frac{\partial}{\partial x}(L_f^{i-1} h) \cdot f = L_f L_f^{i-1} h. \end{aligned}$$

Then, the local observability for an admissible input u can be asserted using the following theorem.

Theorem 4.2 (Isidori (1995), Hermann and Krener (1977)) *Let a n-dimensional nonlinear system defined by*

$$\begin{aligned} \dot{x} &= f(x,u), \\ y &= h(x) = [h_1(x), \ldots, h_p(x)]^T. \end{aligned}$$

Let G denote the set of all finite linear combinations of the Lie derivatives of $h_1, \ldots, h_p$ with respect to $f(x)$ for all possible constant values of u. Let dG denote the set of all their gradients. If there exists n linearly independent vectors within dG, then the system is locally observable.

Being locally observable means that the output y contains enough information to reconstruct the internal state x in a local region. In general, there can be different choices for y, mainly depending on the available physical sensors, which could render the system observable or non-observable.

4.2 Exact Feedback Linearization

The main approach to the nonlinear control synthesis carried out in this work is done by means of *exact feedback linearization.* This technique is based on feedback control plus an algebraic transformation of a nonlinear system into a (fully or partially) linear one. This is completely different from the conventional Jacobian linearization (Lyapunov's indirect method) in the sense that feedback linearization is achieved by exact state transformations and feedback instead of linear approximations of the dynamics.

The state transformation can be thought of as a way to transform the original system model into an equivalent simpler one, thus making the control design easier. For instance, the idea of canceling the nonlinearities and imposing a desired linear dynamics

can be applied in a straightforward way to a class of nonlinear systems described by the so-called companion form, or controllability form. Such systems are represented by

$$x^{(n)} = a(x) + b(x)u, \tag{4.5}$$

where u is the scalar control input, x is the scalar output of interest, $x = [x, \dot{x}, \ldots, x^{(n-1)}]^T$ is the state vector, and $a(x)$ and $b(x)$ are scalar nonlinear functions of the states. By using the control input

$$u = \frac{1}{b(x)}(v - a(x)) \tag{4.6}$$

the nonlinearities can be canceled and a simpler linear relation (multiple-integrator) can be obtained

$$x^{(n)} = v. \tag{4.7}$$

This transformed linear model can then be tackled using established linear control techniques.

4.2.1 Input-State Linearization

In general, nonlinear systems do not come naturally in companion form, as is the case for electrostatic micromirrors. The more general case is described by the state-space equation (4.4). First, the following definitions are necessary:

Definition 4.9 *A function $\phi : \mathbb{R}^n \to \mathbb{R}^n$, defined in a region Ω, is called a diffeomorphism if it is smooth, and if its inverse ϕ^{-1} exists and is smooth.*

Global diffeomorphisms (when Ω is the whole space $\mathbb{R}^n$) are rare, and therefore local diffeomorphisms are often sought. It is easy to check whether a given nonlinear function $\phi(x)$ is a local diffeomorphism by using the following lemma.

Lemma 4.1 *Let $\phi(x)$ be a smooth function defined in a region Ω in $\mathbb{R}^n$. If the Jacobian matrix $\nabla\phi$ is nonsingular at a point $x = x_0$ of Ω, then $\phi(x)$ defines a local diffeomorphism in a subregion of Ω.*

A diffeomorphism is generally used to transform a system into another in terms of a new set of coordinates. Now, input-state linearization can be defined:

Definition 4.10 (Slotine and Li (1991)) *A single-input nonlinear system in the form (4.4) is said to be input-state linearizable if there exists a region Ω in $\mathbb{R}^n$, a diffeomorphism $\phi : \Omega \to \mathbb{R}^n$, and a nonlinear feedback control law*

$$u = \alpha(x) + \beta(x)v \tag{4.8}$$

such that the new state variables $z = \phi(x)$ and the new input v satisfy a linear time-invariant relation

$$\dot{z} = Az + bv, \tag{4.9}$$

where

$$A = \begin{bmatrix} 0 & 1 & 0 & \cdots & 0 \\ 0 & 0 & 1 & \cdots & 0 \\ & \vdots & & & \vdots \\ 0 & 0 & 0 & \cdots & 1 \\ 0 & 0 & 0 & \cdots & 0 \end{bmatrix}, \quad b = \begin{bmatrix} 0 \\ 0 \\ \vdots \\ 0 \\ 1 \end{bmatrix}.$$

The new state z is called the *linearizing state*, and the control law (4.8) is called the *linearizing control law*. Systems in the form (4.9) are said to be in the *Brunovski* form. Generally, not all systems in the form (4.4) are input-state linearizable. In order to investigate this matter, the next definition is introduced.

Definition 4.11 *A linearly independent set of vector fields $\{f_1, \ldots, f_m\}$ is said to be*

involutive if there exists scalar functions $\alpha_{ijk} : \mathbb{R}^n \to \mathbb{R}$ *such that*

$$[f_i, f_j](x) = \sum_{k=1}^{m} \alpha_{ijk}(x) f_k(x) \qquad \forall\ i, j.$$

Involutivity means that the Lie Bracket of any pair of vector fields from the set $\{f_1, \ldots, f_m\}$ can be expressed as a linear combination of the original set of vector fields. It is noted that constant vector fields are always involutive, as well as a set composed of a single vector.

From definition 4.11, checking if a set of vector fields $\{f_1, \ldots, f_m\}$ is involutive amounts to check if

$$rank\Big(f_1(x)\ \ldots\ f_m(x)\Big) = rank\Big(f_1(x)\ \ldots\ f_m(x)\ [f_i, f_j](x)\Big)$$

for all x and all i, j.

Then, the following theorem provides the conditions to establish if a system is input-state linearizable.

Theorem 4.3 (Slotine and Li (1991)) *The nonlinear system (4.4) is input-state linearizable if, and only if, there exists a region* Ω *such that the following conditions hold:*

- *The vector fields* $\{g, ad_f g, \ldots, ad_f^{n-1} g\}$ *are linearly independent in* Ω.
- *The set* $\{g, ad_f g, \ldots, ad_f^{n-2} g\}$ *is involutive in* Ω.

Based on theorem 4.3, once a system is proved to satisfy the input-state linearization conditions, then the first state z_1 can be found from [Slotine and Li (1991)]

$$\begin{aligned} &\nabla z_1 \; ad_f^i g = 0 \qquad i = 0, \ldots, n-2 \\ &\nabla z_1 \; ad_f^{n-1} g \neq 0, \end{aligned} \tag{4.10}$$

next the state transformation $z(x) = [z_1 \; L_f z_1 \; \ldots L_f^{n-1} z_1]^T$ can be computed. Finally, the linearizing control law can be found with

$$\begin{aligned} \alpha(x) &= -\frac{L_f^n z_1}{L_g L_f^{n-1} z_1}, \\ \beta(x) &= \frac{1}{L_g L_f^{n-1} z_1}. \end{aligned} \tag{4.11}$$

4.2.2 Input-Output Linearization and Zero-dynamics

Input-output linearization refers to the possibility of obtaining a linear input-output relation between the output y and a new input v. The basic approach is simply to differentiate the output function y repeatedly until the input u appears, then design u to cancel the nonlinearity.

Being in a region Ω in the state space, the first Lie derivative of the output y for the system (4.4) is

$$\dot{y} = \langle \nabla h, \dot{x} \rangle = \langle \nabla h, f + gu \rangle = L_f h(x) + L_g h(x) u.$$

If the input u does not appear, i.e., in the expression above $L_g h(x) = 0$ for all x in Ω, then the differentiation process can continue until for some integer r

$$y^{(r)} = L_f^r h(x) + L_g L_f^{r-1} h(x) u, \tag{4.12}$$

with $L_g L_f^{r-1} h(x) \neq 0$. Then, by applying the linearizing control law

$$u = \frac{1}{L_g L_f^{r-1} h}\big(- L_f^r h + v\big), \tag{4.13}$$

where v is the new control input, the following simple linear relation can be yielded

$$y^{(r)} = v. \tag{4.14}$$

The number of differentiations required r is called the *relative degree* of the system, and it can be shown that necessarily $r \leqslant n$. Formally,

Definition 4.12 *An autonomous SISO system is said to have relative degree r in a region Ω if, $\forall\ x \in \Omega$*

$$\begin{aligned} &L_g L_f^i h(x) = 0 \qquad 0 \leqslant i < r-1 \\ &L_g L_f^{r-1} h(x) \neq 0. \end{aligned} \tag{4.15}$$

In the special case when the output function leads to a relative degree $r = n$, the input-output linearizable system becomes input-state linearizable. It is noted that in this case (4.8) is equivalent to (4.13). On the other hand, if a system is input-state linearizable with the first new state z_1 representing the output, the system is input-output linearizable with relative degree n.

When $r < n$, by using

$$z = \begin{bmatrix} z_1 & z_2 & \dots & z_r \end{bmatrix}^T = \begin{bmatrix} y & \dot{y} & \dots & y^{(r-1)} \end{bmatrix}^T \tag{4.16}$$

in the neighborhood Ω of a point x_0, the nonlinear system (4.4) can be transformed

into the *normal form*

$$\dot{z} = \begin{bmatrix} z_2 \\ \vdots \\ z_r \\ a(z,\psi) + b(z,\psi)u \end{bmatrix} \tag{4.17a}$$

$$\dot{\psi} = w(z,\psi) \tag{4.17b}$$

with the output defined as

$$y = z_1. \tag{4.18}$$

The variables z_i and ψ_i are referred to as normal states in Ω. It is noted that the subsystem (4.17b) does not contain the system input u. Then, it can be shown that the following (local) diffeomorphism can be constructed [Slotine and Li (1991)]

$$\phi(x) = \begin{bmatrix} z_1 & \dots & z_r & \psi_1 & \dots & \psi_{n-r} \end{bmatrix}^T. \tag{4.19}$$

Hence, the normal form can be completed by using

$$\begin{aligned} a(z,\psi) &= L_f^r h(x) = L_f^r h[\phi^{-1}(z,\psi)] \\ b(z,\psi) &= L_g L_f^{r-1} h(x) = L_g L_f^{r-1} h[\phi^{-1}(z,\psi)]. \end{aligned} \tag{4.20}$$

And the vector field ψ can be found by solving the (often nontrivial) following set of partial differential equations

$$L_g \psi_j(x) = 0 \qquad 1 \leqslant j \leqslant n-r \qquad \forall\, x \in \Omega. \tag{4.21}$$

From (4.17) it can be seen that, by means of input-output linearization, the system is decomposed into an external part and an internal part. The external dynamics (Equation 4.17a) consists of a linear relation between the input u and the output y,

and can be designed to behave as desired. However, the internal dynamics (4.17b) is not affected by the input u, thus its stability plays a major role. If the internal dynamics is stable, then controlling the external dynamics will suffice, but if it is unstable, then the input-output linearization approach fails to control the system.

Generally, the internal dynamics $\dot{\psi} = w(z, \psi)$ depends on the external states z. However, an *intrinsic* property of the nonlinear system can be defined by considering the internal dynamics when the control input is such that the output y is maintained at zero. By investigating this so-called *zero-dynamics* the stability of the internal dynamics can be analyzed.

If the output y is forced to zero, so are its derivatives, then the zero-dynamics describes motion restricted to the $(n-r)$-dimensional smooth surface M_0 defined by $z = 0$. In order for the zero-dynamics to evolve in M_0, the initial state of the system must be on the surface. Furthermore, this implies that $z(0) = 0$, so the system dynamics can be simply written in normal form as

$$\dot{z} = 0 \tag{4.22a}$$

$$\dot{\psi} = w(0, \psi). \tag{4.22b}$$

By definition, Equation (4.22b) is the zero-dynamics of the nonlinear system (4.4). The control input u_0 can be written as a function only of the internal states ψ. From (4.17a)

$$u_0(\psi) = -\frac{a(0, \psi)}{b(0, \psi)}. \tag{4.23}$$

In the special case of input-state linearization, i.e. $r = n$, there is simply no internal dynamics. Hence, the stability relies completely on the external dynamics design.

For linear systems, the relative degree r is the same as the excess of poles over zeros, and the stability of the internal dynamics depends on the location of the zeros of

the transfer function. If the system is minimum phase, then all the zeros are in the left-half plane, which implies that the internal dynamics is stable independently of the initial conditions and of the magnitudes of the desired output $y_d, \ldots, y_d^{(r)}$ for the external dynamics. If at least one zero is in the right-half plane, then the internal dynamics is unstable. This kind of systems are said to be non-minimum phase.

4.2.3 Tracking Control

When using feedback linearization, at least part of the system (4.4) can be expressed in a linear form (4.14) with the new control input v. In order to track a given desired trajectory $y_d(t)$, the tracking error vector is defined as

$$\tilde{z}(t) \triangleq z(t) - z_d(t),$$

where

$$z_d \triangleq \begin{bmatrix} y_d & \dot{y}_d & \ldots & y_d^{(r-1)} \end{bmatrix}^T.$$

Then, the following result can be demonstrated [Isidori (1995)]:

Theorem 4.4 (Slotine and Li (1991)) *Assume that the system (4.4) has relative degree r, that z_d is smooth and bounded, and that the internal dynamics is uniformly asymptotically stable. Then, by using*

$$v = y_d^{(r)} - k_{r-1}\tilde{z}_r - \ldots - k_0\tilde{z}_1, \tag{4.24}$$

where the constants k_i are chosen such that the following polynomial has all its roots in the left-half plane

$$s^r + k_{r-1}s^{r-1} + \ldots + k_1 s + k_0,$$

the whole state remains bounded and the tracking error $\tilde{z}$ converges to zero exponen-

tially.

4.3 Flat Systems

This work profits form the enhanced insight offered by the relatively novel theory of flat systems. Basically, a system is said to be flat if both the states and input can expressed as a function of the output and its derivatives. This implies that the trajectories of flat systems can be parameterized without integrating the dynamic equations. This characteristic makes flat systems very interesting because it greatly simplifies analysis and control design. Flatness theory is also based on differential geometry and uses advanced mathematics tools, so it is not developed here. For a formal presentation of flat systems the reader is referred to [Fliess *et al.* (1995), Fliess *et al.* (1999), Lévine (2004), Penet (2005)]. The algebraic formulation of flatness theory is described below.

Definition 4.13 (Lévine (2004)) *Let a system be in the form (4.4) where* $x \in \mathbb{R}^n$ *and* $u \in \mathbb{R}^m$. *The system is said to be flat if there exists* $y \in \mathbb{R}^m$, *also called flat output, such that*

$$y = (y_1, \ldots, y_m) = \psi(x, u, \dot{u}, \ldots, u^{(s)}) \tag{4.25}$$

implies

$$x = \varphi_0(y, \dot{y}, \ldots, y^{(r)}), \tag{4.26}$$

$$u = \varphi_1(y, \dot{y}, \ldots, y^{(r+1)}). \tag{4.27}$$

where $\psi : \mathbb{R}^n \times (\mathbb{R}^m)^{s+1} \rightarrow \mathbb{R}^m$, $\varphi_0 : \mathbb{R}^m \times (\mathbb{R}^m)^{r+1} \rightarrow \mathbb{R}^n$, *and* $\varphi_1 : \mathbb{R}^m \times (\mathbb{R}^m)^{r+2} \rightarrow \mathbb{R}^m$.

Formally, the dimension of the state vector in the new coordinates is increased from n to r. Indeed, the state of a system represents the set of parameters such that if they are known, then every possible information about the system can be obtained. Flat systems theory treats outputs, inputs, and internal states indifferently as sources of information about the system. Then, having y and its $r+1$ derivatives is enough to know the system, since $x(t)$ and $u(t)$ can be found using φ_0 and φ_1. In other words, if the states and the input can be expressed as functions of the output and its derivatives, then the system is flat.

4.3.1 Properties of Flat Systems

Following, several useful properties of flat systems are stated.

Property 4.1 *Given a flat system, the number of elements of a flat output is equal to the number of independent inputs. From above, y will have m elements.*

Property 4.2 *The flat output is not unique.*

Property 4.3 *Every flat system is locally accessible.*

Property 4.4 *A linear system is flat if, and only if, it is controllable.*

The following definitions are necessary to state the next property:

Definition 4.14 *A **static** state feedback is a closed-loop control law of the form*

$$u(t) = \alpha(x) + \beta(x)v,$$

where v is the new reference. That is, u depends only on the states and on certain external magnitudes (e.g. reference values, parameters).

For instance, the input-state linearization technique described in section 4.2.1 is a static state feedback.

Definition 4.15 *A **dynamic** state feedback is a closed-loop control law of the form*

$$u(t) = \alpha(x, z, v),$$
$$\dot{z} = \beta(x, z, v).$$

That is, u is the output of a dynamical system whose input depends on the states and on certain external magnitudes.

Property 4.5 *Every flat system is linearizable by dynamic state feedback. Inversely, every system linearizable by dynamic state feedback is flat.*

This property clearly illustrates that flatness is larger than static state feedback linearization, since static state feedback is a subset of dynamic state feedback.

Even though in the case of single input systems ($m = 1$) flatness is equivalent to static state feedback linearization, it is in the case of multiple inputs, where static feedback and dynamic feedback are not equivalent anymore, where the flatness property reveals all its strength. Indeed, systems can be found (e.g. VTOL aircraft, non-holonomic vehicle) that can not be linearized by static feedback, but are, nevertheless, flat.

4.3.2 Control of Flat Systems

In this section, the general guideline to design a controller for a SISO flat system is described.

Initially, a flat output must be found. Unfortunately, there is no procedure to find flat outputs or criteria to assert their existence. However, in most physical systems the

flat output has a physical meaning, which is convenient since in practice the output can be directly measured. In the case of the electrostatic micromirror, it will be shown in chapter 5 that the angle θ is a flat output.

Then, using a change of coordinates plus a suitable feedback control, the system can be put into the Brunovsky canonical form. This can be done via a diffeomorphism $y = \phi(x)$ where the new coordinates are the output and its derivatives. Once the system is in the Brunovski form, linear system control theory can be used to design a control law for v. Then, a tracking control approach as described in section 4.2.3 can be applied. To this end, depending on the control objective, a reference trajectory must be specified. The next section deals with this matter.

4.3.3 Trajectory Planning

In order to apply tracking control, a reference trajectory $y_d(t)$ and its derivatives must be available. Such trajectory can be expressed by any suitable function since it does not need to satisfy any differential equation, so it can be simply constructed, for example, by polynomial interpolations [Lévine (2004)], so as to take the system from an initial point x_i in state space at time t_i to a desired point x_f in state space at time t_f. A sufficiently smooth trajectory $t \rightarrow y_d(t)$ at least $(r+1)$ times differentiable needs to be found such that the initial and final conditions are verified. In this section, the construction of trajectories for single-input/single-output (SISO) systems is considered. The trajectory specifications given at time t_i,

$$y(t_i), \ldots, y^{(r+1)}(t_i)$$

and those at time t_f,

$$y(t_f), \ldots, y^{(r+1)}(t_f)$$

define a total of $2(r+2)$ conditions for the output $y_d(t)$. Denoting $T = t_f - t_i$ and $\tau(t) = (t - t_i)/T$, the desired trajectory $y_d(t)$ can then be expressed as a polynomial of time of order equal to $2r+3$:

$$y_d(t) = \sum_{k=0}^{2r+3} a_k \tau^k(t). \tag{4.28}$$

By differentiating $y_d(t)$ $(r+1)$ times and imposing the initial conditions, the first $r+2$ coefficients $a_0, \ldots, a_{r+1}$ are given by

$$a_k = \frac{T^k}{k!} y^{(k)}(t_i), \qquad k = 0, \ldots, r+1, \tag{4.29}$$

while the remaining $r+2$ coefficients are determined by the initial and final conditions and are given by

$$\begin{pmatrix} 1 & 1 & \cdots & 1 \\ r+2 & r+3 & \cdots & 2r+3 \\ (r+1)(r+2) & (r+2)(r+3) & \cdots & (2r+2)(2r+3) \\ \vdots & \vdots & \cdots & \vdots \\ (r+2)! & \dfrac{(r+3)!}{2} & \cdots & \dfrac{(2r+3)!}{(2r+2)} \end{pmatrix} \begin{pmatrix} a_{r+2} \\ \vdots \\ a_{2r+3} \end{pmatrix}$$

$$= \begin{pmatrix} y(t_f) - \sum_{l=0}^{r+1} \frac{T^l}{l!} y^{(l)}(t_i) \\ \vdots \\ T^k \big(y^{(k)}(t_f) - \sum_{l=k}^{r+1} \frac{T^{l-k}}{(l-k)!} y^{(l)}(t_i) \big) \\ \vdots \\ T^{r+1} \big(y^{(r+1)}(t_f) - y^{(r+1)}(t_i) \big) \end{pmatrix}. \tag{4.30}$$

This trajectory planning can be applied to construct set-point references. In this case, the derivatives of the reference trajectory should vanish at the initial and final

positions, $y(t_i)$ and $y(t_f)$, and hence, the desired trajectory becomes

$$y_d(t) = y(t_i) + \big(y(t_f) - y(t_i)\big)\tau^{r+2}(t)\sum_{k=0}^{r+1} a_k \tau^k(t), \tag{4.31}$$

where the coefficients $a_0, \ldots, a_{r+1}$ can be obtained by solving the following linear equation:

$$\begin{pmatrix} 1 & 1 & \cdots & 1 \\ r+2 & r+3 & \cdots & 2r+3 \\ (r+1)(r+2) & (r+2)(r+3) & \cdots & (2r+2)(2r+3) \\ \vdots & \vdots & \cdots & \vdots \\ (r+2)! & \dfrac{(r+3)!}{2} & \cdots & \dfrac{(2r+3)!}{(2r+2)} \end{pmatrix} \begin{pmatrix} a_0 \\ a_1 \\ \vdots \\ a_{r+1} \end{pmatrix} = \begin{pmatrix} 1 \\ 0 \\ \vdots \\ 0 \end{pmatrix}. \tag{4.32}$$

As all the time derivatives of $y(t)$ vanish at the equilibria, a finite number of null initial and final conditions can be added above the $(r+1)$ high order derivatives without changing the initial and final positions. In this way, smoother trajectories can be achieved. This is particularly useful in practice if oscillating modes are to be avoided.

CHAPTER 5

CONTROL SYNTHESIS FOR ELECTROSTATIC MICROMIRRORS

This chapter presents the control synthesis for both single and dual electrostatic torsional micromirrors. The dynamic models developed in Chapter 3 are the starting point for the controllers design. The techniques employed are based on the tools described in Chapter 4.

The closed-loop controllers design combines techniques of exact feedback linearization and trajectory planning and deals with different types of operations, such as scanning control and set-point control. The design takes advantage of the flatness-based control, in which the desired performance can be specified through the appropriate choice of a reference trajectory, allowing the control system tuning to be carried out in a systematic way. The performance of the proposed control schemes is verified first by simulation and later, in chapter 6, by means of an experimental setup consisting of low-cost generic platform and hardware.

5.1 Controller Design for the Single-electrode Micromirror

In this section the design of a nonlinear controller for the system (3.8) is carried out. In order to do so, the controllability properties of the single micromirror are investigated first. These properties establish the feasibility and possible limitations of any controller. The observability of the system is also explored. Since the designed controller is to be implemented, the reconstruction of the system states from the measured output has to be guaranteed.

5.1.1 Accessibility and Observability

In general, the controllability properties for nonlinear systems are difficult to establish, that is why a weaker condition, namely the accessibility, is investigated instead. This can be done using theorem 4.1 by noting that the system (3.8) is of the form:

$$\dot{x} = f(x) + g(x)u \tag{5.1}$$

with $x = [\theta\ \omega\ V_a]^T$, $u = V_s$, and

$$f(x) = \begin{bmatrix} \omega \\ -\frac{b}{J}\omega - \frac{k}{J}\theta + \frac{C_0}{2J}\gamma'_\theta V_a^2 \\ -\frac{V_a}{RC_0(\rho+\gamma_\theta)} - \frac{\omega\gamma'_\theta V_a}{(\rho+\gamma_\theta)} \end{bmatrix}, \quad g(x) = \begin{bmatrix} 0 \\ 0 \\ \frac{1}{RC_0(\rho+\gamma_\theta)} \end{bmatrix}. \tag{5.2}$$

Then, the accessibility distribution matrix is given by

$$C = \begin{bmatrix} g(x) & [f(x), g(x)](x) & ad_f^2 g(x) \end{bmatrix}. \tag{5.3}$$

The second column in C is given by

$$[f(x), g(x)](x) = \begin{bmatrix} 0 & -\frac{\gamma'_\theta V_a}{RC_0(\rho+\gamma_\theta)} & \frac{1}{R^2C_0^2(\rho+\gamma_\theta)^2} \end{bmatrix}^T. \tag{5.4}$$

Hence, the only way for C to not be singular for all x is that the first line has a nonzero term in its third position. The term (1,3) in C is given by

$$C(1,3) = -\frac{\gamma'_\theta V_a}{RJ(\rho+\gamma_\theta)}. \tag{5.5}$$

Since every factor in (5.5) is nonzero except for V_a, it can be seen that if V_a is zero the system is not accessible. The point where V_a is zero is called the flat position. Since the system is accessible everywhere else, a controller can then be designed to

operate in the whole range of operation except for the flat position.

As for observability, the only state not measured because of practical considerations is the angular velocity ω. So, the question arises as if by measuring the angle θ and the applied voltage V_a there is enough information about the angular velocity throughout the whole state space. To address this matter, local observability can be investigated by means of theorem 4.2. The output function is defined as

$$y = h(x) = \begin{bmatrix} h_1(x) \\ h_2(x) \end{bmatrix} = \begin{bmatrix} \theta \\ V_a \end{bmatrix}$$

Then, since the order of the system (3.8) is three, it suffices to obtain three linearly independent gradient vectors out of the set of all finite linear combinations of the Lie derivatives of the output y. Hence, The matrix G can be constructed as

$$G = \begin{bmatrix} L_f^0 h_1 \\ L_f^1 h_1 \\ L_f^0 h_2 \end{bmatrix} = \begin{bmatrix} h_1 \\ L_f h_1 \\ h_2 \end{bmatrix} = \begin{bmatrix} \theta \\ \omega \\ V_a \end{bmatrix}.$$

Next, the gradient is easily found to be

$$dG = \begin{bmatrix} 1 & 0 & 0 \\ 0 & 1 & 0 \\ 0 & 0 & 1 \end{bmatrix},$$

which is full rank. Subsequently, it can be concluded that the system is locally observable. Then, by measuring the tilt angle θ and the applied voltage V_a the reconstruction of the state vector can be guaranteed.

5.1.2 Control Synthesis

Once controllability and observability conditions are established, the design of the controller for the single micromirror can be carried out. The closed-loop control system diagram is shown in Fig. 5.1. The input and output signals of every block are indicated so as to better follow the design procedure. The whole state vector $x = [\theta\ \omega\ V_a]^T$ is considered available in order to obtain the linearizing state z, the linear tracking control law v, and the linearizing control law V_s.

The diffeomorphism $z(x)$ can then be found by computing the time derivatives of the output until the input appears. Then, using (3.8) yields

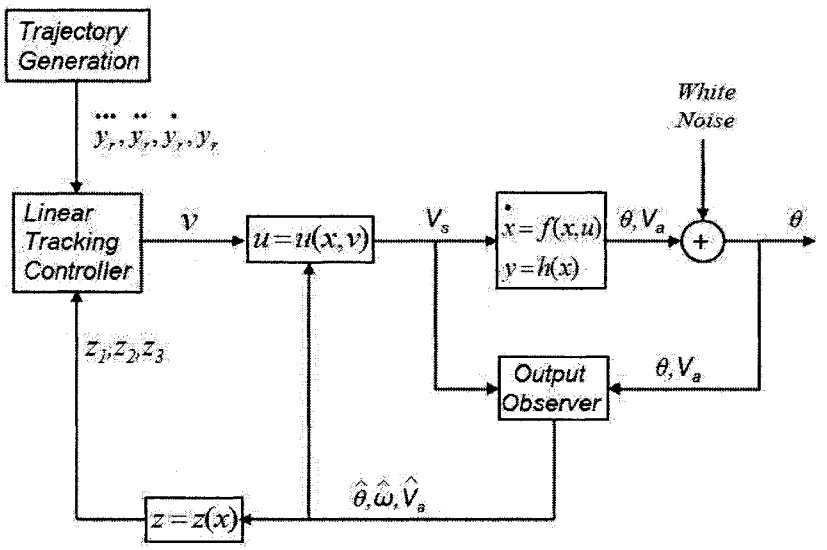

FIGURE 5.1 CLOSED-LOOP CONTROL SYSTEM DIAGRAM.

$$y = \theta \tag{5.6a}$$

$$\dot{y} = \dot{\theta} = \omega \tag{5.6b}$$

$$\ddot{y} = \dot{\omega} = \frac{1}{J}\left(-b\omega - k\theta + \frac{C_0}{2}\gamma'_\theta V_a^2\right) \tag{5.6c}$$

$$\dddot{y} = \ddot{\omega} = -\frac{b}{J}\dot{\omega} - \frac{k}{J}\dot{\theta} + \frac{C_0}{2J}\left(\gamma'_\theta 2V_a\dot{V}_a + V_a^2\gamma''_\theta\dot{\theta}\right), \tag{5.6d}$$

where $\gamma''(\theta) = \partial^2\gamma(\theta)/\partial\theta^2$. From (5.6c), V_a^2 can be expressed as

$$V_a^2 = \frac{2}{C_0\gamma'(\theta)}\left(J\ddot{\theta} + b\dot{\theta} + k\theta\right). \tag{5.7}$$

Since all the state variables θ, ω, and V_a, as well as the input V_s, can be expressed as algebraic functions of the output and its time derivatives, it can be concluded that the system described by (3.8) is flat with θ as output, [Fliess *et al.* (1995)].

At this point a distinction has to be made. Strictly speaking, it is the square of V_a that can be expressed as an algebraic function of the output and its time derivatives. This implies that there are two possible branches in the new set of coordinates, the positive and the negative square root of V_a. In this work only the positive square root is employed. Moreover, the variable V_a is never let to be zero. The point where V_a becomes zero, i.e. the flat position, presents an ambiguity, which is why the system is not linearly controllable at this point. Obviously, the system is not flat at this point.

The system (3.8) can hence be put into the Brunovsky canonical form via the diffeomorphic change of coordinates $z(x)$. That is, it can be transformed from (θ, ω, V_a) to

(z_1, z_2, z_3) with

$$\begin{aligned} \dot{z_1} &= z_2 \\ \dot{z_2} &= z_3 \\ \dot{z_3} &= v \\ y &= z_1 = \theta. \end{aligned} \tag{5.8}$$

From (5.6d) it is easily seen that the input v corresponds to:

$$v = \dddot{\theta} = -\frac{b}{J}\dot{\omega} - \frac{k}{J}\dot{\theta} + \frac{C_0}{J}\gamma'_\theta V_a \left[\frac{1}{\rho + \gamma_\theta}\left(\frac{V_s - V_a}{RC_0} - \omega\gamma'_\theta V_a\right)\right] + \frac{C_0}{2J}V_a^2\gamma''_\theta\dot{\theta}, \tag{5.9}$$

where (3.8c) has been included. Then, after some development, the linearizing feedback control law V_s can be deduced as

$$V_s = \frac{R}{\gamma'_\theta V_a}(\rho + \gamma_\theta)\left(Jv + b\ddot{\theta} + k\dot{\theta}\right) + V_a\left(1 + RC_0\gamma'_\theta\dot{\theta} - \frac{RC_0\gamma''_\theta\dot{\theta}(\rho + \gamma_\theta)}{2\gamma'_\theta}\right). \tag{5.10}$$

It can be seen from (5.10) that the linearizing feedback control law V_s is singular when $V_a = 0$. This is due to the fact that System (3.8) is not linearly controllable at this point. In the implementation of this control law an ad-hoc artifice for avoiding the singularity will be used, which consists in applying a small bias voltage to keep the operational point away from the uncontrollable point. This bias voltage will not affect significantly the operational range of the device, since the micromirror deflection is not very sensitive to the applied voltage near the flat position, i.e., the bias voltage will only make the micromirror tilt a relatively small angle.

Tracking control can be tackled through the linearized system (5.8). Let $e = y - y_r$ be the tracking error and $y_r(t)$ be the desired trajectory. In order to track the desired

trajectory, y_r, it suffices to choose v as

$$v = \dddot{y}_r - k_2\left(\ddot{\theta} - \ddot{y}_r\right) - k_1\left(\dot{\theta} - \dot{y}_r\right) - k_0\left(\theta - y_r\right), \tag{5.11}$$

which can also be written as

$$v = \dddot{y}_r - k_2\left(z_3 - \ddot{y}_r\right) - k_1\left(z_2 - \dot{y}_r\right) - k_0\left(z_1 - y_r\right). \tag{5.12}$$

Then the tracking error, $e = \theta - y_r$, satisfies

$$\dddot{e} + k_2\ddot{e} + k_1\dot{e} + k_0 e = 0, \tag{5.13}$$

which is the characteristic Equation of an asymptotically stable linear system provided $s^3 + k_2 s^2 + k_1 s + k_0$ is a Hurwitz polynomial.

The selection of the gains for the linear tracking controller in (5.12) is usually made from performance requirements. However, it is often not evident how the performance specified in the the linearized coordinates (5.8) will affect that in the original coordinates. In the absence of any specific consideration, this parameters can be chosen in a way that the location of closed-loop poles satisfies the Butterworth configuration. The control is then optimal in the sense of control effort. The closed-loop poles will tend to radiate out from the origin along the spokes of a wheel in the left half-plane. The third-order Butterworth polynomial is

$$B_3(p) = p^3 + 2p^2 + 2p + 1,$$

where $p = s/\Omega$ and Ω is the radius of the circle on which the poles are placed. The corresponding pole locations are shown in Fig. 5.2. The controller gains are then given by

$$k_0 = \Omega^3; \quad k_1 = 2\Omega^2; \quad k_2 = 2\Omega,$$

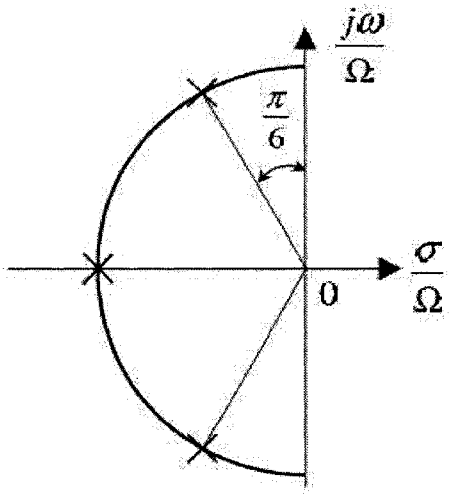

FIGURE 5.2 POLE LOCATION FOR 3TH ORDER BUTTERWORTH POLYNOMIAL.

with Ω becoming the tuning parameter.

In this work, the set-point control reference trajectory used is based on the trajectory planning algorithm described in section 4.3.3, which results in a polynomial of the following form [Lévine (2004)]:

$$y_r(t) = \theta(t_i) + (\theta(t_f) - \theta(t_i))\tau^5(t) \sum_{i=0}^{4} a_i \tau^i(t), \tag{5.14}$$

where $\theta(t_i)$ is the initial tilt angle at time t_i, $\theta(t_f)$ is the desired tilt angle at time t_f, and $\tau(t) \triangleq (t - t_i)/(t_f - t_i)$. The coefficients in (5.14) can be determined by imposing the initial and final conditions

$$\dot{\theta}(t_i) = \dot{\theta}(t_f) = \ddot{\theta}(t_i) = \ddot{\theta}(t_f) = \theta^{(3)}(t_i) = \theta^{(3)}(t_f) = 0,$$

which yields $a_0 = 126$, $a_1 = -420$, $a_2 = 540$, $a_3 = -315$, and $a_4 = 70$.

5.1.3 Simulation

The control law developed in the previous section is validated by means of numerical simulations via Matlab/Simulink®. Table 5.1 shows the parameters of the micromirror used in simulation. In order to make the simulation as realistic as possible, the effect of quantization and measurement noise was taken into account. A fixed-step solver cycling at $40\mu s$ is used.

The controller parameter Ω was set to 25000. This high value is justified by the rather fast micromirror used. The angle resolution and the voltage resolution set for the quantizers were $1, 2mdeg$ and $0.2V$ respectively. White noise with zero mean was used for the angle output θ and the applied voltage V_a with variances of $\pm 10mdeg$ and $\pm 2V$ respectively.

TABLE 5.1 SIMULATION PARAMETERS.

Parameter	**Value**
Mirror width W	500 (μm)
Mirror length L	250 (μm)
Air gap d	12 (μm)
Stiffness coefficient k	3.9 10^{-6} (N/rad)
Maximum angle range $\theta_{\max}$	$\sim 2.7°$
Pull in angle θ_{PIN}	$\sim 1.2°$
Pull in voltage V_{PIN}	$\sim 280V$
Output resistance R	100 (Ω)
Parasitic capacitance C_p	3.0×10^{-7} (F)

Fig. 5.3 shows the output θ for different set-points. It can be seen that the developed controller makes the mirror angle follow the reference trajectory flawlessly, hence delivering the desired dynamic response. This confirms the main strength of the exact feedback linearization technique for perfect models.

Figure 5.4 shows the corresponding control signals V_s. To avoid the singularity at the zero-voltage position, a small bias voltage of $10V$ is applied, making the initial angle

unnoticeably greater than zero (see beginning of the curves in Fig. 5.3). Although quite smooth, it is seen that the control signal shows some variations near the uncontrollable point (flat position). It is worth remarking that for the 2.5° set-point, the control signal starts to shake, that is, to lose numeric stability. This is mainly because of the noise and slow sample time, and would not happen had the noise been removed and a faster sample time used.

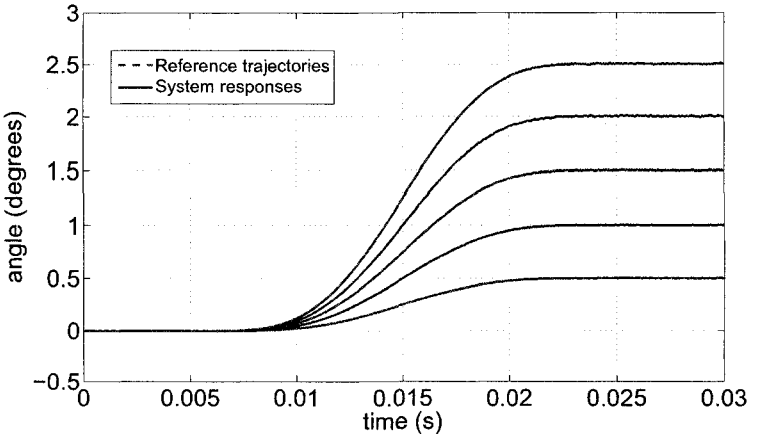

FIGURE 5.3 CLOSE-LOOP SET-POINT CONTROL: SYSTEM RESPONSES AND REFERENCE TRAJECTORIES.

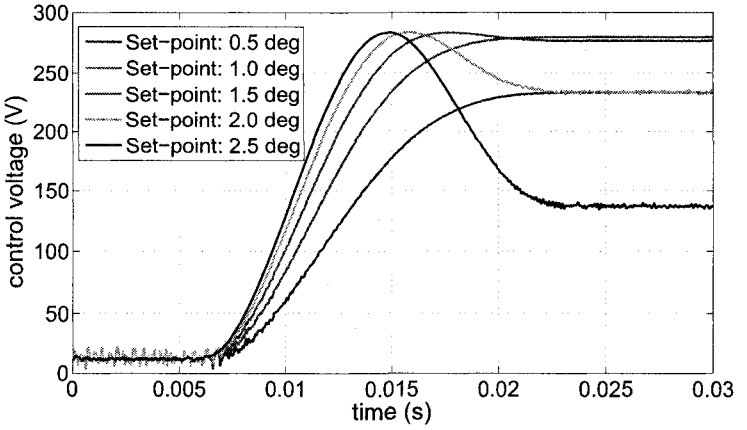

FIGURE 5.4 CONTROL SIGNALS FOR SET-POINT CONTROL TRAJECTORIES.

Figure 5.4 also reveals the nonlinearities in the electrostatic micromirror model. In

order to drive the mirror angle beyond the pull-in point, the control signal has to cross the pull-in voltage and then decrease its value accordingly to maintain the mirror angle stable.

As shown by simulation, the designed nonlinear controller smoothly operates the micromirror through the whole gap, improving the system performance in terms of transient response and precision.

5.2 Controller Design for the Dual-electrode Micromirror

This section presents the controller design for the dual-electrode electrostatic micromirror. For this purpose, differential actuation is introduced. Its role in avoiding the singularity at the flat position and reducing the control effort is discussed. Next, the control synthesis is carried out.

5.2.1 Differential Actuation

Many torsional micromirrors make use of the driving scheme involving multiple electrodes. In the case of the dual micromirror, two bottom electrodes are used to drive the micromirror both ways. This configuration increases the operational range by incrementing the number of inputs: one control signal per electrode. However, the system continues to be uncontrollable at the flat position as long as the applied voltage is zero, as is the case for system (3.11).

A schematic of the differential configuration for one-dimensional torsional micromirrors is shown in Fig. 5.5. One advantage of using such an actuation mechanism is that it allows to implement the so-called torque amplification (see, e.g., [Hornbeck (1990), Pareek *et al.* (2005)]. This configuration produces an enhanced electrical torque as the active signal is shifted by the bias voltage to a steeper region on the

voltage actuation curve (see Fig. 5.6), making the micromirror more sensitive to the span of the actuation signal and hence, helping to reduce the amplitude of the active control signal.

According to Fig. 5.5, the drive voltages under the differential bias configuration become

$$V_{sp} = V_B + V_M, \tag{5.15a}$$

$$V_{sn} = V_B - V_M, \tag{5.15b}$$

where V_{sp} and V_{sn} are the voltages applied to the right and left electrode respectively, V_B is a bias voltage, and V_M is the active control signal. As (5.15) states, the differential scheme also reduces the number of inputs from two to one. This means that a degree of freedom is lost since one electrode can not be operated independently from the other, however the design is greatly simplified.

Another benefit of using a differential actuation scheme in open-loop is that in a small range around the zero-deflection position it can make the deflection of the mirror mostly linear with respect to the actuation voltage. This improves the input-to-output linearity of the device (see, e.g., [Uchimaru *et al.* (1998), Toshiyoshi *et al.* (2001)], making this method widely used in open-loop control schemes. However, the linearization by means of differential actuation is valid only for very small deflections and is by all means approximate. Furthermore, the constant bias voltage applied in the differential scheme causes a spring softening effect that makes the pull-in angle decrease, shortening the stable range of the micromirror [Pareek *et al.* (2005)].

By applying nonlinear control techniques it is possible to explore the full potential offered by differential actuation. The control system can take advantage of the reduction of the active control signal range while achieving a stable operation through the whole gap. Furthermore, by using a differential scheme, the uncontrollability at

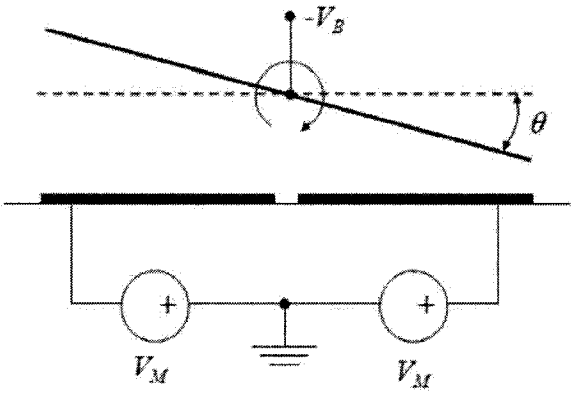

FIGURE 5.5 SCHEMATIC CROSS SECTION OF ANGULAR ACTUATOR WITH A DIFFERENTIAL BIAS CONFIGURATION.

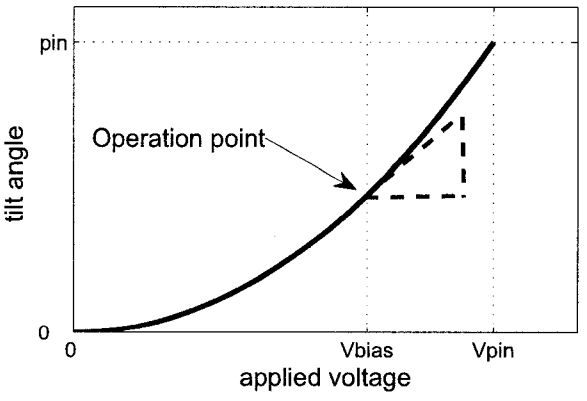

FIGURE 5.6 TYPICAL VOLTAGE ACTUATION CURVE.

the flat position can be avoided.

From an implementation point of view, differential actuation permits the control system to generate only the active signal V_M while the bias voltage V_B can be generated by an external power supply and needs not to be an intrinsic part of the system, thus reducing the voltage range of the control signal drive. This helps to integrate readily the control system into the embedded actuation system of a final application because the specifications for the actual electrical drive system are less demanding.

5.2.2 Controllability at the Flat Position

It has been shown in section 5.1.1 that the system (3.8) at the flat position is not linearly controllable for single actuation schemes (see, e.g., [Maithripala *et al.* (2005)a, Agudelo *et al.* (2007)]). Hence, the control law obtained is singular at this point. Differential actuation provides the means of getting around the uncontrollability at the flat position by introducing a bias voltage and a linked active signal.

The linear controllability of System (3.11) using the differential scheme (5.15) at the flat position can be analyzed by its Jacobian linearization evaluated at this point. Let A and B denote the state space and the control input matrices of the Jacobian linearization of (3.11), respectively. At the point $\theta = \omega = 0, V_{ap} = V_{an} = V_B, V_M = 0$

$$A = \begin{bmatrix} 0 & 1 & 0 & 0 \\ \frac{1}{J}(-k + C_0 V_B^2 \frac{2L^2}{3d^2}) & -\frac{b}{J} & \frac{C_0 L V_B}{2dJ} & -\frac{C_0 L V_B}{2dJ} \\ 0 & -\frac{LV_B}{2d(\rho+1)} & -\frac{1}{RC_0(\rho+1)} & 0 \\ 0 & \frac{LV_B}{2d(\rho+1)} & 0 & -\frac{1}{RC_0(\rho+1)} \end{bmatrix} \tag{5.16}$$

and

$$B = \begin{bmatrix} 0 & 0 & \frac{1}{RC_0(\rho+1)} & -\frac{1}{RC_0(\rho+1)} \end{bmatrix}^T. \tag{5.17}$$

A simple computation shows that the controllability matrix $[B \vdots AB \vdots A^2B \vdots A^3B]$ has

rank three, the third and fourth lines being linearly dependent. The fact of not being full rank comes with the differential configuration. Since V_{ap} and V_{an} are rigidly linked to the mirror, they can not vary independently, hence, one degree of controllability is lost. However, it will be shown later that the internal dynamics is, nevertheless, stable. The uncontrollable mode is associated to the voltage across the device, not to the angle.

It is easy to see that the bias voltage plays an essential role in enhancing the controllability. When setting V_B to zero, the rank of the controllability matrix at the flat position will fall down to one because the first two lines in the controllability matrix become zero, leaving only the two linearly dependent third and fourth lines. Maintaining the bias voltage V_B greater than zero will assure the linear controllability at the flat position.

5.2.3 Control Synthesis

The closed-loop control design is based on the technique of input-output linearization. The closed-loop control system diagram is shown in Fig. 5.7. Comparing Fig. 5.1 and Fig. 5.7 it is seen that the control system in both cases is similar. The major difference is the inclusion of the differential scheme and the analysis of the internal dynamics ψ. To construct the controller, successive time derivatives of the output are carried out, then a new system is constructed through a change of coordinates. That is, with the output $y = \theta$, the system (3.11) yields

$$\dot{y} = \dot{\theta} = \omega \tag{5.18a}$$

$$\ddot{y} = \dot{\omega} = \frac{1}{J}\left(-b\omega - k\theta + \frac{C_0}{2}\left(\gamma'_\theta V_{ap}^2 + \gamma'_{-\theta} V_{an}^2\right)\right) \tag{5.18b}$$

$$\dddot{y} = \frac{1}{J}\left[-b\ddot{\theta} - k\dot{\theta} + \frac{C_0}{2}\left(2\gamma'_\theta V_{ap}\dot{V}_{ap} + \gamma''_\theta \omega V_{ap}^2 + 2\gamma'_{-\theta} V_{an}\dot{V}_{an} + \gamma''_{-\theta}\omega V_{an}^2\right)\right]. \tag{5.18c}$$

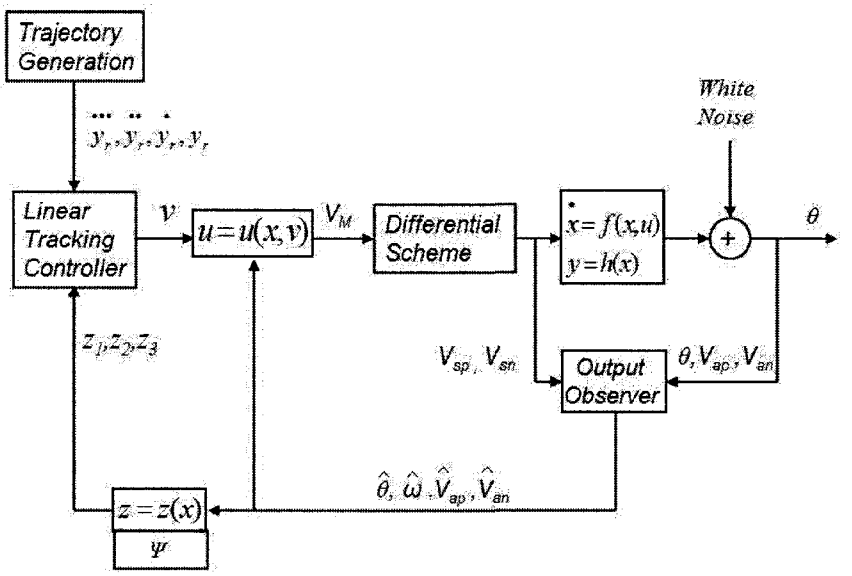

FIGURE 5.7 CLOSED-LOOP DIAGRAM FOR THE DUAL MIRROR.

Equation (5.18c) can be further developed by including the dynamic equations of $\dot{V}_{ap}$ and $\dot{V}_{an}$, (3.11c) and (3.11d) respectively. Then, it follows

$$\begin{aligned}\dddot{y} =& \frac{1}{J}\left[-b\ddot{\theta} - k\dot{\theta} + \frac{C_0}{2}\left(2\gamma'_\theta V_{ap}\left(\frac{V_B + V_M - V_{ap}}{RC_0} - \omega\gamma'_\theta V_{ap}\right) + \gamma''_\theta \omega V_{ap}^2\right.\right. \\ & \left.\left. +2\gamma'_{-\theta} V_{an}\left(\frac{V_B - V_M - V_{an}}{RC_0} - \omega\gamma'_{-\theta} V_{an}\right) + \gamma''_{-\theta}\omega V_{an}^2\right)\right]. \end{aligned} \tag{5.19}$$

Hence, the system has relative degree three in $D = \{(\theta, \omega, V_{ap}, V_{an}) \in \mathbb{R}^4 | V_{ap} \neq 0,\ V_{ap} \neq 0\}$. By using the following coordinate set

$$z = \begin{bmatrix} z_1 & z_2 & z_3 \end{bmatrix}^T \triangleq \begin{bmatrix} y & \dot{y} & \ddot{y} \end{bmatrix}^T, \tag{5.20}$$

the system can be transformed from $(\theta, \omega, V_{ap}, V_{an})$ into the normal form by means of the following (local) diffeomorphism

$$\phi(x) = \begin{bmatrix} z_1 & z_2 & z_3 & \psi \end{bmatrix}^T, \tag{5.21}$$

where ψ can be found by solving the partial differential equation $L_g\psi = 0$. It is noted that since the system has relative degree three, the existence of a zero-dynamics is implied. The design then addresses the control of the new three states $[z_1, z_2, z_3]$, which is valid as long as the internal dynamics is itself stable. This will be covered next in the stability analysis section. The linearized third order system is given then by

$$\begin{aligned} \dot{z_1} &= z_2 \\ \dot{z_2} &= z_3 \\ \dot{z_3} &= v, \end{aligned} \tag{5.22}$$

where v is the new control input. The linearizing control law for V_M can be deduced hence from Equation (5.19) as

$$\begin{aligned} V_M = \Bigg[& R\left(Jv + b\ddot{\theta} + k\dot{\theta}\right) - V_B\left(\frac{\gamma'_\theta}{C_1}V_{ap} + \frac{\gamma'_{-\theta}}{C_2}V_{an}\right) + \left(\frac{\gamma'_\theta}{C_1}V_{ap}^2 + \frac{\gamma'_{-\theta}}{C_2}V_{an}^2\right) \\ & + R\dot{\theta}C_0\left(\frac{{\gamma'_\theta}^2}{C_1}V_{ap}^2 + \frac{{\gamma'_{-\theta}}^2}{C_2}V_{an}^2\right) - \frac{R\dot{\theta}C_0}{2}\left(\gamma''_\theta V_{ap}^2 + \gamma''_{-\theta}V_{an}^2\right)\Bigg]\left(\frac{\gamma'_\theta}{C_1}V_{ap} - \frac{\gamma'_{-\theta}}{C_2}V_{an}\right)^{-1}, \end{aligned} \tag{5.23}$$

where $C_1 = \rho + \gamma_\theta$ and $C_2 = \rho + \gamma_{-\theta}$. It can be seen from (5.23) that the expression for V_M is not singular as long as $\left(\frac{\gamma'_\theta}{C_1}V_{ap} - \frac{\gamma'_{-\theta}}{C_2}V_{an}\right) \neq 0$. Since $\gamma'_{-\theta}$ is always negative, the expression is always positive if V_{ap} and V_{an} are both restricted to be greater than zero. This can be achieved by an appropriate choice of V_B. To this end, V_B should be sufficiently large to allow (5.15b) be always positive, and also sufficiently small to let

(5.15a) be below pull-in voltage. This reasoning, plus some simulations, suggest that V_B should be lower than the pull-in voltage but greater than half the pull-in voltage to allow the active control signal V_M maneuver comfortably. V_B can be safely chosen as two-thirds of the pull-in voltage, however, a theoretical study about the optimal choice of the value of V_B is beyond the scope of the present work.

In order to track a desired trajectory y_r, the same procedure used for the single-electrode electrostatic micromirror is employed. Suppose that y_r is sufficiently smooth, then the control signal v can be chosen as

$$v = \dddot{y}_r - k_2\left(\ddot{\theta} - \ddot{y}_r\right) - k_1\left(\dot{\theta} - \dot{y}_r\right) - k_0\left(\theta - y_r\right) \tag{5.24}$$

in such a way that k_0, k_1, and k_2 are all positive and $s^3 + k_2 s^2 + k_1 s + k_0$ is a Hurwitz stable polynomial of s.

5.2.4 Stability Analysis

The stability of the new system in the coordinates (z_1, z_2, z_3) cannot yet be inferred because the linearizing feedback control law given by (5.23) linearizes only the input-output map which is of third order. Therefore, it is necessary to examine the stability of the internal dynamics, which is of first order. To obtain the zero-dynamics, the output θ and its time derivatives $\dot{\theta}$, $\ddot{\theta}$, and $\dddot{\theta}$ are forced to be identically zero.

Subsequently, the condition $V_{ap} = V_{an}$ is easily obtained from (3.11b). Then taking into account that $z_3 = \ddot{\theta}$ from (5.20), it follows that $\dot{z}_3 = \dddot{\theta}$. Since $\dddot{\theta}$ is by definition forced to zero, it can be deduced from (5.22) that $v = 0$. Now, recalling from Chapter 3 that $\gamma'_{-\theta}(0) = -\gamma'_{\theta}(0)$, and noting that $C_1 = C_2$ when $\theta = 0$, the linearizing control

law V_M can be found from (5.23) to be

$$V_M = \frac{-\frac{V_B\gamma'_{-\theta}(0)}{C_1}(V_{ap} - V_{an}) + \frac{\gamma'_{-\theta}(0)}{C_1}(V_{ap}^2 - V_{an}^2)}{\frac{\gamma'_{-\theta}(0)}{C_1}(V_{ap} + V_{an})}.$$

Applying the condition $V_{ap} = V_{an}$, it yields $V_M = 0$.

Since the dynamical equations in (3.11) are symmetric in V_{ap} and V_{an}, either one can be worked on, say (3.11d). Hence, it can be deduced that the zero-dynamics is given by

$$\dot{V}_{an} = -\frac{1}{RC_0\,(\rho + 1)}\,(V_{an} - V_B)\,, \tag{5.25}$$

which is exponentially stable at the equilibrium point V_B. From Theorem 4.4 in Section 4.2.2, it follows that if y_r, $\dot{y}_r$, and $\ddot{y}_r$ are all uniformly bounded, then the feedback control composed of (5.23) and (5.24) provides (local) asymptotic tracking with internally bounded states.

5.2.5 Simulation

All simulations are made with Matlab/Simulink®. Quantizers and white noise matching experimental circumstances were taken into account and a fixed-step solver cycling at $5\mu s$ was used. This value is smaller than the one used for the single electrode micromirror ($40\mu s$) mainly because of the dynamics added by the differential scheme beyond pull-in. Again, the parameters of the micromirror used in simulation are given in Table 5.1.

The bias voltage V_B was set to $200V$ and the controller parameter Ω to 80000. This high value is due to the more complex dynamics resulting after the inclusion of a second electrode and the differential scheme.

Two control schemes, namely set-point and scanning control, are considered in simu-

lation. The scanning control reference trajectory is a sine wave:

$$y_r(t) = A \sin(2\pi t/T), \tag{5.26}$$

where A is the amplitude and T is the period.

Figure 5.8(a) shows the simulation result for a scanning trajectory of amplitude 2.5° and a $25ms$ period. It can be seen that the mirror followed smoothly the reference without distortion in nearly the whole deflection range allowed by the geometry, hence delivering the desired dynamic response. This confirms the main strength of the developed controller. Figure 5.8(b) shows the control signal V_M. It is seen that the range of the control signal V_M is considerably reduced compared to Figure 5.4. Clearly, the relationship between the input and the output is nonlinear. Again the control signal has to drastically compensate the pull-in phenomenon.

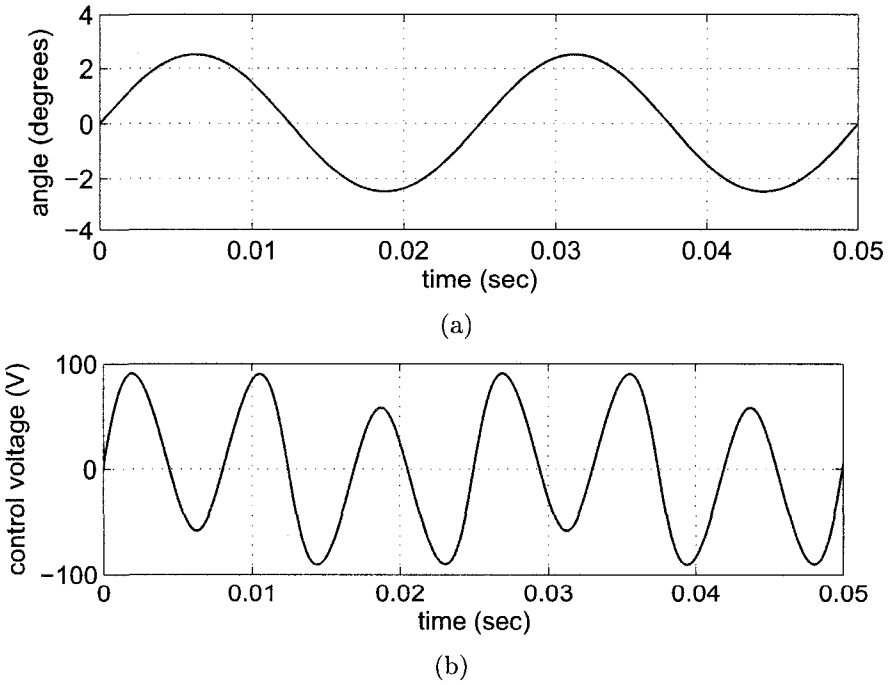

FIGURE 5.8 CLOSED-LOOP SCANNING CONTROL: (A) SYSTEM RESPONSE θ, (B) CONTROL SIGNAL V_M.

Figure 5.9 shows the tracking error for the scanning control. It is always less than $2mrad$ except for an initial transient when the controller is turned on. This small tracking error verifies the good performance of the controller.

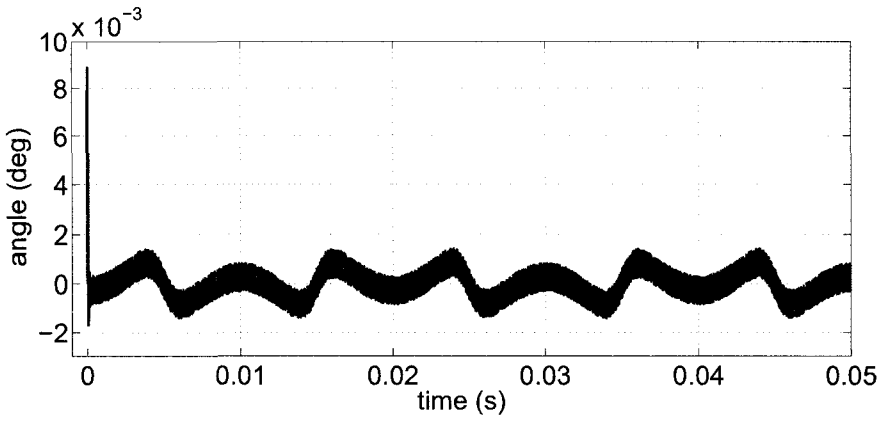

FIGURE 5.9 SIMULATION SCANNING ERROR.

The reference trajectory used in set-point control is of the same polynomial type used for the single-electrode micromirror. Figure 5.10(a) shows the simulation result for a set-point trajectory with a first set-point of $-2.5°$ and a second set-point of $2.5°$. The traveling time for each transition is set to $5ms$. It can be seen that the performance provided is excellent. Once again, the whole gap range operation is attained. Figure 5.10(b) shows the control signal V_M. It is clear that the input-output relationship is nonlinear, in particular during the second transition. It is noted that the system can go through the flat position with a bounded control signal without any problem of instability.

Figure 5.11 shows the tracking error for the scanning control. It is always less than $2.5mrad$ except for an initial transient when the controller is turned on. This small tracking error verifies the good performance of the controller. Finally, it is noted that the reduction in the control signal range facilitates the implementation of control systems with commercially available voltage amplifiers.

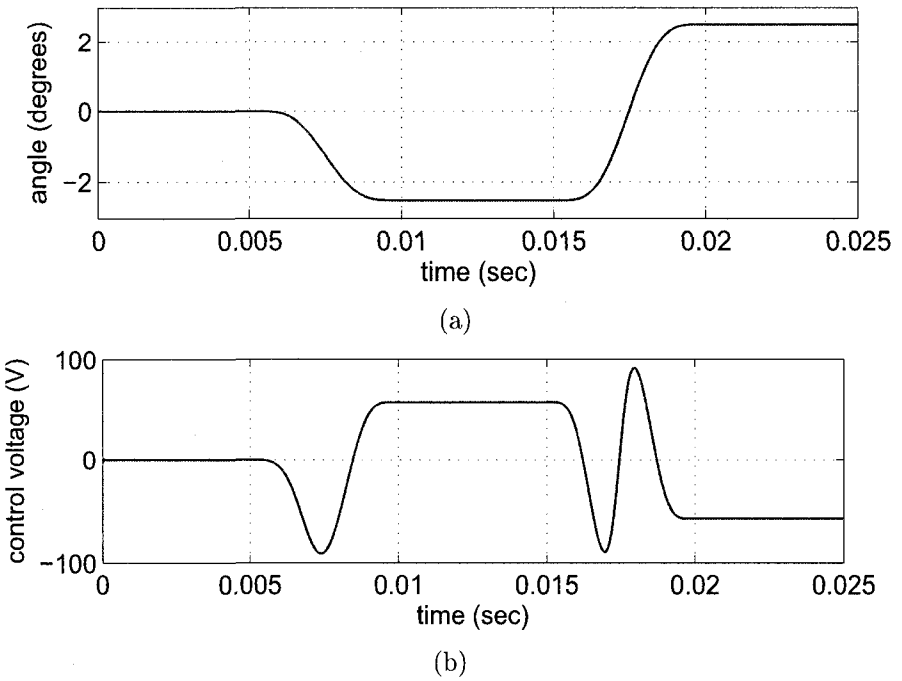

FIGURE 5.10 CLOSED-LOOP SET-POINT CONTROL: (A) SYSTEM RESPONSE θ, (B) CONTROL SIGNAL V_M.

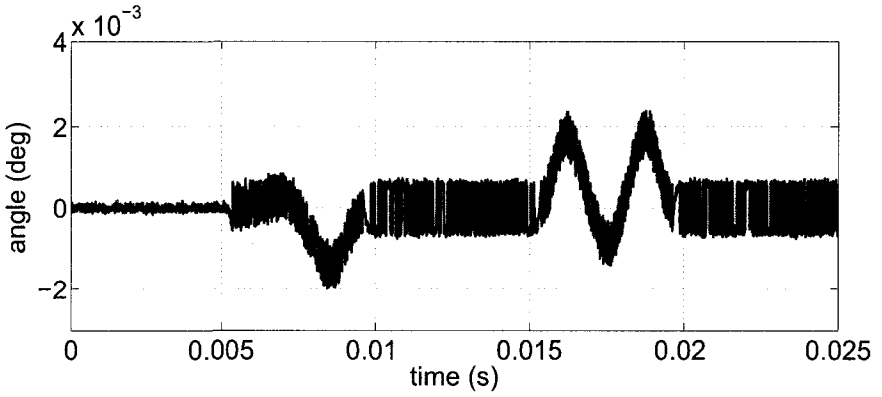

FIGURE 5.11 SIMULATION SET-POINT ERROR.

CHAPTER 6

EXPERIMENTAL IMPLEMENTATION

This chapter addresses the practical aspects of the implementation of the controllers developed in the preceding chapter. Initially a detailed description of the proposed setup is presented. Later, the characteristics of the two real micromirror used in this thesis are given. Open-loop responses and modeling issues are also discussed. Finally, experimental closed-loop results are reported.

6.1 Experimental Setup

6.1.1 General Description

A schematic representation of the setup is shown in Fig. 6.1, which consists of an xPCtarget-based control unit, a National Instruments 12bits DAQ (6025E), a high voltage amplifier (Apex PA97), two voltage boosters (EMCO G05) that provide the power supply for the high voltage (HV) amplifier, an infrared laser source (900nm wavelength), and a Hamamatsu position sensitive detector (PSD S1880). The electronic interfaces between the sensor, the actuator, and the DAQ board are custom-made circuits. The image of the embedded real-time application is developed in the Matlab/Simulink host PC, then it is downloaded to the xPC-Target kernel installed on the target PC. During experimentation, the host can control the execution of target programs and retrieve signal data. The laser is used to measure the micromirror angle. The actual setup in the lab is shown in Fig. 6.2.

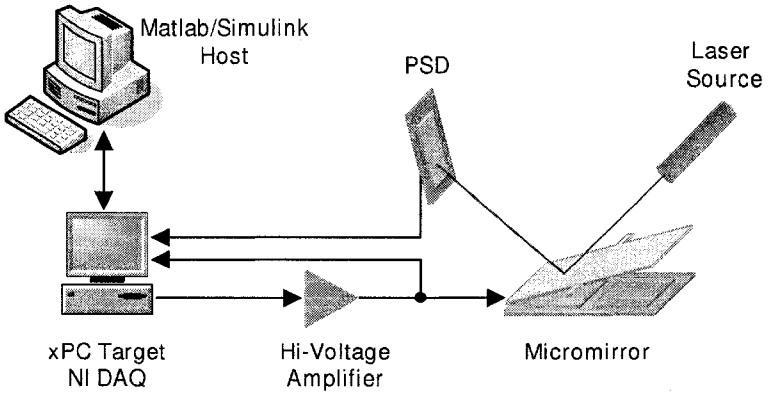

FIGURE 6.1 SCHEMATIC REPRESENTATION OF THE EXPERIMENTAL SETUP.

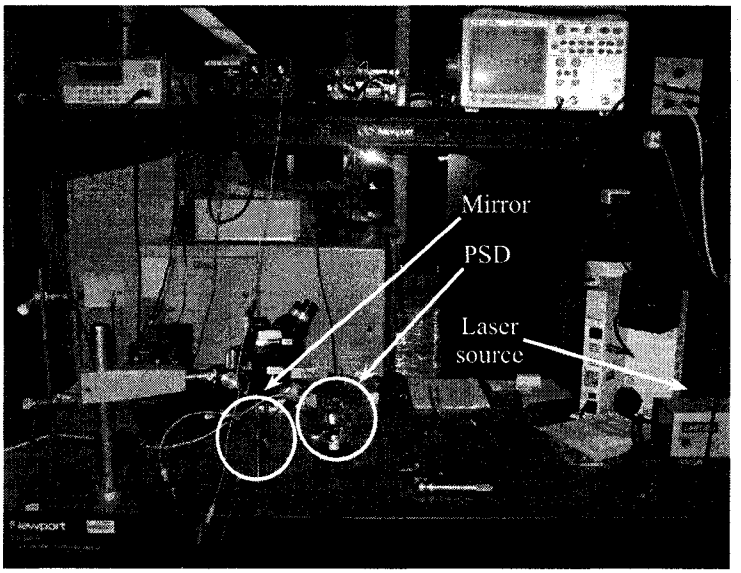

FIGURE 6.2 REAL SETUP IN THE LAB.

6.1.2 Actuation

One of the difficulties of working with electrostatic micromirrors is the high voltage required to generate a sufficient electrical torque. Consequently, the actuation system is mainly composed of a High Voltage (HV) amplifier. The drive system receives a small analog input voltage from the control unit, in the order of few volts, and delivers an amplified high voltage of several hundred volts.

Generally, commercial operational amplifiers do not operate with voltages above $30V$, that is why choosing such a device becomes a key issue. The HV amplifier used is the PA97 from Apex. The PA97 is a high voltage MOSFET operational amplifier designed as a low cost solution for driving continuous output currents up to 10mA and pulse currents up to 15mA into capacitive loads. External compensation provides flexibility in choosing bandwidth and slew rate for the application. The main properties of the PA97 amplifier are listed in Table 6.1. The value of the output resistance R is provided by the manufacturer and the output capacitance C_p is modeled by finding the *time constant* of a RC circuit that would deliver the time delay specified by the slew rate parameter provided by the manufacturer. The circuit used to implement the HV

TABLE 6.1 PARAMETERS OF THE PA97 AMPLIFIER.

Parameter	**Value**
Supply voltage	± 300 (V)
Input impedance, DC	10^{11} (Ω)
Gain bandwidth product	1 (Mhz)
Voltage swing	$\pm V_s \pm 20$ (V)
Output current	10 (mA)
Slew rate	8 (V/μs)
Amplifier output resistance R	100 (Ω)
Amplifier output capacitance C_p	2.0×10^{-7} (F)

amplifier with PA97 is shown in Fig. 6.3(a). The amplifier is used in noninverting configuration and is set to deliver a gain of $31V/V$. It must be noted that the

compensation capacitor C_c must be rated for the total supply voltage. A 20pF NPO (COG) capacitor rated at 500V was used. Of equal importance is to split the feedback resistor. A high voltage can appear across the feedback resistor, which might easily exceed the typical voltage rating for low wattage resistors (around 200V).

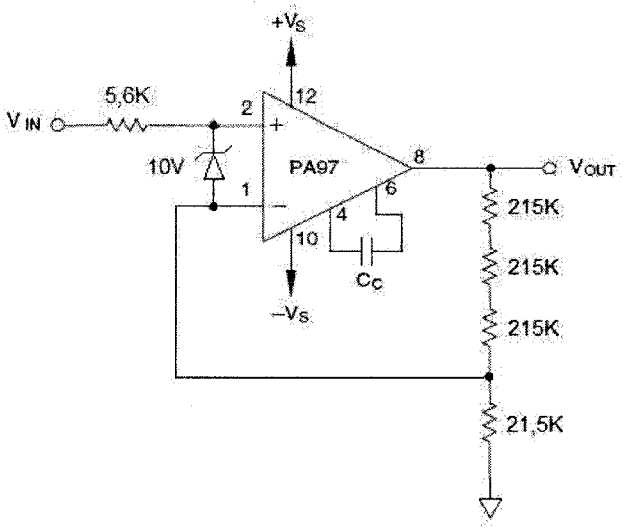

(a)

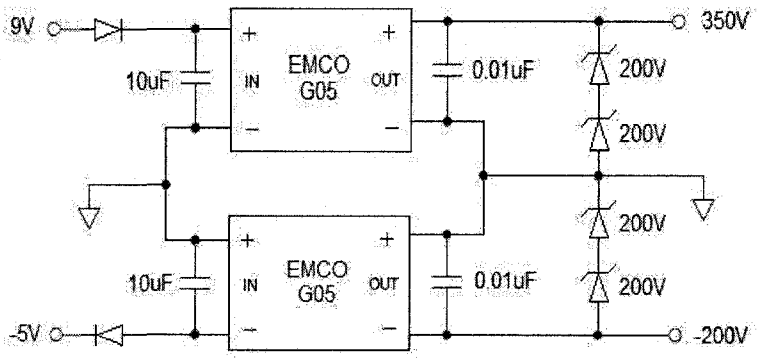

(b)

FIGURE 6.3 HV CIRCUIT: (A) HV AMPLIFIER CONFIGURATION, (B) HV POWER SUPPLY.

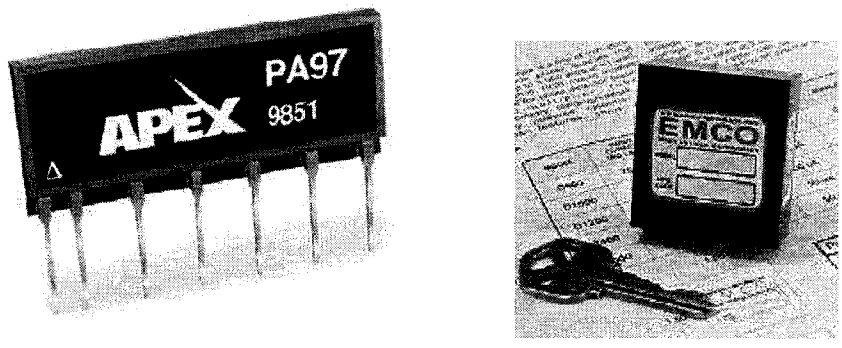

(a) (b)

FIGURE 6.4 ACTUAL DEVICES: (A) PA97 APEX AMPLIFIER, (B) G05 EMCO CONVERTER.

Another issue that comes with a HV amplifier is how to provide a proper power supply. To this end, another device has been accounted for, namely the G05 from EMCO. Both devices are shown in Fig. 6.4. The G05 is a miniature DC to HV converter. This component provides up to 500 VDC, positive or negative, in a compact PC mount package. The isolated output is directly proportional to the input (0-12V), and is linear from approximately 0.7 volts upward (turn-on voltage). It provides reliable DC to HV DC conversion with low ripple ($< 0.02\%$) and low EMI/RFI. Its maximum output current is $3mA$, and maximum input current is $250mA$. Two of these devices were used in conjunction to obtain positive and negative power supply as depicted in Fig. 6.3(b).

6.1.3 Applied Voltage Sensing

Thanks to the use of the applied voltage instead of the charge, the acquisition of this state variable is greatly simplified. In practice, a simple voltage divider is used to measure the applied voltage across the micromirror. Relatively big valued resistances were used to avoid consuming a significant current from the HV amplifier and to meet power consumption budget. The voltage divider provides linear sensing in such a way

that when a voltage of 410V is being applied, then a voltage of 10V is sent to the platform. The attenuation factor is 0.0244. The schematic of the voltage divider is shown in Fig. 6.5.

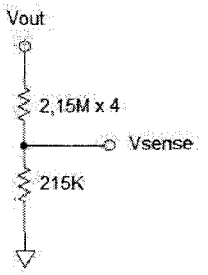

FIGURE 6.5 SENSING VOLTAGE DIVIDER.

6.1.4 Angular Position Sensing

Measuring the angle deviation is crucial for feedback operation. The method chosen for sensing the tilt angle consists in measuring the reflection of a beam light onto the mirror surface. This method is indirect and involves some calculation, but it is the option with lower associated costs and greater availability at the laboratory compared to the generic solution found in the market.

Fig. 6.6 shows how the tilt angle is derived. By means of a Position Sensitive Detector (PSD), the distance x is measured and consequently the tilt angle θ is deduced. From the diagram, it is seen that

$$\alpha_2 = \alpha_1 + \theta$$

$$\alpha_2 + \theta = \alpha_1 + \varphi$$

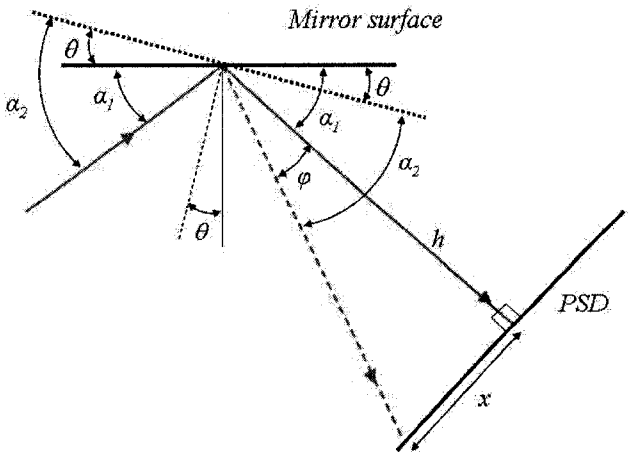

FIGURE 6.6 ANGLE SENSING DIAGRAM.

which yields

$$\varphi = 2\theta. \tag{6.1}$$

If the distance from the mirror spot to the PSD surface is denoted by h, the tilt angle θ is given by

$$\theta = \frac{1}{2} \arctan \frac{x}{h}. \tag{6.2}$$

The PSD used is the two-dimensional S1880 from Hamamatsu shown in Fig. 6.7. This device is an optoelectronic position sensor that utilizes photodiode surface resistance. Unlike discrete element detectors such as CCD, the PSD provides continuous position and beam intensity measurement with high resolution and fast response time. It features a relatively wide spectral response range and is robust with respect to the spotlight size since it measures its centroid.

The main properties of the PSD are listed in Table 6.2. Further information can be obtained from the manufacturer's web site.

Although the PSD sensor has the required performance for the proof-of-concept test,

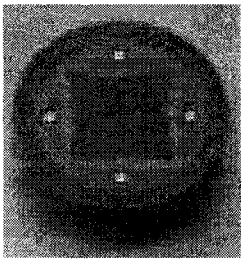

FIGURE 6.7 HAMAMATSU S1880 PSD.

TABLE 6.2 PARAMETERS OF THE PSD.

Parameter	**Value**
Active area size	12×12 (mm)
Maximum reverse voltage V_R	20 (V)
Operating temperature	-10 to +60 $(°C)$
Spectral response range	320 to 1060 (nm)
Peak sensitivity wavelength	920 (nm)
Maximum position detection error	$\pm$250 (μm)
Saturation current ($V_R = 5V$)	0.5 (mA)
Maximum dark current ($V_R = 5V$)	500 (nA)
Rise time	1.5 (μs)

final applications might require the use of integrated sensors. This continues to be an active research field, the treatment of which is out of the scope of this work.

In order to acquire the PSD signal, an interface circuit has to be built. Fig. 6.8 shows the diagram of the circuit used. Each axis has two current components. The values of the resistances R_1 to R_{25} are equal and were set to $5.6K\Omega$. R_f depends on the input level and was set to $21.5K\Omega$. Although the PSD is capable of providing two dimensional angular measurements, only one axis is used in the present systems. From Fig. 6.8 the outputs of the circuit are deduced as

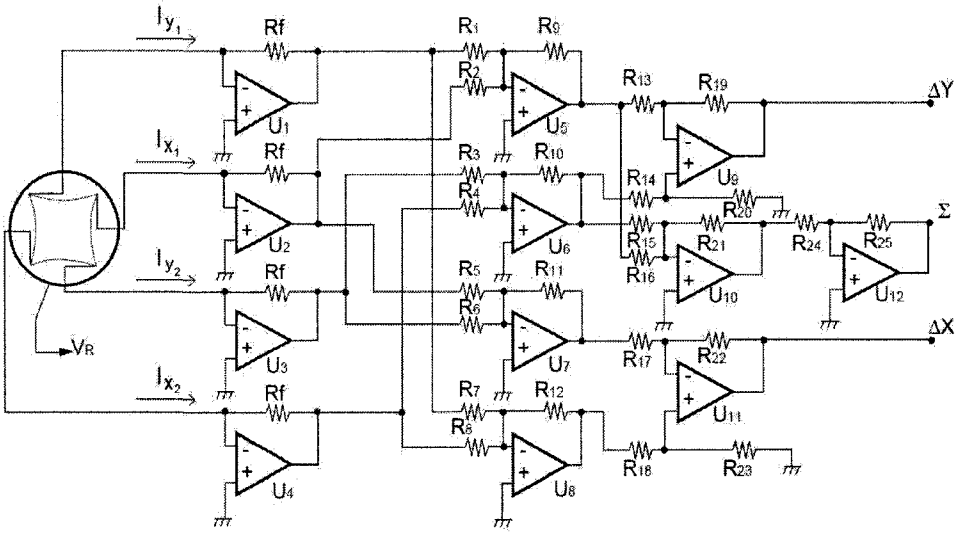

FIGURE 6.8 PSD INTERFACE CIRCUIT.

$$\begin{aligned}
\Sigma =& R_f \left(I_{y_1} + I_{y_2} + I_{x_1} + I_{x_2}\right) \\
Y =& R_f \left(I_{y_2} - I_{y_1} + I_{x_2} - I_{x_1}\right) \\
X =& R_f \left(I_{y_1} - I_{y_2} + I_{x_2} - I_{x_1}\right)
\end{aligned} \tag{6.3}$$

The signal actually used can be either Y or X, depending only on the axis aligned

with the micromirror. Both signals have ideally a gain of $1V/mm$, but it differs considerably depending on lighting conditions, beam intensity, and beam spot, which is why it has to be calibrated. The output Σ is a direct measurement of the incident light intensity.

6.1.5 Computation Platform

As seen in Fig. 6.1, the platform is composed of a host computer and a target computer. The host computer is used to design and create the models in MATLAB/Simulink, then the models are compiled and loaded on the target computer where they are executed in real time by the xPC target real-time operating system using a National Instruments (NI) Data Acquisition (DAQ) card as the I/O interface.

xPC Target is a real-time kernel that provides a high-performance, host-target prototyping environment that enables to link Simulink models to physical systems and executes them in real time on PC-compatible hardware. xPC Target enables to add I/O interface blocks to the simulink models, readily generating and downloading the code to a target PC running the xPC Target real-time kernel. The target PC can be a desktop computer, an industrial computer, PC/104, or any other PC-compatible device based on Intel or AMD 32-bit processors[1].

For this work, Simulink models are compiled using Visual C 6.0 compiler and then downloaded to the target PC via TCP/IP conection. Although the execution on the target PC can be controlled from MATLAB, most of the tests are made without direct interaction since the dynamics of the micromirrors is quite fast, hence, open and closed loop tests take just few milliseconds.

The main task to be done by xPC Target is to accurately update input and output

[1]http://www.mathworks.com

signals, to estimate state variables with the Output Observer, and to compute the control law. This is not a trivial task due to the high nonlinear terms in the model and the controller besides the time constraints imposed by the fast micromirror dynamics. The fastest successful sample time at which the control system executed was $25\mu s$. This is the sample time that was used for the closed-loop tests.

Nonetheless, some inconveniences were encountered with the utilization of this platform, mainly due to the timing requirements. Almost every test is interrupted by a time overflow caused by the operating system. This, of course, is not benign to a closed-loop control system. Furthermore, if this occurs during operation beyond pull-in then a failed test is certain to occur. Another problem is the serious overhead in every cycle computation. For a sample time of $40\mu s$, the task execution time (TET) is about $25\mu s$, but further reduction of the sample time would generate a time overflow.

The DAQ used in this work is the National Instruments NI6025E. This low cost acquisition card offers input-output analog capability and compatibility with the xPC Target system. Table 6.3 shows the main characteristics of this card. From Table 6.3

TABLE 6.3 PARAMETERS OF THE NI6025E DAQ CARD.

Parameter	**Value**
Number of AI	16 single ended or 8 differential
Type of A/D converter	Successive approximation
Input impedance	$100G\Omega$ in parallel with 100 pF
Input resolution	12 bits
Max sampling rate	200 kS/s
Max input voltage range	± 10 V
Number of Analog Outputs	2
Output resolution	12 bits
Max update rate	10 kHz, system dependant
Output voltage range	± 10 V
Max output impedance	0.1Ω

it can be seen that there is already one major drawback, which is the *Max update rate*. This characteristic states that the output signals can not be updated reliably faster than $100\mu s$. This is far from the needed sample time. After several tests, it can be concluded that below the time threshold of $100\mu s$ the performance of the DAQ card is seriously degraded.

Due to the stringent timing conditions, other platforms readily available are being considered. The purpose is to obtain more control of the low level execution of tasks to guarantee the required sample time and signals update.

The first option is an advanced microcontroller, the LPC2368 from NPX (PHILLIPS). This device is an ARM7-based microcontroller for general applications. These microcontrollers incorporate a wide sort of communication and control interfaces. It contains an ARM7TDMI-S processor, running at up to 72 MHz, and 512 kB on-chip Flash Program Memory with In-System Programming (ISP). The core is a fixed point RISC-based processor with a three-stage pipeline.

A basic interrupt driven program was developed to test this platform. A subroutine with the sole purpose of computing the capacitance function was timed to take about $100\mu s$. This is, of course, insufficient to fulfill the requirements of the nonlinear control at hand. This is why a faster, more powerful system with floating point capability is suggested. At present, a DSP-FPGA platform is now under preliminary performance tests.

6.1.6 Nonlinear velocity observer

The implementation of the control algorithm requires the availability of velocity measurement. Besides, the unavoidable presence of noise in real conditions needs to be handled. For the application addressed in this work the performance of the control

system can be considerably degraded if the noise level is high, particularly during operation beyond pull-in. This noise is mainly due to several sources such as electronic equipment, temperature dependance, electrical static, mechanical vibration, instruments imperfection, quantization, among others.

The nonlinear observer for state estimation we intend to use is of the general form

$$\dot{\widehat{x}} = f(\widehat{x}, t) + g(u) + K_{obs}[y(t) - H\widehat{x}], \qquad \widehat{x}(t_0) = \overline{x}_0. \tag{6.4}$$

The gain K_{obs} is chosen in order to guarantee the convergence of the state estimate $\widehat{x}$ to its true value x. One way to do so is to use the Extended Kalman Filter (EKF) approach and take

$$K_{obs} = PH^T R^{-1}$$

where H is the output matrix

$$H = \begin{bmatrix} 1 & 0 & 0 \\ 0 & 0 & 1 \end{bmatrix}.$$

corresponding to the measurement of θ and V_a, R is the covariance matrix of the output noise, and $P(t)$ is the solution of a differential matrix Ricatti equation (see e.g. [Bryson and Ho (1975)] for more details).

However, incorporating such a filtering scheme, in particular solving the Ricatti equation on-line, requires a much faster sample time (around $5\mu s$) than it is at disposal during this work (around $40\mu s$). Therefore, a constant gain K_{obs} is chosen, the value of which is obtained based on extensive simulations.

6.1.7 Experimental Issues

Throughout the realization of this work several setbacks were encountered that held back the experimental testing. Some of the most critical issues are described next.

Closed-loop execution takes considerable effort to carry out since the micromirrors at hand are relatively fast with respect to the sample time attained by the computing platform. A modest sample time of $25\mu s$ (minimum sample time attainable by the current setup) is simply on the edge of the Nyquist frequency. Furthermore, the rise time and the scape time showed by the current micromirror are not greater than $100\mu s$, which makes the sample time issue a great one.

Tests beyond pull-in were usually difficult to bring about because micromirrors are not usually mechanically protected. Even though a great effort was put in software and electrical protections, most of the tests near pull-in ended up by destroying some of the few micromirrors at hand.

Besides the hardware issues involved in the implementation of control systems, numerical issues have to be taken into account as well. Integration methods, integration step, numerical stability, numerical accuracy, bloc rearranging, function calculation, and signal consistency are just some of the aspects that have to be considered not only in design, but in implementation. Also, considerable effort was put into simplifying the expressions in the models. Every pre-computed multiplication can save execution time. As illustration, these simplifications helped to reduce the initial execution time by about half.

Despite the good performance of the nonlinear observer, small biases were spotted during tests. This could be explained by the fact that the observer assumes a perfect model, but the question arises if the approximation is good enough or if a different approach could offer better experimental results.

Finally, modeling is also a delicate matter. An accurate model is necessary in order to make the control system work properly. Great care should be given to make the model as precise as possible. This is particularly valid for the micromirrors available at the laboratory, since most of them deviate considerably from theoretical models. Various sources of inaccuracy in the model are:

- Geometry and driving mechanism for both electrodes are considered identical.
- The squeeze damping film effect has been neglected.
- Mirror displacement due to hinge translation has been neglected.
- The mirror surface is considered flat and rigid.
- The electrical interference between the electrodes is considered negligible.

6.2 Instruments Calibration and Components Tuning

Before any experimental test can be performed, there is a calibration and tuning procedure. Among the main bottlenecks in the setup are: sensor calibration, equipment performance and execution coordination. Special attention must be paid to these issues every time a new set of tests is to be carried out. Concisely, several items have to be addressed.

Mirror alignment. In order to acquire reliable angle measurements the micromirror has to be aligned with the PSD. From Fig 6.6 it can be seen that the beam that comes from the mirror and arrives to the PSD is expected to be perpendicular to the PSD surface. The tuning can take some considerable time depending on the positioning mechanism available in the lab. It is also important to assure that the mirror rotation axis is well positioned since in Fig 6.6 it is assumed to be perpendicular to the page surface. To help aligning the mirror it is useful to keep the laser source, the mirror

and the PSD at the same horizontal level and assure that as the mirror tilts the beam only produces readings on the PSD along one axis.

Distance. The distance between the mirror surface and the PSD surface has to be accounted for as well. This depends on the expected maximum tilt angle and needs some priory mirror knowledge. For this work, mechanical characteristics suggested a maximum tilt angle of 2.7° for the micromirror, which means that for single-electrode operation the total angle that the PSD should measure is 5.4°. Since it is desirable that most of the surface be used to attain the maximum available resolution, a conservative maximum distance for x in Fig 6.6 would be of 10mm. *Conservative* in this context means that the beam spot is not to be close to any edge of the PSD surface. Then, it follows

$$h = \frac{10mm}{\tan(5.4°)} \sim 105mm$$

This means that the PSD sensor can not be placed further than $10.5cm$ from the mirror. In fact, for bigger angles the PSD has to be even closer to the micromirror. Due to physical obstacles and mechanical alignment it is unpractical to have the PSD closer than 5cm, which is why the distance generally used throughout the tests was around $8cm$.

Beam spot size. The beam spot size is not as trivial as it could seem to be. It would be desirable to have a laser source with a very narrow beam, but in practice this is not always what is available in the laboratory. The beam, then, has to be passed through a lenses arrangement to focus it onto the mirror surface. No lenses arrangement was used after reflection to avoid a more complex angle computation. According to the PSD datasheet, the spot position can be sensed despite its size, but care should be taken not to flood the PSD surface since it could lead to unreliable readings.

Connections. It is helpful to make sure which mirror pins are to be used and to

establish electrical connection before mirror alignment since once the mirror is aligned any little movement can displace it. Also, some precautions should be taken when manipulating the HV circuits since high static electricity may be stored and can cause electrical discharges that can harm not only the devices but also a human being.

PSD signal. The analog signal that comes from the PSD depends highly on temperature and beam intensity. Because of this, voltage measurements have to be made with known distances in order to assure that the PSD voltage corresponds indeed to the displacement that is being measured. According to experimental tests, the PSD voltage stabilizes reliably after at least half an hour of operation.

Angle span. To obtain reliable angle measurements it is extremely important to correctly map the micromirror zero and maximum angle to the PSD readings. This is particularly critical for operation beyond pull-in, where angle imprecisions or offsets would lead to a failed test. In order to do so, a good practice is to run frequently calibration checks by applying a sufficiently high voltage to make the mirror go to its maximum angle for a brief lapse of time and recalibrate if necessary. This obviously implies a snap protection mechanism which would prevent the micromirror from breaking.

Angle resolution. Although the PSD sensor is supposed to give 1V/mm, this value is found to be inaccurate and to depend heavily on light conditions. An influential factor could be the fact that the interface card sold by Hamamatsu is not being used. Nevertheless, according to the manufacturer the PSD sensor gives around 12V for 10mm. Then, using the $\pm$10V range for the 12bit DAQ, the resolution becomes

$$x_{resolution} = \frac{20V}{(2^{12}-1)}\frac{10mm}{12V} = 4.1\mu m$$

Now, having the PSD distance resolution, the angle resolution can be calculated using the Equation (6.2) yielding $1,2mdeg$. Unfortunately, after exhausting tests, the noise

found in the angle measurement by the platform is about $\pm 10 mdeg$, a relatively high value. Of course, with better equipment this numbers should improve.

Applied voltage resolution. The high voltage applied to the micromirror is sensed through a voltage divider as shown in Fig. 6.5. Normally, the conversion factor $0.0244V/V$ is derived from the circuit, however, in practice this value differs due to the high voltage dynamics and electrical noise. This value then has to be calibrated as well. Using the 12bit DAQ range of 20V the resolution is given by

$$V_{a_{resolution}} = \frac{20V}{(2^{12}-1)} \frac{410V}{10V} = 0.2V$$

The noise level is found as well to be high: $\pm 2V$.

6.3 Characteristics of the Micromirrors

6.3.1 Single Electrostatic Micromirror

The top view of the single electrostatic micromirror is shown in Fig. 6.9. The geometric and the mechanical parameters of the single micromirror are given in Table 6.4. Every static parameter listed was measured straightforwardly, however, the dynamic parameters k, ω_n, ζ, θ_{PIN}, and V_{PIN} required a more elaborate procedure.

In order to obtain the value of the stiffness coefficient k, the real pull-in voltage V_{PIN} was drawn from laboratory tests, then the value of k was found from (3.16). It is noted that the value of k must be particularly accurate since the pull-in voltage is very sensitive to this parameter. The pull-in angle θ_{PIN} for the single electrostatic micromirror can be computed from equation (3.15) using the capacitance model (3.3), resulting in $\theta_{PIN} = 1.01°$. It is noted that this result agrees almost perfectly with the experimental result shown in Table 6.4.

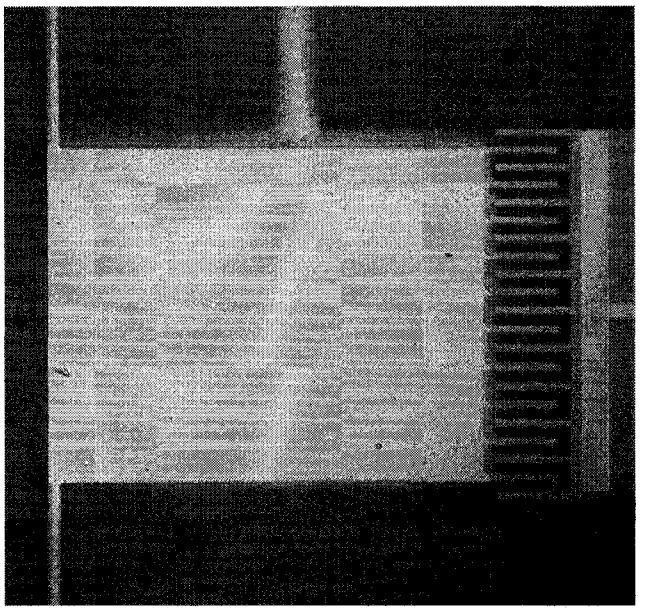

FIGURE 6.9 TOP VIEW OF THE SINGLE ELECTRODE MICROMIRROR.

TABLE 6.4 PARAMETERS OF SINGLE-ELECTRODE MICROMIRROR.

Parameter	**Value**
Mirror width W	250 (μm)
Mirror length L	300 (μm)
Mirror comb length	350 (μm)
Air gap d	12 (μm)
Damping ratio ζ	0.1
Natural frequency ω_n	60000 (rad/s)
Stiffness coefficient k	2.3 10^{-7} (N/rad)
Maximum angle $\theta_{\max}$	$\sim 2.3°$
Touch angle θ_{TOUCH}	$\sim 1.96°$
Pull in angle θ_{PIN}	$\sim 1.01°$
Pull in voltage V_{PIN}	$\sim 73V$
Permittivity ε	8.85×10^{-12} (F/m)

From Equation (3.4) it can be considered that for small angle deflections the system behaves like a second order dynamical system. For this reason, the damping ratio ζ and the undamped natural frequency ω_n parameters preferred over the J and b since they can be determined in a straightforward manner from open-loop angle response. Since k is already known, then the parameters J and b can be indirectly obtained using the well known expressions $J = k/\omega_n^2$, and $b = 2J\zeta\omega_n$.

According to Equation (3.8), every parameter of the single micromirror model has then been identified. The remaining parameters R, and C_p are given in section 6.1.2 where the actuation system was described, and the parameter C_0 and the function γ are entirely defined by the mechanical dimensions of the mirror.

6.3.2 Dual Electrostatic Micromirror

The geometric and mechanical parameters of the dual electrostatic micromirror are given in Table 6.5. Fig. 6.10 shows the top view of the dual-electrode micromirror.

TABLE 6.5 PARAMETERS OF DUAL-ELECTRODE MICROMIRROR.

Parameter	**Value**
Mirror width W	500 (μm)
Mirror length L	250 (μm)
Air gap d	12 (μm)
Torsion beam width, w	20 (μm)
Torsion beam length, l	200 (μm)
Mirror and torsion beam thickness, δ	10 (μm)
Damping ratio ζ	0.15
Natural frequency ω_n	150000 (rad/s)
Stiffness coefficient k	3.9 10^{-6} (N/rad)
Maximum angle range $\theta_{\max}$	$\sim 2.7°$
Pull in angle θ_{PIN}	$\sim 1.20°$
Pull in voltage V_{PIN}	$\sim 280V$
Modulus of rigidity, G	73 (GPa)
Permittivity ε	8.85×10^{-12} (F/m)

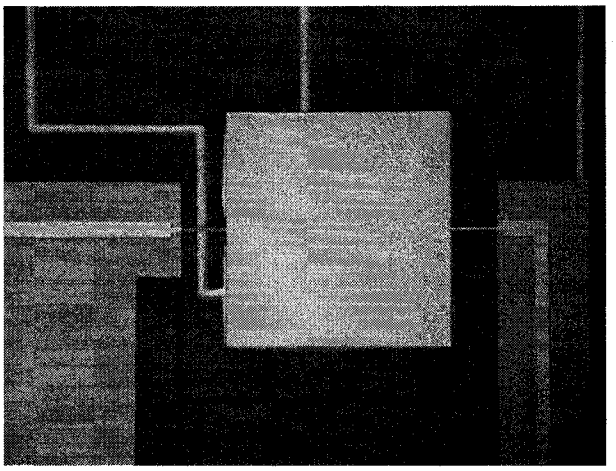

FIGURE 6.10 TOP VIEW OF THE DUAL-ELECTRODE MICROMIRROR.

Generally, several micromirrors come in one single chip depending on the design purposes. A typical MOEMS chip available at the Mechanical Department at Concordia University, where the experimentation took place, is shown in Fig. 6.11. The mirrors available on this chip have different torsion beam widths w and different kind of hinges (e.g. corrugated, beam) which lead to different pull-in voltages and in some cases to considerably different behaviours.

FIGURE 6.11 MOEMS CHIP.

Theoretically, the parameter k for beam hinges can be computed by using the follow-

ing expression [Gere and Timoshenko (1997)]

$$k = \frac{2Gw\delta^3}{3l}\left(1 - \frac{192\delta}{\pi^5 w} tanh\left(\frac{\pi w}{2\delta}\right)\right), \tag{6.5}$$

which for the dual-electrode micromirror would yield $k = 3.3410^{-6}$N/rad. Fig. 6.12 shows an additional schematic for the parameters involved in the computation of k. However, due to the lack of model precision, the procedure used to obtain this value

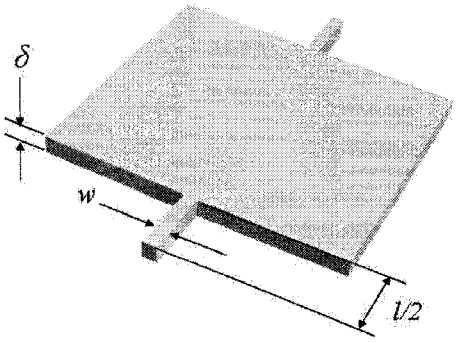

FIGURE 6.12 k PARAMETERS.

was the same as for the single micromirror. That is, the real pull-in voltage was drawn from laboratory tests, then the value of k is found from (3.16). It is noted that the value of the stiffness coefficient k calculated with Equation (6.5) and the one in Table 6.5 are relatively close, differing only by 16%, but the experimental approach was preferred since it led to a better model fitting.

Again, the pull-in angle for the dual electrostatic micromirror is computed from equation (3.15) using the capacitance model (3.3), resulting in $\theta_{PIN} = 1.21°$. This result agrees almost perfectly with the experimental result shown in Table 6.5.

6.3.3 Open Loop Responses

The open loop curves responses shown in this section were done with the single electrostatic micromirror previously described. Although its maximum angle is around 2.3°, the mirror has a comb extension that makes the mirror length equal to 350μ, stopping the mirror effectively at 1.96°. Open loop responses throughout all the micromirror range would be impossible without this physical protection since any test beyond pull-in would generally end up destroying the mirror. This solution offers test repeatability and its inclusion should not be taken carelessly in the design of MEMS. Furthermore, since there exists a touch angle θ_{TOUCH} the mirror angle will never reach the essential discontinuity at $\theta_{\max}$, improving numerical stability.

Fig. 6.13 shows the mirror output angle to a pseudo-step input measured with a 100Mhz oscilloscope. The term "pseudo" is used because the input signal is not a properly step input since it does not change instantaneously. Moreover, the rate of the applied voltage is limited by the slew rate specification of the HV amplifier. Each curve in each graph is matched by the same color. In Fig. 6.13(a) it can be seen from the transient that the damped natural frequency at the flat position is $\omega_d = 1/120\mu s = 8.4Khz$. This damping frequency decreases as the voltage increases until pull-in is reached. It is noted that as the voltage increases beyond pull-in, the lapse of time between pull-in and mirror stopping (escape time) decreases. This shows how sensitive the pull-in voltage is.

In Fig. 6.14 the nonlinearity of the micromirror becomes even more evident with a triangle voltage signal as input. Slightly different maximum voltages were introduced in the input signal to show the different responses of the tilt angle. The curves were obtained by using the platform xPCtarget since such input signals are more elaborate than those usually found in standard voltage generators.

Fig. 6.14 also shows one of the most common problems with MEMS: the stiction. In

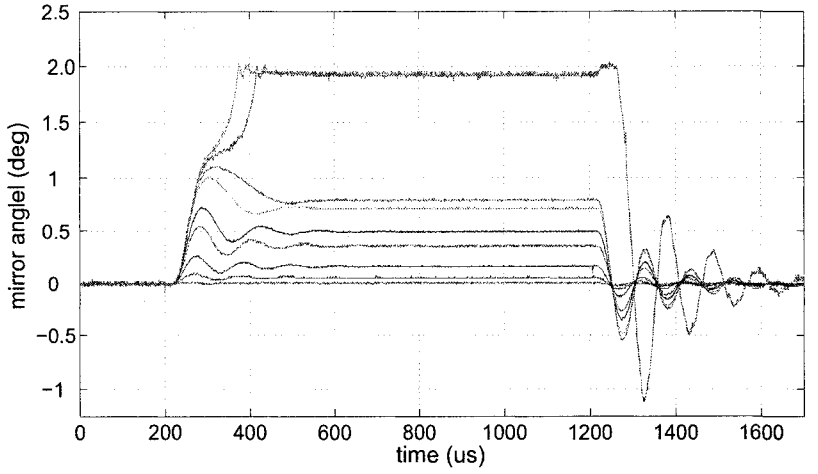

(a)

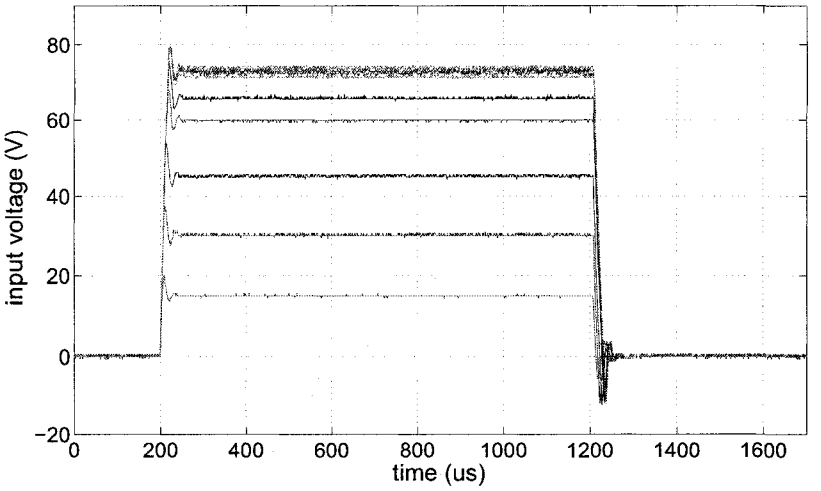

(b)

FIGURE 6.13 MIRROR RESPONSE TO A PSEUDO-STEP INPUT: (A) OUTPUT ANGLE, (B) INPUT VOLTAGE.

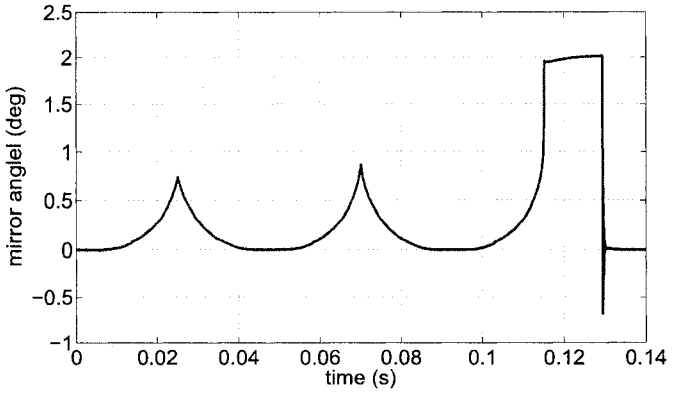

(a)

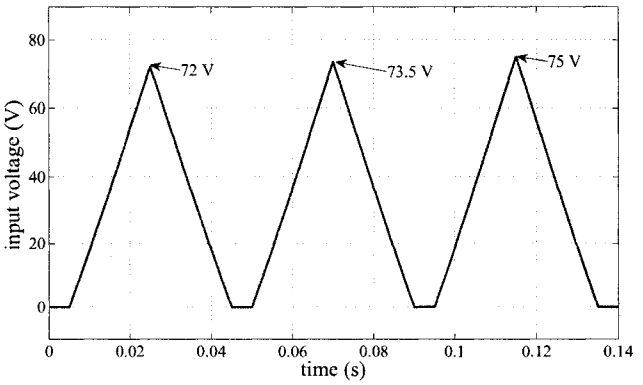

(b)

FIGURE 6.14 MIRROR RESPONSE TO A TRIANGLE INPUT: (A) OUTPUT ANGLE, (B) INPUT VOLTAGE.

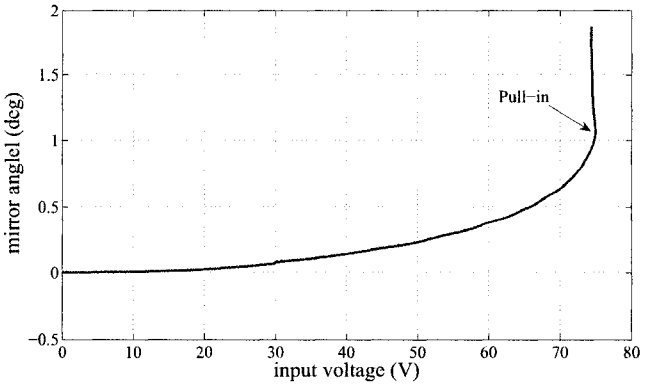

FIGURE 6.15 ANGLE VS VOLTAGE MICROMIRROR CURVE.

the third triangle the voltage is high enough to make the micromirror snap. Only after the applied voltage has gone back to practically zero did the micromirror restore itself. Of course, this is an undesirable behaviour for the micromirror. Besides the stiction phenomena, the micromirror generally does not restore itself in the same way it was actuated. Finally, Fig. 6.15 shows the characteristic angle vs voltage for the single electrostatic micromirror.

6.3.4 Model Fitting

How the model represents the actual device is crucial to the performance of a control system. If the model does not reflect the real dynamics of the device then the controller's performance will be degraded. This issue is even more delicate for the control system at hand because of the high nonlinearities present in the electrostatic micromirror and the limited resources of the platform used, which are already being pushed to their limit.

Fig. 6.16 shows how the output of the model developed for the single electrostatic micromirror corresponds to the real angle response of the micromirror in response of a pseudo step. The match is very close either below or beyond pull-in, keeping the model valid for the whole range of the micromirror. It is noted that this decent correspondence is achieved with the help of the Output Observer.

Fig. 6.17 shows the rest of the state variables generated by the model to the same input that generated Fig. 6.16(a). Since the angular velocity is not available the Output Observer is used for providing its estimate. The controller then, can be fed with the complete state vector reliably.

Although many model fitting techniques could be applied to obtain a different or better match, the advantage of the approach taken in this work is that the parameters

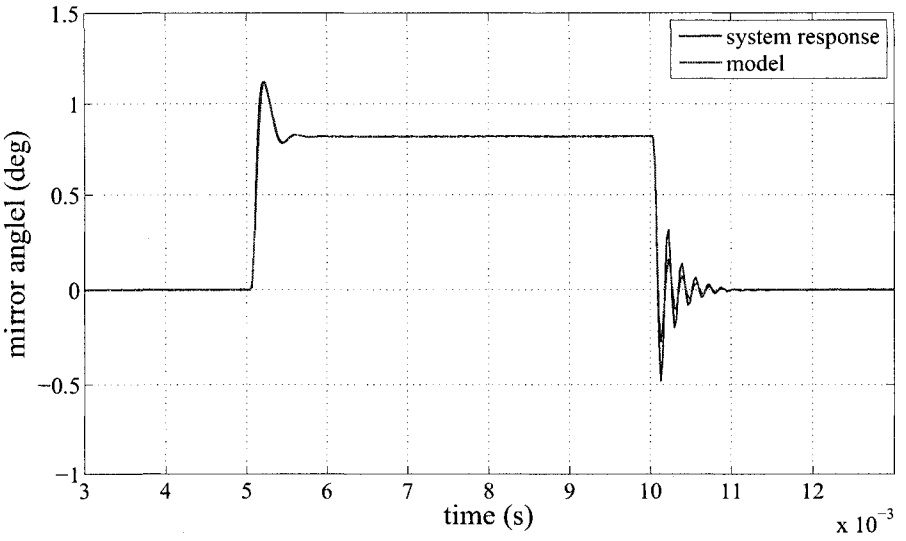

(a)

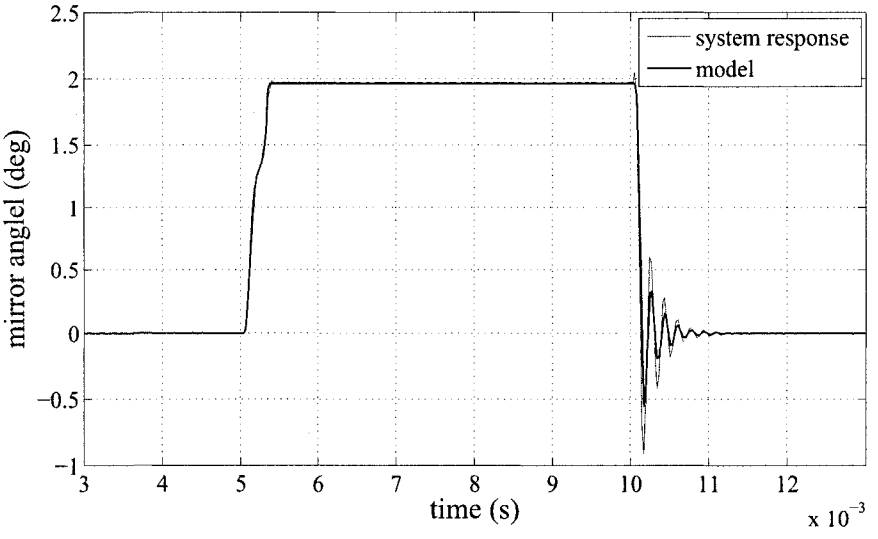

(b)

FIGURE 6.16 ANGLE FITTING : (A) BELOW PULL-IN, (B) BEYOND PULL-IN.

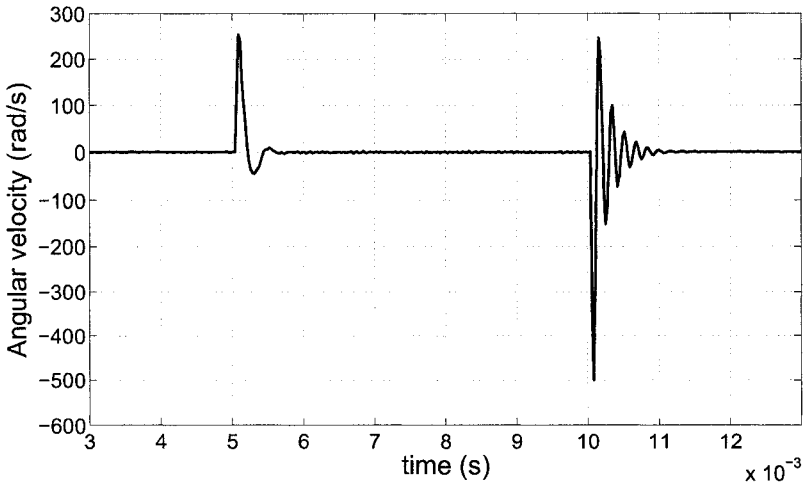

(a)

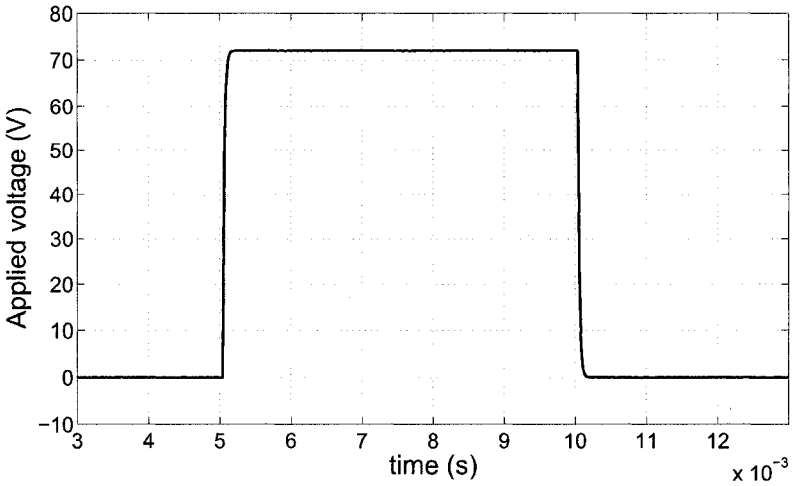

(b)

FIGURE 6.17 VELOCITY AND VOLTAGE FITTING : (A) BELOW PULL-IN, (B) BEYOND PULL-IN.

of the model can be directly inferred from the mechanical and dynamic properties of the device (Table 6.4).

6.4 Experimental Closed-loop Tests

Two different micromirrors were used to test the proposed controllers, namely a single-electrode micromirror and a dual electrode micromirror. Both single and dual actuation schemes were implemented for the dual-electrode micromirror.

6.4.1 Single-electrode Micromirror

The results for the single-electrode electrostatic mirror will be presented in two sets, first, operation below pull-in, then operation beyond pull-in. These are based on the controller parameter values obtained in Section 5.1.2 and the observer gain value given by

$$K_{obs} = \begin{bmatrix} 3266.9 & -0.004852 \\ 1.0714 \times 10^{8} & -159.12 \\ -0.9704 & 1.4412 \times 10^{-6} \end{bmatrix}.$$

Fig 6.18 shows experimental results for different set-points with transitions of $10ms$. It can be seen that the flatness-based controller makes the mirror follow the reference trajectory, hence delivering a desired dynamic response. This confirms the main strength of the designed tracking controller.

Despite the general satisfactory performance, a small steady-state error is noticed in Fig 6.24(a) due mainly to the discrepancy between the model and the real micromirror. An integrator in the direct trajectory could be accounted for in a future work, but up to the current stage of this thesis, the inclusion of such integrator would require a further decrease of the sample time, which is beyond the current limits of the

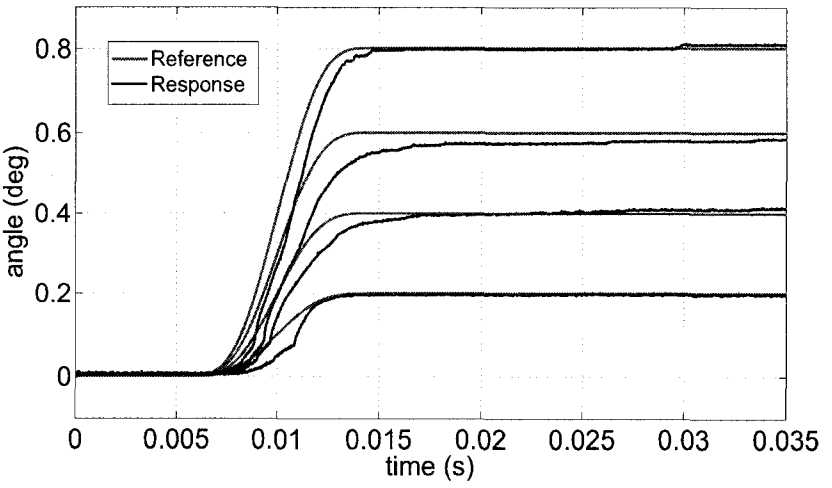

(a)

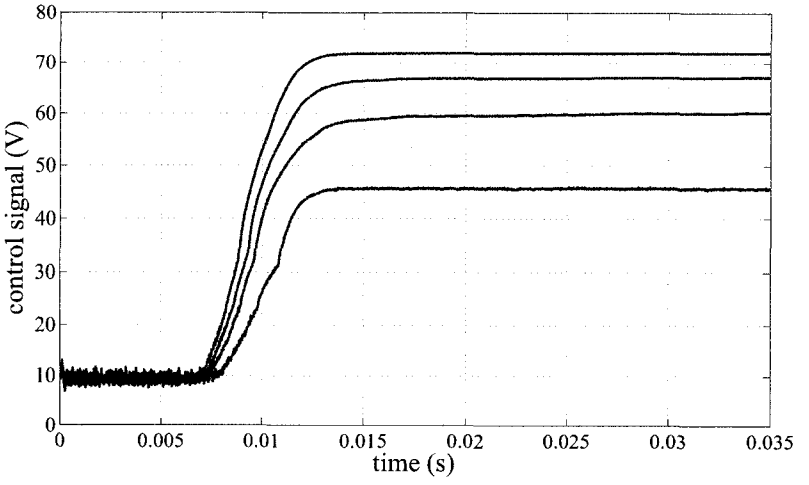

(b)

FIGURE 6.18 CLOSED-LOOP SET-POINT CONTROL BELOW PULL-IN: (A) SYSTEM RESPONSES, (B) CONTROL SIGNALS.

available platform. Moreover, the steady-state error of each test may vary slightly depending on random noise.

Another aspect noticed is the rather noisy system response. A great effort has been dedicated to decrease such noise as much as possible, but it an inevitable burden that real systems have to bear. Still, it can be improved for operation below pull-in by using additional frequency filters besides the Output Observer. The delay added by such filters does not affect the stability of the system below pull-in but they are prohibited for operation beyond pull-in.

Figure 6.24(b) shows the corresponding control signals for the set-point trajectories. Although quite smooth, it is seen that the control signal shows some variations at low voltages, i.e., near the uncontrollable point. To avoid the singularity at the zero-voltage position, a small bias voltage of $10V$ is applied. This produces an initial angle of less than $0.01°$. Since the actuation voltage curve is highly nonlinear, the deflection of the device due to the bias voltage is nearly unnoticeable at low voltages. This is illustrated in Fig. 6.19 where a zoom is made on the time range when the controller is turned on. Fig. 6.19 also illustrates the effective filtering along the angular trajectory, which shows the effective performance of the Output Observer.

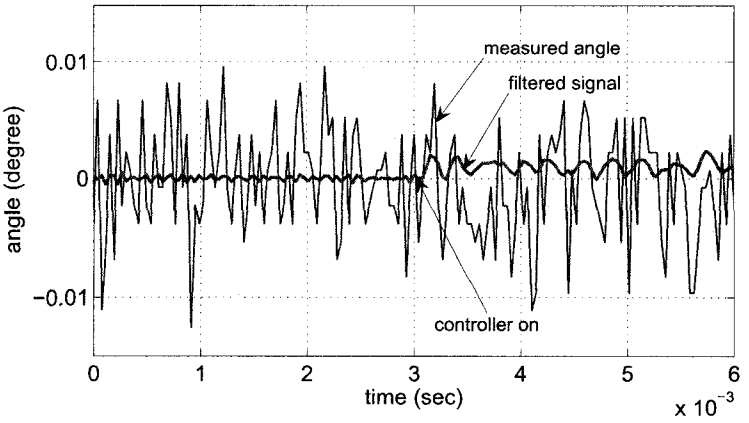

FIGURE 6.19 ZOOM ON SYSTEM RESPONSE: MEASURED ANGLE AND FILTERED SIGNAL.

How much the parameters can vary without affecting the overall performance of the control system is difficult to determine since even decreasing the sample time by $5\mu s$ can improve noticeably the robustness. For the current state of this work, a variation greater than 10% on any parameter can compromise the control system performance, although the percentage could increase greatly for operation below pull-in. Furthermore, a considerable noise on the angle state variable or the applied voltage state variable can destabilize the whole system. However, faster sample times anticipate increased robustness.

Operation beyond pull-in is shown in Fig 6.20. To illustrate the behaviour of the control system below and beyond the pull-in point, two references are presented: 0.8° and 1.25°. Let us recall that the pull-in angle is approximately 1.0°. First, it is noted that operation beyond pull-in is possible thanks to the closed-loop nonlinear controller. Still, it can be seen that operation beyond pull-in is noisier than operation below pull-in, causing some undesired random glitches. In deed, a much greater effort has to be done to keep the micromirror stable after pull-in. The system then becomes more sensible to noise and perturbations as the capacitance function has larger variations for any variation of theta. At the same time, every discrepancy between the model and the real device is strengthened beyond pull-in, demanding more from the controller. Furthermore, stabilization beyond pull-in for the electrostatic mirror at hand does not occur for sample times slower than $28\mu s$.

Fig 6.20(b) shows the control signals generated for the two references. It is seen how the controller goes beyond the pull-in voltage to make the mirror cross to the unstable zone and then lowers the voltage accordingly. This is not seen for references below pull-in since the mirror works in a stable zone. Some impulse disturbances are also observed in Fig 6.20. These are caused, among other things, by the real-time operating system which fails to update the control signal at the exact time. However, the control system manages to restore the micromirror effectively. Another curve is

shown in Fig 6.21. Here, a reference of 1.45° was used. It is demonstrated hence that operation beyond pull-in is achieved successfully.

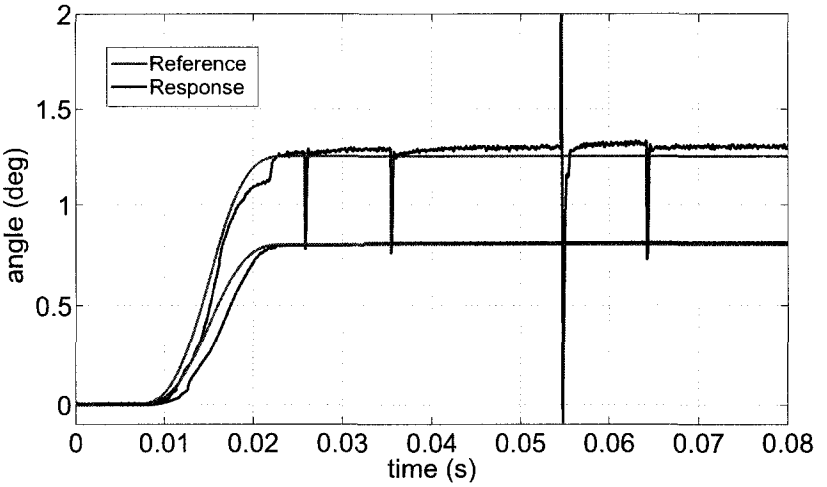

(a)

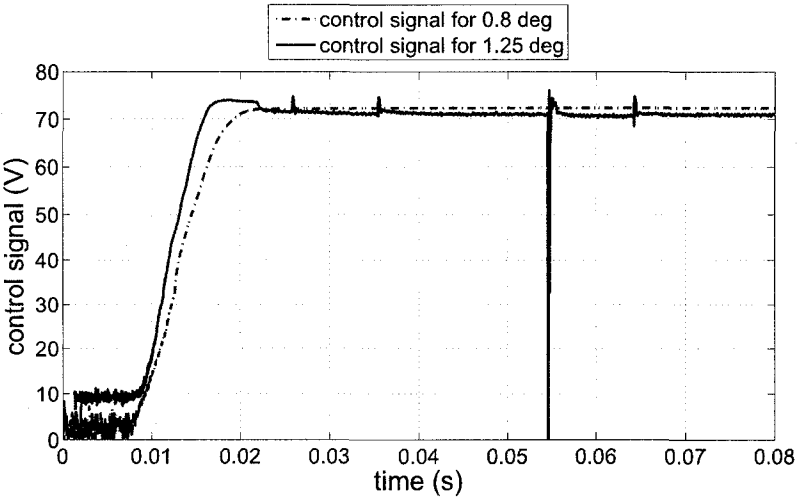

(b)

FIGURE 6.20 CLOSED-LOOP SET-POINT CONTROL BEYOND PULL-IN: (A) SYSTEM RESPONSES, (B) CONTROL SIGNALS.

Fig 6.21(b) also shows the control signal used for a smaller reference. Through this comparison, the nonlinear behavior of the electrostatic micromirror is better seen. Initially, the control signal is raised properly until pull-in, then the voltage is lowered accordingly. For higher angles, lower voltages are needed.

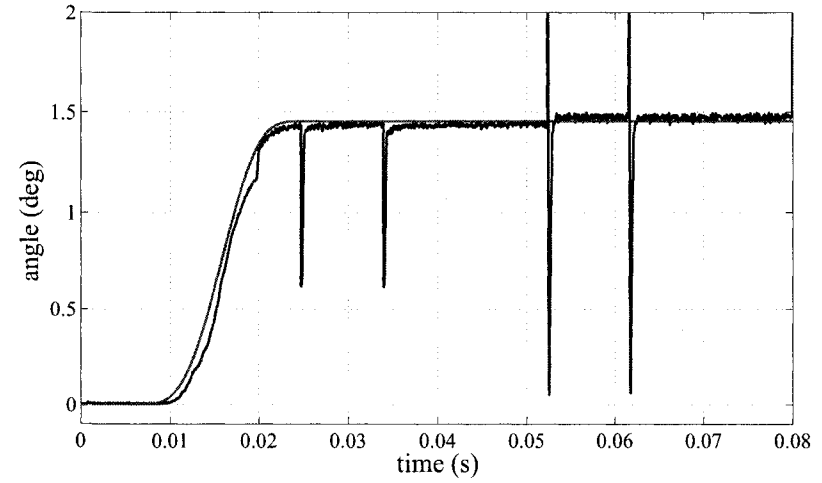

(a)

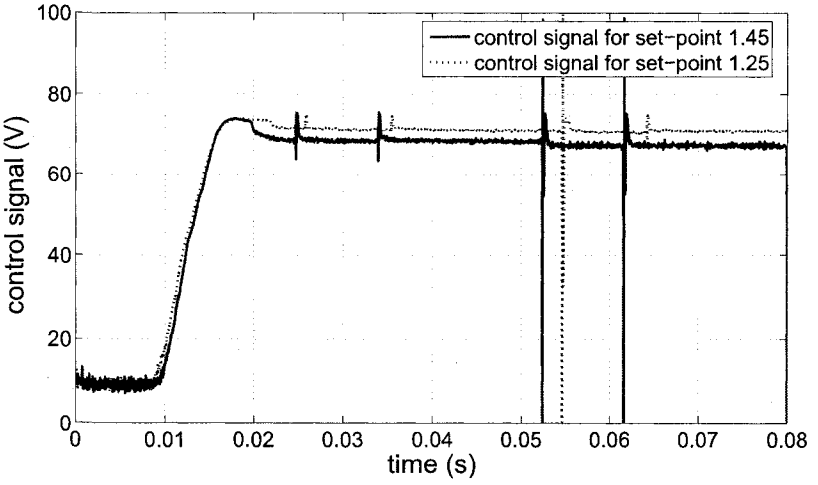

(b)

FIGURE 6.21 CLOSED-LOOP HIGHER SET-POINT CONTROL BEYOND PULL-IN: (A) SYSTEM RESPONSE, (B) CONTROL SIGNAL.

Fig 6.22 shows a scanning trajectory that goes beyond and below pull-in alternatively with a period of $50ms$. Once again the tracking controller exhibits a good performance managing the highly nonlinear control signals needed to achieve such reference. Another alternating set-point reference beyond pull-in is shown in Fig 6.23. As expected, it is easier for the controller to take the mirror out of the unstable zone than into it. Still, the reference is tracked, confirming the versatility of the designed controller.

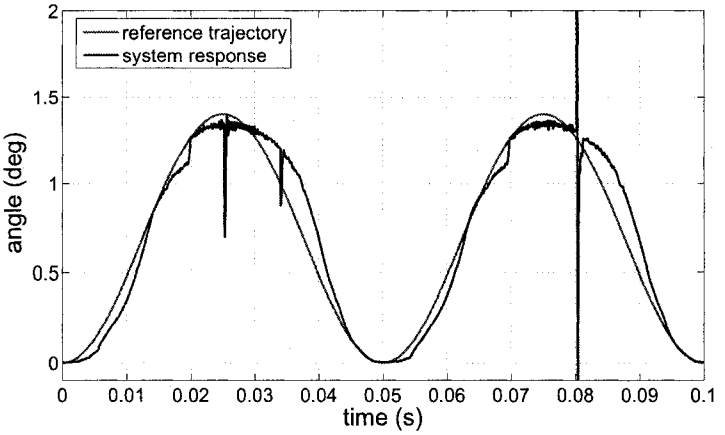

(a)

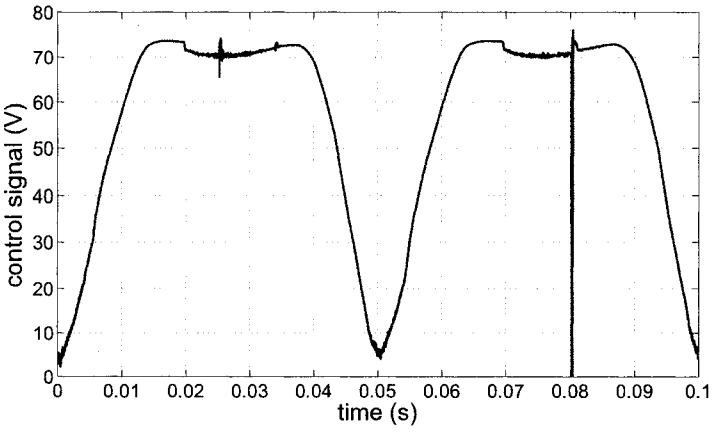

(b)

FIGURE 6.22 CLOSED-LOOP SCANNING CONTROL BEYOND PULL-IN: (A) SYSTEM RESPONSES, (B) CONTROL SIGNALS.

Finally, the maximum reference angle attainable by the current setup is about 1.6°. For references greater than 1.5° the steady-state error increases considerably, and at

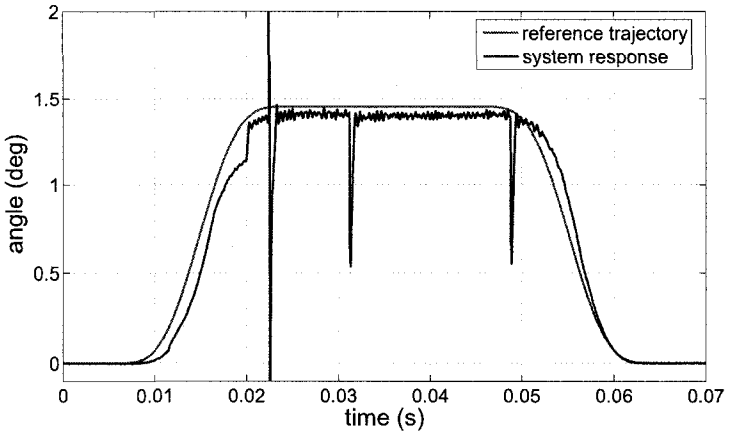

(a)

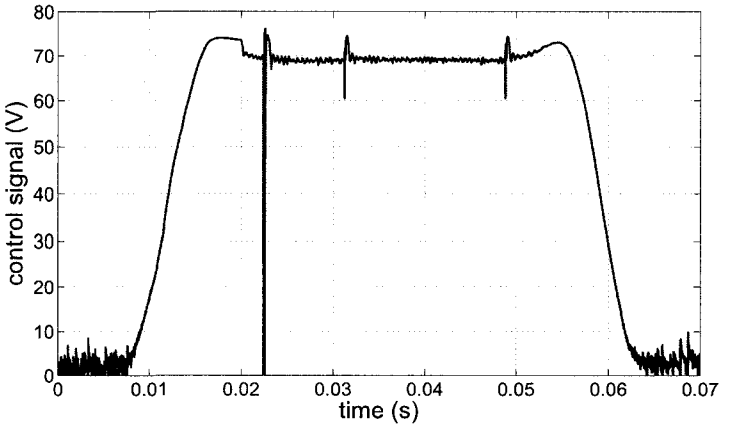

(b)

FIGURE 6.23 CLOSED-LOOP ALTERNATING SET-POINT CONTROL BEYOND PULL-IN: (A) SYSTEM RESPONSES, (B) CONTROL SIGNALS.

1.6° the system response becomes oscillating. This limitation is mainly because of the current setup capabilities, so further improvements are still foreseen.

6.4.2 Dual-electrode micromirror

6.4.2.1 Single Actuation Scheme

Fig 6.24 shows experimental results for different set-points below pull-in for the dual-electrode micromirror using a single actuation scheme. It can be seen that the flatness-based controller makes the mirror follow smoothly the reference trajectory, hence delivering the desired dynamic response. It is noted that the noise level and the model correspondence of the dual micromirror are considerably better than the single micromirror.

6.4.2.2 Dual Actuation Scheme

Figure 6.25(a) shows experimental results for a scanning trajectory of amplitude 0.5° and 50ms period. A bias voltage V_B of $200V$ was used. It can be seen that the mirror followed smoothly the reference without distortion, delivering the desired dynamic response. This confirms the main strength of the tracking controller. Figure 6.25(b) shows the control signal V_M.

Figure 6.26 shows the experimental result for a scanning trajectory with 100ms and 25ms periods. It can be seen that the performance provided is outstanding for different references. Figures 6.25(a) and 6.26 also show that the differential actuation effectively removes the uncontrollable point at the flat position, permitting the micromirror to swing across this point without any inconvenient. In general a scanning trajectory fits well the control system since it has been noted by simulation and

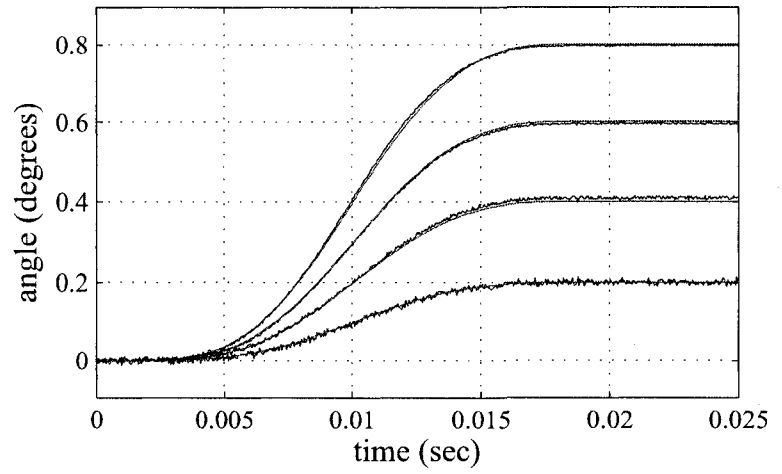

(a)

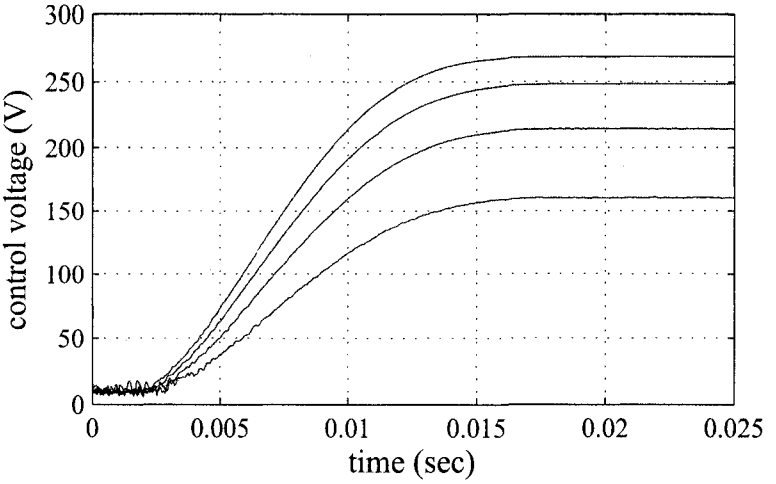

(b)

FIGURE 6.24 CLOSED-LOOP CONTROL WITH SINGLE ACTUATION SCHEME: (A) SYSTEM RESPONSES, (B) CONTROL SIGNALS.

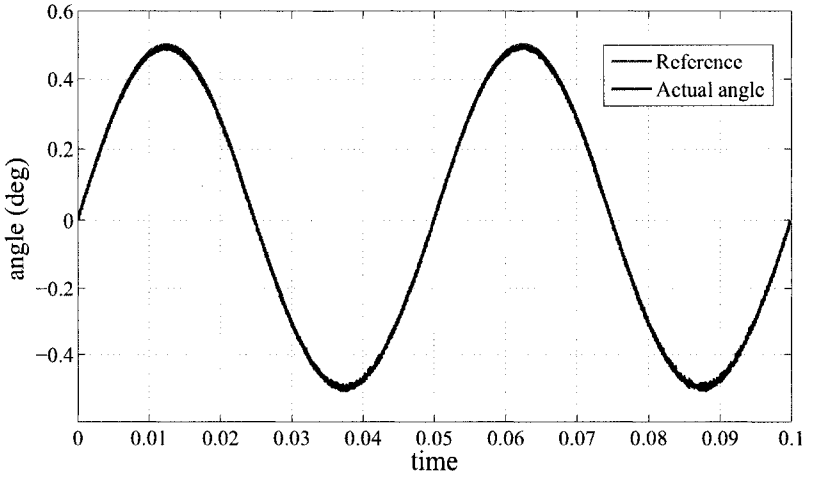

(a)

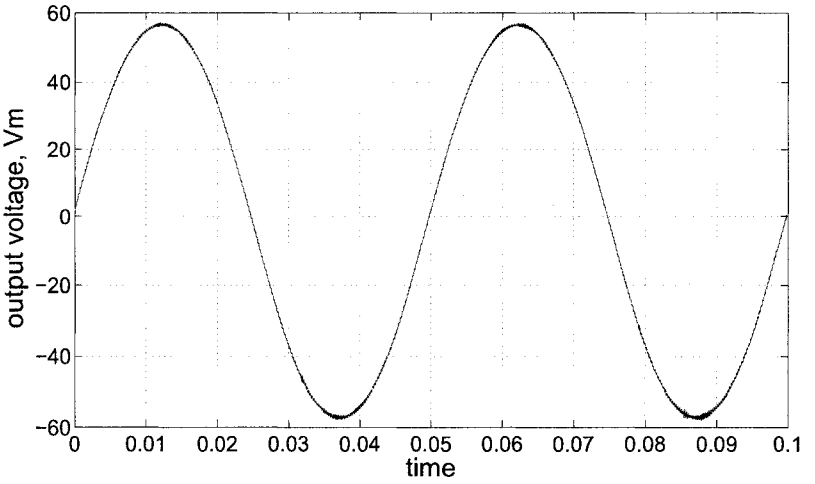

(b)

FIGURE 6.25 CLOSED-LOOP SCANNING CONTROL: (A) SYSTEM RESPONSE θ, (B) CONTROL SIGNAL V_M.

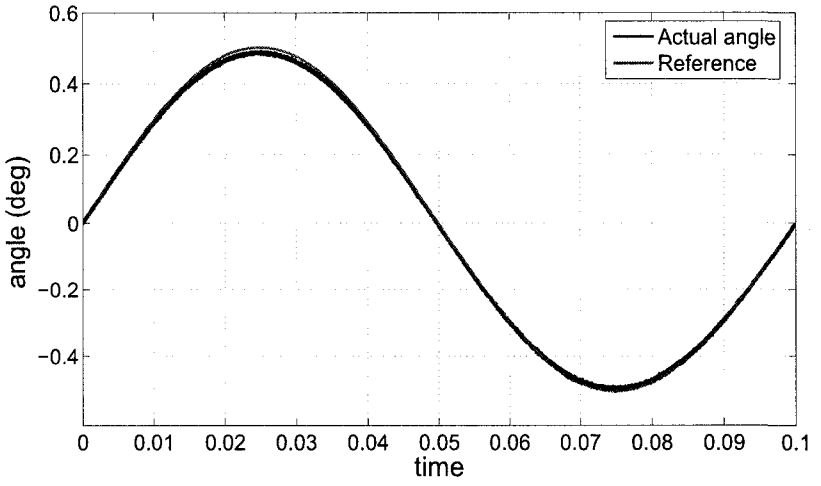

(a)

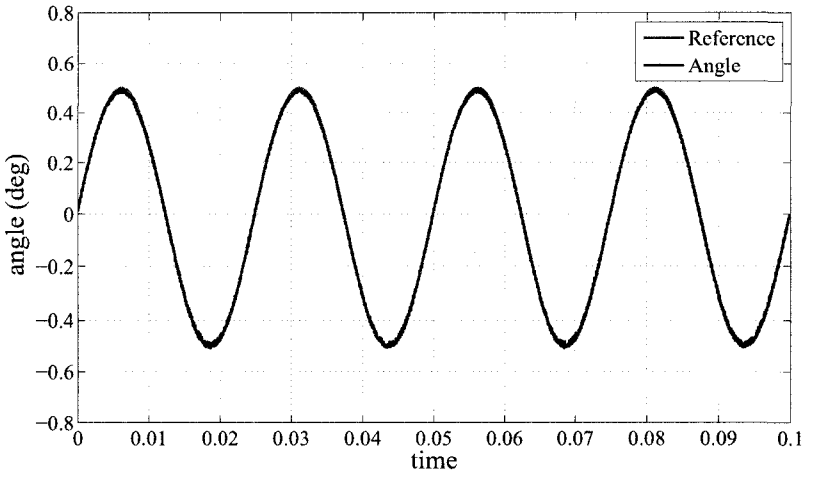

(b)

FIGURE 6.26 CLOSED-LOOP SCANNING CONTROL RESPONSE: (A) 100MS PERIOD, (B) 25MS PERIOD

experimentation that the performance is better when the reference trajectory varies.

CHAPTER 7

CONCLUSIONS AND FUTURE WORK

In general, this work shows that the electrostatic micromirror can certainly be stabilized and operated beyond pull-in by a well designed control system despite the stringent implementation requirements imposed by such a fast and highly nonlinear device, confirming the main thesis stated in chapter 1. Specifically, several conclusions can be stated.

A reliable nonlinear model of the electrostatic micromirror has been successfully achieved. Indeed, the systems described by equations (3.8) and (3.11) can be effectively used for control purposes, modeling properly the single and dual electrostatic micromirrors. The use of the applied voltage as a state variable considerably facilitates the implementation of the control system.

Performing and stabilizing nonlinear control laws for the single and dual electrostatic micromirrors have been developed using the nonlinear tools presented in chapter 4 and a systematic design has been elaborated in chapter 5. Good transient response and precision for set-point and scanning references are offered by the controllers.

A nonlinear tracking control system has been successfully implemented for the single and dual electrostatic micromirrors. Experimental closed-loop results show that the designed controllers perform outstandingly below pull-in for both kinds of micromirror. Furthermore, operation beyond pull-in has been demonstrated with satisfactory performance.

The uncontrollability at the flat position has been successfully removed by making use of a differential actuation scheme. Experimental closed-loop results in chapter 6 show

that using this approach the dual-electrode electrostatic micromirror can effectively follow any reference that crosses the flat point.

Numerous aspects influencing the real-time performance of the control system have been identified. Strengths as well as bottlenecks, drawbacks and minimum specifications have been pointed out and described. In general, the setup has an excellent performance below pull-in but only satisfactory beyond pull-in. From extensive test results it is concluded that the setup is currently operating at its limit and improved results should be expected provided a specialized embedded platform.

A working low cost setup has been put together to implement the closed-loop control of electrostatic micromirrors. A compromise between cost and performance has been done. The design of this platform proposes a middle-level integration of the control system into a MEMS application.

In order to assure the effectiveness of MEMS control systems, the development of MEMS should include control considerations in earlier stages of their design. Crucial parameters such as natural frequency, damping ratio, among other dynamic parameters, impose implementation specifications depending on the particular application, affecting the complexity and the cost of control systems.

The inclusion of a physical protection has been shown to be an effective solution. It enables the realizations of tests beyond pull-in and improves the control system experimental performance. This is one of the most important recommendations suggested by this work.

According to these conclusions and in the author's opinion, several suggestions can be made to direct future work:

Closed-loop results beyond pull-in can be far improved by increasing the precision and computing speed of the setup components. In particular, a faster and better controlled

platform would enhance the real-time performance of the controllers. Theoretically, there is no reason for not achieving higher reference angles beyond pull-in since it is the setup that is currently imposing its limit.

The system model could be improved by including unmodeled behaviour as suggested in chapter 6 since some micromirrors were found to considerably disagree with it. Further work could also be done with the model by using optimized model fitting techniques.

Specialized nonlinear techniques such as state estimation, robust design, and system optimization in hand with low level implementation techniques and numerical software should be taken into account since any improvement in any direction can make the control system perform better. From a theoretical point of view, it does not exist a best approach to control the micromirror yet. Research is still open to the use of techniques other than those presented in this work. Even extensions or variations of the theory already used can be further investigated.

REFERENCES

AGUDELO, C.-G., ZHU, G. AND SAYDY, L. (2007). Nonlinear closed-loop control of an electrostatic torsional micromirror by means of differential actuation. *Proc. of the IEEE-MWSCAS/NEWCAS'07.* Montreal, Quebec.

ANDERSON, R. C., KAWADE, B., MAITHRIPALA, D. H. S., RAGULAN, K., BERG, J. M. AND GALE, R. O. (2005). Integrated charge sensors for feedback control of electrostatic MEMS. *Proc. of the SPIE conference on Smart Structures and Materials 2005.* San Diego, 42–53.

BANKS, D. (2006). *Microengineering, MEMS, and interfacing : a practical guide.* Taylor & Francis.

BAUER, C. (2003). Emerging technologies; impetus for future high technology growth. *Electronic Packaging Technology Proceedings, 2003.*

BLOOM, D. M. (1997). The grating light valve: Revolutionizing display technology. *Projection Displays III Symposium, SPIE Proceedings.*

BRYSON, A. E. AND HO, Y.-C. (1975). *Applied Optimal Control.* Taylor and Francis.

CHAN, E. K. AND DUTTON, R. W. (2000). Electrostatic micromechanical actuator with extended range of travel. 9, 321–328.

CHEN, J., WEINGARTNER, W., AZAROV, A. AND GILES, R. C. (2004). Tilt-angle stabilization of electrostatically actuated micromechanical mirrors beyond the pull-in point. *Journal of Microelectromechanical Systems,* 13.

CHU, P. B., BRENER, I., PU, C., LEE, S.-S., DADAP, J. I., PARK, S., BERGMAN, K., BONADEO, N. H., CHAU, T., CHOU, M., DORAN, R. A., GIBSON, R., HAREL, R., JOHNSON, J. J., LEE, C. D., PEALE, D. R., TANG, B., TONG, D. T. K., TSAI, M.-J., WU, Q., ZHONG, W., GOLDSTEIN, E. L., LIN, L. Y. AND WALKER, J. A. (2005). Design and nonlinear servo control of mems mirrors and their performance in a large port-count optical switch. *Journal of MicroElectroMechanical Systems*, 14.

CHU, P. B., LEE, S.-S. AND PARK, S. (2002). Mems: The path to large optical crossconnects. *IEEE Communications Magazine*.

DARVEAUX, R. AND MUNUKUTLA, L. (2005). Critical challenges in packaging mems devices. *Advanced Semiconductor Manufacturing Conference and Workshop, 2005 IEEE/SEMI*. 210–216.

DEGANI, O., SOCHER, E., LIPSON, A., LEITNER, T., SETTER, D. J., KALDOR, S. AND NEMIROVSKY, Y. (1998). Pull-in study of an electrostatic torsion microactuator. 7, 373–379.

FLIESS, M., LÉVINE, J., MARTIN, P. AND ROUCHON, P. (1995). Flatness and defect of nonlinear systems: Introductory theory and examples. *Int. J. of Control*, 61, 1327–1361.

FLIESS, M., LÉVINE, J., MARTIN, P. AND ROUCHON, P. (1999). A Lie-Bäcklund approach to equivalence and flatness of nonlinear systems. 44, 922–937.

GADELHAK, M. (2006a). *The MEMS handbook. MEMS : applications.* Taylor & Francis, second edition.

GADELHAK, M. (2006b). *The MEMS handbook. MEMS : design and fabrication.* Taylor & Francis, second edition.

GAURA, E. (2006). *Smart MEMS and sensor systems.* Imperial College Press.

GERE, J. M. AND TIMOSHENKO, S. P. (1997). *Mechanics of Materials.* PWS Pub. Co, fourth edition.

HARSHAD, S., NAVID, Y. AND MASTRANGELO, C. (2003). Application of sliding mode control to electrostatically actuated two-axis gimbaled micromirrors. *Proc. of the American Control Conference.*

HERMANN, R. AND KRENER, A. (1977). Nonlinear controllability and observability. *IEEE Transactions on Automatic Control.*

HORNBECK, L. J. (1990). Deformable-mirror spatial light modulators. *Spatial Light Modulators and Applications III, SPIE.* vol. 1150, 86–102.

ISIDORI, A. (1995). *Nonlinear Control Systems.* Springer-Verlage, London, third edition.

JAIN, A., KOPA, A., PAN, Y., FEDDER, G. AND XIE, H. (2004). A two-axis electrothermal micromirror for endoscopic optical coherence tomography. *IEEE Journal of selected topics in quantum electronics.*, 10.

KESSEL, V. (1998). A mems-based projection display. *Proc. of the 1998 IEEE Integrated Sensors, Microactuators, and Microsystems (MEMS).* vol. 86.

KHALIL, H. K. (2002). *Nonlinear Systems.* Prentice Hall, third edition.

KOVACS, G. T. A. (1998). *Micromachined Transducers Sourcebook.* McGraw-Hill, New York.

LEONDES, C. (2006). *MEMS/NEMS handbook : techniques and applications. Volume 5, medical applications and MOEMS.* Springer.

LÉVINE, J. (2004). *Analyse et Commande des Systèmes Non Linéaires.* [Online] Available: http://cas.ensmp.fr/~levine/Enseignement/CoursENPC.pdf.

LU, M. S.-C. AND FEDDER, G. K. (2004). Position control of parallel-plate microactuators for probe-based data storage. *Journal of Microelectromechanical Systems*, 13, 759–769.

LYSHEVSKI, S. AND LYSHEVSKI, M. (2003). Nano- and microoptoelectromechanical systems and nanoscale active optics. *Nanotechnology, 2003. IEEE-NANO.* vol. 2.

MAITHRIPALA, D. H. S., BERG, J. M. AND DAYAWANSA, W. P. (2005a). Control of an electrostatic mems using static and dynamic output feedback. *ASME Journal of Dynamic Systems, Measurement and Control*, 127, 443–450.

MAITHRIPALA, D. H. S., BERGĘAND, J. M. AND DAYAWANSA, W. P. (2003). A port-controlled hamiltonian approach to control of an electrostatic mems actuator. *Proc. of the International Mechanical Engineering Congress 2003.* Washington, D. C., 687–691.

MAITHRIPALA, D. H. S., KAWADE, B. D., BERG, J. M. AND DAYAWANSA, W. P. (2005b). A general modelling and control framework for electrostatically actuated mechanical systems. *Int. J. Robust Nonlinear Control*, 15, 839–857.

MASTRANGELO, C. H. (1999). Suppression of stiction in mems. Technical report, Spring MRS Meeting, Boston, MA.

MCCARTHY, B., ADAMS, G. G., MCGRUER, N. E. AND POTTER, D. (2002). A dynamic model, including contact bounce, of an electrostatically actuated microswitch. *Journal of Microelectromechanical Systems*, 11, 276–283.

MOTAMEDI, M. E. (2005). *MOEMS : Micro-Opto-Electro-Mechanical Systems.* SPIE publications.

NADAL-GUARDIA, R., DEHE, A., AIGNER, R. AND ASTANER, L. M. (2002). Current drive methods to extend the range of travel of electrostatic microactuators beyond the voltage pull-in point. *Journal of Microelectromechanical Systems*, 11, 255–263.

PAREEK, A., DOKMECI, M. R., BAKSHI, S. AND MASTRANGELO, C. H. (2005). Torque multiplication and stable range tradeoff in parallel plate angular electrostatic actuators with fixed dc bias. 14, 1217–1222.

PENET, J. (2005). Commande d'un système non linéaire par platitude. Technical report, Faculty of Electrical Eng., Ecole Polytechnique Montréal.

RAMANI, C. (2006). Optical mems: boom, bust and beyond. *Optical Fiber Communication Conference, 2006.*

SASTRY, S. (1999). *Nonlinear Systems: Analysis, Stability, and Control.* Springer.

SEEGER, J. I. AND BOSER, B. E. (2003). Charge control of parallel-plate, electrostatic actuators and the tip-in instability. 12, 656–671.

SEEGER, J. I. AND CRARY, S. B. (1997). Stabilization of electrostatically actuated mechanical devices. *Tech. Dig. 9th Int. Conf. Solid-State Sensors and Actuators (Transducers' 97)*. 1133–1136.

SENTURIA, S. D. (2002). *Microsystem Design*. Kluwer Academic Publishers, Norwell, MA.

SLOTINE, J.-J. E. AND LI, W. (1991). *Applied Nonlinear Control*. Prentice Hall, New Jersey.

SUHONEN, M., GRAEFFE, J., SILLANPAA, T., SIPOLA, H. AND EIDEN, M. (2001). Scanning micromechanical mirror for fine-pointing units of intersatellite optical links. *SMART MATERIALS AND STRUCTURES*.

THIELICKE, E. AND OBERMEIER, E. (2000). Microactuators and their tecnologies. *Mechatronics*, 10.

TOSHIYOSHI, H., PIYAMATTANAMETHA, W., CHAN, C. T. AND WU, M. C. (2001). Linearization of electrostatically actuated surface micromachined 2-d optical scanner. 10, 205–214.

TOSHIYOSHI, H. AND WU, M. C. (2002). Design of electrostatic actuators for moems. *Proc. Symp. on Design, Test, Integration and Packaging of MEMS/MOEMS 2002*. 200–207.

TYSON, R. K. (2000). *Introduction to Adaptive Optics*. SPIE Publications.

UCHIMARU, K., KASAHARA, A. AND SEKIMURA, M. (1998). Technical report U.S. Pat. 5 740 150.

WANG, W. AND SOPER, S. (2007). *Bio-MEMS : technologies and applications.* Boca Raton, FL : CRC Press.

XIAO, Z., PENG, W. AND FARMER, K. R. (2003). Analytical behavior of rectangular electrostatic torsion actuators with nonlinear spring bending. *Journal of microelectromech. Syst.*, 12.

ZHAO, Y., TAY, F. E. H., CHAU, F. S. AND ZHOU, G. (2006). Stabilization of dual-axis micromirrors beyond the pull-in point by integral sliding mode control. *Journal of Micromechanics and Microengineering*, 16.

ZHU, G., LÉVINE, J. AND PRALY, L. (2005a). Improving the performance of an electrostatically actuated mems by nonlinear control: Some advances and comparisons. *Proc. of the 44th IEEE CDC and ECC 2005.* Seville, Spain, 7534–7539.

ZHU, G., LÉVINE, J. AND PRALY, L. (2005b). On the differential flatness and control of electrostatically actuated MEMS. *Proc. of the 2005 American Control Conference.* Portland, OR, 2493–2498.

ZHU, G., LÉVINE, J., PRALY, L. AND PETER, Y.-A. (2006a). Flatness-based control of electrostatically actuated MEMS with application to adaptive optics: A simulation study. 15, 1165–1174.

ZHU, G., PACKIRISAMY, M., HOSSEINI, M. AND PETER, Y.-A. (2006b). Modelling and control of an electrostatically actuated torsional micromirror. *Journal of Micromech. Microeng.*, 16, 2044–2052.

ZHU, G., PENET, J. AND SAYDY, L. (2007). Modeling and control of electrostatically actuated MEMS in the presence of parasitics and parametric uncertainties. *ASME Journal of Dynamic Systems, Measurement and Control*, 00, 00–00.